# Beyond 5G White Paper
# Supplementary Volume
## “Radio Technologies for higher frequency”

Version 1.0

March 7, 2024

Beyond 5G Promotion Consortium
White Paper Subcommittee

【Revision History】

| Ver. | Date | Contents | Note |
|---|---|---|---|
| 1.0 | 2024.3.7 | Initial version | |
| | | | |
| | | | |
| | | | |

## Preface

In our published white paper “Beyond 5G White Paper ~Message to the 2030s~”, we researched what are required in various industries in the Beyond 5G era, then we proposed “Further enhancement of specific 5G features” such as ultra-high speed wireless access at 10 times faster than 5G’s, 1/10$^{th}$ of 5G’s latency. To address these target, we need possibility to use a drastically wider bandwidth compared with 5G. The higher frequency spectrum, spanning from millimeter waves to THz waves, unlocks the potential for significantly wider bandwidth. This leap enables data transfer rates exceeding 100 Gbps and process massive amounts of data from any location instantly and accurately. Moreover, the short wavelength of the THz spectrum allows for the miniaturization of antenna elements, leading to the development of ultra-massive MIMO systems. These systems promise enhanced coverage through pencil-beamforming and heightened spectrum efficiency via superior spatial resolution and frequency reuse.

However, the path to integrating THz technology is not without its challenges. Terahertz waves tend to travel through a straight path than millimeter waves and cannot propagate over a long distance. In order to address this problem, it is necessary to carry out technical examination on terahertz waves to clarify their radio propagation characteristics, establish their propagation model and high-precision propagation simulation technique, and advance device technology. A wide range of frequency utilization technologies, such as spectrum sharing, and a review of spectrum utilization methods in low frequency bands, will also be important.

In addition to the extremely high data rates, high-resolution sensing and imaging, and high-precision positioning applications will be implemented into THz communications, whose THz spectrum has features such as wider bandwidth operation, higher gain antenna performance, and frequency-selective resonant absorption characteristics. Moreover, as a further coverage extension technique, RIS reflectors can be applied on the wall of the room or the building to deliver THz waves to the non-covered areas. These technologies, ultra-massive MIMO, RIS and Sensing technologies, are discussed in detail in our other white papers.

To tackle these challenges and to realize new use cases, a lot of research and development activities in Japan. In this white paper, we show these research and development activities and its results with a lot of figures as follows.

- *“Spatial Characteristics of Sub-THz Band Radio Propagation in Indoor Environments for Beyond 5G”* describes they measured and analyzed path loss and direction of arrival of multipath in sub-terahertz wave bands of 160 GHz and 300 GHz in an indoor conference room.

- *"Path Loss Characteristics from Microwave to Sub-THz Bands in Urban Environment for Beyond 5G"* reports the path loss, namely basic transmission loss, and building penetration loss from microwave to sub-THz bands in urban environment to exploit the new spectrums for beyond 5G.
- *"Evaluation Technique for Propagation Characteristics of 300-GHz-band Radio wave near the Human Body"* describes the evaluation techniques for 300-GHz radio propagation near the human body, including diffraction and reflection characteristics near the human body.
- *"AI Calibration Technique for RF Impairments with Sub-THz transmission"* presents the conceptual overview of artificial intelligence (AI) device calibration and AI calibration network to optimize communication quality and calibration cost based on AI. Furthermore, as a basic examination of AI device calibration, they demonstrate a compensation technology of RF impairments based on deep neural network (DNN).
- *"Sub-THz-Band Massive MIMO Technology for Beyond 5G/6G"* introduces link-level simulations of a 100 GHz-band radio access technology exploiting Massive MIMO, over-100 Gbps downlink throughput and coverage performances are clarified in the sub-THz band.
- "*High-Capacity Wireless Transmission Technology using Orbital Angular Momentum Multiplexing in the Sub-THz Frequency Bands"* describes they designed and implemented an 8×8 Butler matrix that performs discrete Fourier transform (DFT) processing in an analog way to generate and separate OAM waves with high precision over 32 GHz bandwidth and a parabolic reflector antenna to extend the transmission distance.
- *"Performance Analysis of OAM Multiplexing Using Parabolic Antenna"* describes that they investigate OAM multiplexing transmission with a parabolic antenna for a link distance and analyze the received power concerning link distance, carrier frequency, and receiving antenna radius, as well as highlight the advantages of planar reception achieved by the parabolic antenna. Additionally, they also demonstrate how OAM modes affect propagation attenuation at different link distances.
- *"Antenna Array Module for Sub-THz Communications"* reports their developments and achievements of an antenna array module with element pitch less than 1 wavelength (1λ) at 300 GHz.
- *"Virtualized terminal technologies for high-capacity communications in Beyond 5G era"* presents a "virtualized terminal" concept for enhanced uplink capacity in beyond 5G networks to overcome the space and power constraints of conventional MIMO systems, and also reports their experimental results.

- *"Sub-THz multi-beam antennas for virtualized terminal technologies"* describes their development of multi-beam antennas using Plano-convex lenses, Spherical lenses and Rotman lens arrays at Sub-THz band to apply to the virtualized terminal technologies of user-centric architecture for future beyond 5G/6G systems.
- *"Sub-THz band device technologies"* presents sub-THz band device technologies from high power transistors to RF components with the experiments and simulation results.
- *"6G Simulator using Real Environment Model based on Point Cloud Data"* describe an overview of the functions of the 6G system level simulator they have developed and an example of its performance evaluation.
- *"THz Sensing and Communication Towards Future Intelligence Connected Networks"* describes their research and prototype verification of ISAC feature on THx spectrum.
- *"300GHz point-to-point fixed wireless transmission systems"* describes a 300 GHz fixed radio transmission system based on V-band IF signal processing and also recent research results on reflection loss and scattering due to roughness.

In conclusion, as we embark on the journey towards Beyond 5G technologies, the THz spectrum emerges as a pivotal element in this technological evolution. Japan's endeavor to overcome the challenges posed by THz wave usage, coupled with its commitment to research and development in this domain, positions it at the forefront of this next generation communication revolution. This white paper aims to provide a comprehensive overview of the potential, challenges, and future directions of THz technology in the Beyond 5G landscape, with a particular emphasis on its implications and advancements within Japan.

This White Paper was prepared with the generous support of many people who participated in the White Paper Subcommittee. The cooperation of telecommunications industry players and academia experts, as well as representatives of various industries other than the communications industry has also been substantial. Thanks to everyone's participation and support, this White Paper was able to cover a lot of useful information for future business creation discussions between the industry, academia, and government, and for investigating solutions to social issues, not only in the telecommunications industry, but also across all industries. We hope that this White Paper will help Japan create a better future for society and promote significant global activities.

Kazunori Sakumoto, Fujitsu

# I. Spatial Characteristics of Sub-THz Band Radio Propagation in Indoor Environments for Beyond 5G

Nobuaki Kuno, Koshiro Kitao, Takahiro Tomie, Satoshi Suyama
NTT DOCOMO, INC.
Mitsuki Nakamura, Minoru Inomata, Wataru Yamada
NTT Access Network Service Systems Laboratories, NTT Corporation.

*Abstract*— **For the 6th generation mobile communication system (6G), realization of ultra-high speed and large capacity communication over 100 Gbps is examined. To achieve communications over 100 Gbps, one method is using sub-terahertz bands from 100 GHz to 300 GHz which provide ultra-wide bandwidth. However, because of large propagation loss, these band are suitable for short communication range, and indoor environment will be an important scenario. In indoor environment due to large blocking loss of obstacle, it is necessary to investigate methods to reduce the effects of blocking, such as utilizing reflected waves from walls and ceilings. Therefore, it is necessary to clarify the path loss of direct and reflected waves and the direction of arrival waves. In this paper, we measured and analyzed path loss and direction of arrival of multipath in sub-terahertz wave bands of 160 GHz and 300 GHz in an indoor conference room.**

## I-1. Introduction

The actualization of ultra-high-speed and high-capacity communications exceeding 100 Gbps is under investigation for the 6th generation mobile communication system (6G) [1]. In order to actualize a communications speed of greater than 100 Gbps, the use of the sub-terahertz wave band from 100 GHz to 300 GHz, which can utilize a wide frequency bandwidth, is attracting attention. Various studies on sub-terahertz charged wave propagation have been reported [2] - [4].

Various organizations are investigating sub-terahertz bands for 6G. NTT DOCOMO has published a 6G white paper, which indicates a frequency band of up to 300 GHz as the scope of a 6G study [1]. This white paper shows that the communications in the 6G era can be carried out in various environments at ultra-high speeds and with high capacity. In order to achieve this, it is necessary to investigate the propagation characteristics of sub-terahertz bands in various environments.

The path loss of sub-terahertz wave band is larger than that of millimeter wave. Therefore, the indoor line-of-sight environment, where path loss is relatively smaller than the outdoor or the non-line-of-sight environment, is considered to be a leading environment where sub-terahertz waves are used. For system evaluation, a channel model for standardization such as International Telecommunication Union

Radiocommunication Sector (ITU-R) M. 2412 is necessary, and for model construction, clarification of path loss, delay and angular characteristics is necessary [5].

This paper reports the results of measurements of arrival waves from walls and the ceiling of indoor conference rooms using two frequencies, 160 GHz and 300 GHz, in indoor environments. This paper describes the measurement environment and measurement method using 160 GHz and 300 GHz indoors. Next, this paper presents the measurement results of the path loss of the arrival wave from a direction other than the Tx antenna direction, which is achieved when changing the direction of a high-directivity Tx antenna and examining the strength and direction of the arrival wave.

### I-2. Measurement Environment and Measurement Method

Measurements were taken in a conference room in the NTT DOCOMO R&D Center. Fig. I-1 shows the measurement environment and Table I-1 gives the measurement parameters. As shown in Fig. I-1(a) and Fig. I-1(b), the measurement environment is a space surrounded by walls and glass windows on all sides. In the diagram in Fig. I-1(a), the right side is a wall in which multiple partitions are arranged in parallel. At the bottom of the figure there is a wall and an entrance door. The left side is a wall, and a part of the wall near the top of the figure contains a glass window. The wall at the top of the figure has a single glass window. The size of the room is approximately 12 m square, the height of the ceiling is approximately 3.6 m, and desks and chairs are arranged such that they surround the center of the room. The height of the desks is approximately 70 cm, and the height of the chairs is approximately 83 cm. The desks have metal legs. The chairs have metal legs and a plastic back.

For the measurement, two frequencies with the center frequency of 160 GHz and 300 GHz are used. The Tx antenna is placed in the corner of the room, and the Rx antenna is placed at measurement point A, which is at the center of the room, or measurement point B, which is set at a point in the room diagonal to the Tx antenna. To acquire the waves reflected from the wall surface, the horizontal direction of the Tx antenna is changed every 10 degrees from the 0-degree direction to the 90-degree direction in Fig. I-1(a). The ceiling direction is set to + for the angle of elevation and the ground direction to – for the angle of elevation, and the angle of elevation direction is changed every 10 degrees from -30 degrees to 30 degrees. The Rx antenna is rotated horizontally 360 degrees in the direction of each Tx antenna, and the angle of elevation direction is changed every 3 degrees from -12 degrees to 30 degrees. From the received level obtained by measurement, the path loss is calculated based on the transmitter used for the measurement and the Tx and Rx antenna gain.

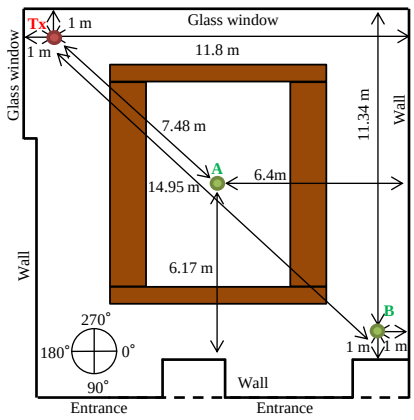


(a) Diagram of measurement environment

(b) Photo of measurement environment

Fig. I-1 Measurement environment.

Table I-1. Measurement parameters

| Parameter | Value | |
|---|---|---|
| Center frequency | 160 GHz | 300 GHz |
| Transmission signal | CW | |
| Tx antenna | Horn antenna | |
| Rx antenna | Cassegrain antenna | |
| Tx azimuth HPBW | 18 deg. | 10 deg. |
| Tx elevation HPBW | 17 deg. | 9 deg. |
| Rx azimuth HPBW | 0.9 deg. | 0.9 deg. |
| Tx elevation HPBW | 0.9 deg. | 0.9 deg. |
| Tx antenna height | 3 m | |
| Rx antenna height | 1 m | |

### I-3. Measurement Results

Fig. I-2 (a) shows the minimum value of the path loss in all Tx antenna directions for each Rx antenna direction. From Fig. I-2 (a), we can confirm an arrival wave (indicated in red) with a path loss of 130 dB or less from directions other than approximately 230 degrees horizontal and approximately 15 degrees elevation, which are directions of the Tx antenna as seen from the Rx antenna. Fig. I-2 (b) shows the minimum path loss in all Tx antenna directions for each Rx antenna direction at 160 GHz. Even at 160 GHz, it is possible to confirm an arrival wave (shown in red) with a path loss of 120 dB or less from the direction of approximately 230 degrees horizontal and approximately 15 degrees elevation corresponding to the Tx antenna direction and other directions from the Rx antenna. The arrival wave in the direction with an approximate 6 degree elevation and approximate 40 degree horizontal is called A1, the arrival wave in the direction with an approximate 6 degree elevation and approximate 110 degree horizontal is called A2, the arrival wave in the direction with an approximate 24 degree elevation and approximate 230 degree horizontal is called A3, and the arrival wave in the direction

with an approximate 6 degree elevation and approximate 350 degree horizontal is called A4.

Similarly, Fig. I-3 (a) and Fig. I-3 (b) show the minimum path loss in all Tx antenna directions for each Rx antenna direction at 160 GHz and 300 GHz at measurement point B. As shown in Fig. I-3 (a), an arrival wave, which is yellow on the color bar, with a path loss of approximately 120 dB can be seen from the angle of elevation of approximately 6 degrees and other directions at approximately 230 degrees horizontal, which is the direction of the Tx antenna. As shown in Fig. I-3 (b), even at 300 GHz, a red arrival wave with a path loss of 130 dB or less can be confirmed from the direction with an angle of elevation of approximately 6 degrees and other directions at approximately 230 degrees horizontal, which is the direction of the Tx antenna. The arrival wave in the direction with an angle of elevation of approximately 12 degrees at approximately 50 degrees horizontal is referred to as B1, the arrival wave in the direction with an angle of elevation of approximately 12 degrees at approximately 130 degrees horizontal is referred to as B2, the arrival wave in the direction with an angle of elevation of approximately 12 degrees at approximately 230 degrees horizontal is referred to as B3, and the arrival wave in the direction with an angle of elevation of approximately 9 degrees at approximately 320 degrees horizontal is referred to as B4.

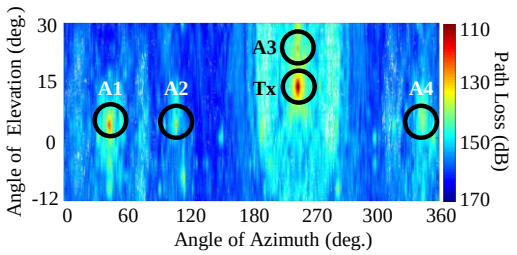


(a) Composite diagram at 300 GHz

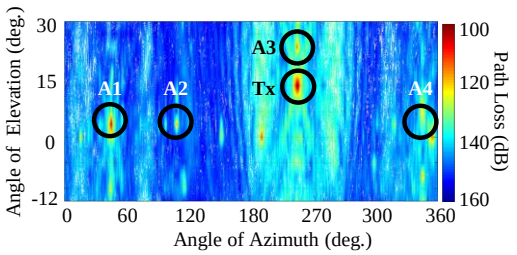


(b) Composite diagram at 160 GHz

Fig. I-2. Measurement results at measurement point A.

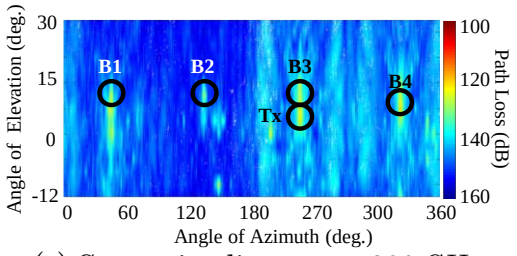


(a) Composite diagram at 300 GHz

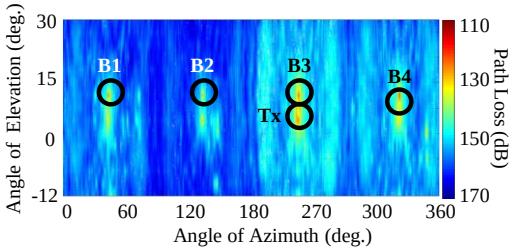


(b) Composite diagram at 160 GHz

Fig. I-3. Measurement results at measurement point B.

## I-4. Conclusion

Using the two frequencies of 160 GHz and 300 GHz, which are sub-terahertz wave bands, multipath wave measurements were carried out in an indoor environment. For both frequencies, multiple arrival waves were confirmed from the wall surface and ceiling directions except for the Tx antenna direction. The difference in the path loss of the arrival wave from the wall and ceiling directions was approximately 10 dB to approximately 30 dB compared to that for the arrival wave from the Tx antenna direction. We found that even if the direct wave is blocked in the sub-terahertz wave bands of 160 GHz and 300 GHz, there is a possibility of communications using these arrival waves.

## REFERENCE


[1] NTT DOCOMO, INC., "White paper: 5G Evolution and 6G," Jan. 2022. https://www.docomo.ne.jp/english/binary/pdf/corporate/technology/whitepaper_6g/DOCOMO_6G_White_PaperEN_v4.0.pdf

[2] M. Inomata et al., "Terahertz propagation characteristics for 6G mobile communication systems," 2021 15th European Conference on Antennas and Propagation (EuCAP), Dusseldorf, Germany, pp. 1-5, March 2021.

[3] T. S. Rappaport et al., "Wireless communications and applications above 100 GHz: Opportunities and challenges for 6G and beyond," IEEE Access, vol. 7, pp. 78729-78757, 2019.

[4] M. Nakamura et al., "Measurement of Multipath Waves at 160 GHz and 300 GHz in an Indoor Conference Room," 2023 17th European Conference on Antennas and Propagation (EuCAP), Florence, Italy, pp. 1-5. May 2023.

[5] "ITU-R M. 2412–0", Guidelines for evaluation of radio interface technologies for IMT-2020, Oct. 2017.

# II. Path Loss Characteristics from Microwave to Sub-THz Bands in Urban Environment for Beyond 5G

Minoru Inomata, Wataru Yamada, Ryotaro Taniguchi, Daisei Uchida
NTT Access Network Service Systems Laboratories, NTT Corporation.
Nobuaki Kuno, Koshiro Kitao, Takahiro Tomie, Satoshi Suyama
NTT DOCOMO, INC.

***Abstract*—Beyond 5G, sub-terahertz bands, millimeter-wave bands, microwave bands, path loss characteristics, frequency dependency**

## II-1. Introduction

New spectrum used for 6G and beyond 5G are sub-terahertz (THz) bands above 100 GHz for extremely high-speed communication data rates exceeding 100 Gbps. The ITU-R Working Party 5D (WP5D) has agreed on a new recommendation on the Framework and overall objectives of the future development of IMT for 2030 and beyond and agreed a report on the technical feasibility in bands above 100 GHz [1]-[4]. 5G have been rolled out using a combination of sub 6 GHz and millimeter wave (mmW) band. And as networks move toward beyond 5G, newly exploiting the mid-bands in 7-24 GHz and the sub-THz bands, utilization of the combination of multiple frequency bands from microwave to sub-THz bands will be necessary for achieving extremely high-speed and reliable communications. In this study, aiming to exploit the new spectrums for beyond 5G, we reported the path loss, namely basic transmission loss, and building penetration loss from microwave to sub-THz bands in urban environment [5]-[8].

## II-2. Key Propagation Phenomena Affecting Radio Channel Characteristics in bands above 100 GHz

Fig. II-1 shows the key propagation phenomena that affect channel characteristics for the sub-THz bands in urban environment. ITU-R M.2412 [9] proposed models that can calculate path loss that building shadowing and human blockage is considered and the building penetration loss in accordance with the mixing ratio of building materials. The path loss governs the coverage distance and the interference levels for the coexistence of radio services using the same frequency bands. However, the M.2412 path loss models are constructed by using measurement frequency bands below sub 6 GHz and mmW bands [9]. Therefore, it is necessary to clarify the path loss characteristics, which includes frequency dependency from microwave to sub-THz bands for operating the combination of multiple frequency bands.

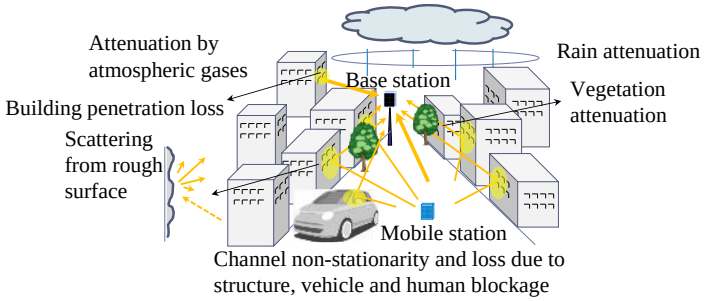


Fig. II-1. Key propagation phenomena in bands above 100 GHz [5][6]

### II-3. Measurement System Setup

The measurement system uses frequency bands at 2, 26, 97, 158 and 300 GHz. Continuous wave (CW) signal was transmitted using the omni-directional antenna [7][8]. The omni-directional antenna with 60° of half power beam width (HPBW) for 2, 26, 97 GHz in the elevation plane, 20° of HPBW for 158, 300 GHz. At the 2 GHz, the Rx omni-directional antenna measured the path loss. At the 26, 97, 158 and 300 GHz, Rx measured the CW signal while the cassegrain antenna with 4° of HPBW for 26 GHz, 2° of HPBW for 97 GHz, 1° of HPBW for 158 and 300 GHz was rotated 360 degrees in the azimuth plane and up to 20 degrees in the elevation plane. Path loss equivalent to the omni-directional antenna is obtained by this measurement method.

### II-4. Path Loss Characteristics

The path loss measurement environment around Tokyo Station is shown in Fig. II-2 [7]. Path loss was measured at measurement points of the LOS and NLOS environment. The Tx antenna was set on the rooftop of a measurement vehicle with height of 2.55 m, which is lower than the surrounding building's rooftop level. The Rx antenna was fixed to the trolley, with height of 1.7 m. We compared the free space path loss (FSPL) $FSPL(f,d) = 32.4 + 20\log_{10} f + 20\log_{10} d$, M.2412, and measurement results. M.2412 path loss model was used a mandatory model for IMT-2020. The close-in (CI) model is always used to characterize the path loss for LOS and the Alpha-Beta-Gamma (ABG) model for NLOS. The CI model and ABG model are expressed by following equation:

$$PL_{CI}(f,d)(dB) = PL_{FSPL}(f,1) + 10n\log_{10} d + X_{\sigma}^{CI}$$

where $n$ is the path loss exponent (PLE), and $X_{\sigma}^{CI}$ is a shadow fading with a standard derivation of $\sigma$ in dB.

$$PL_{ABG}(f,d)(dB) = 10\alpha\log_{10} d + \beta + 10\gamma\, log_{10}\left(\frac{f}{1\ \mathrm{GHz}}\right) + X_{\sigma}^{ABG}$$

where $\alpha$ and $\gamma$ are the PLE and frequency dependence on path loss, respectively, $\beta$ is the optimized offset in path loss. From Fig. II-3 (a) for LOS, the measured path loss indicate the similar tendency as the predicted path loss of FSPL. It is obvious that the

direct wave in the LOS environment was dominant. Therefore, the PLE for M.2412 path loss model and $PL_{CI}$ is equivalent to that for FSPL. From Fig. II-3 (b) for NLOS, $PL_{ABG}$ by regressing the measured path loss had steeper PLE and larger frequency dependency than the calculation results using M.2412 path loss model. In urban NLOS environment, the diffracted and reflected waves with multiple reflection were major paths. Since the diffraction loss depends on the wavelength and the frequency dependency is significantly larger than M.2412 path loss model. Specifically, in the case of scattering from a building rough surface, the higher the frequency, the larger the scattering power and the lower the reflection power, so it is assumed that since larger reflected loss occurred, the path loss had steep distance attenuation.

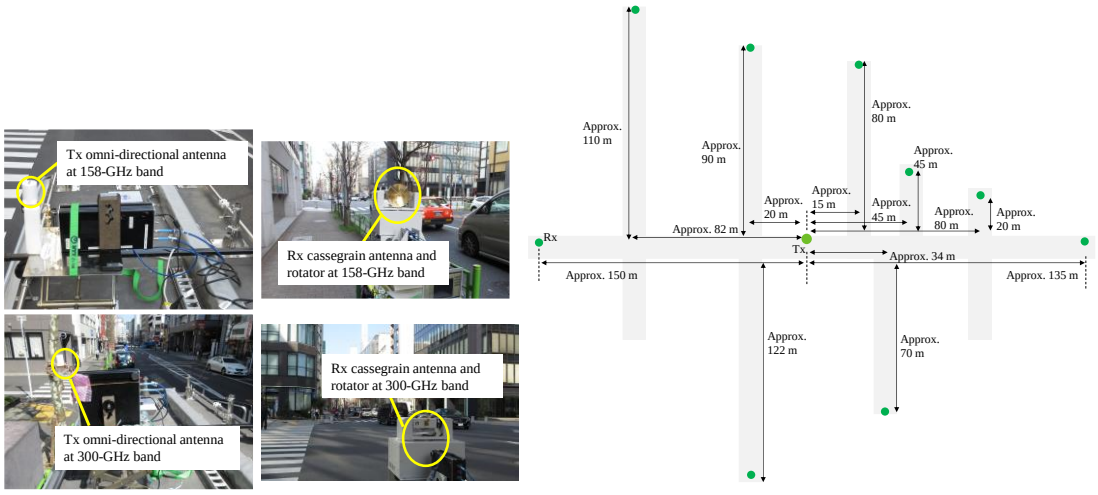


(a) measurement system setup (b) measurement routes

Fig. II-2. measurement system setup and routes [7]

Table II-1. Comparison results [7]

| | | $n$ | *Constant loss (dB)* | | $X_{\sigma}^{CI}$ *(dB)* |
|---|---|---|---|---|---|
| LOS | $PL_{CI}$ | 1.9 | $32.4+20\log_{10} f$ | | 6.04 |
| | *FSPL* | 2.0 | $32.4+20\log_{10} f$ | | 6.21 |
| | *M.2412* | 2.1 | $32.4+20\log_{10} f$ | | 6.86 |
| | | $\alpha$ | $\beta$ *(dB)* | $\gamma$ | $X_{\sigma}^{ABG}$ *(dB)* |
| NLOS | $PL_{ABG}$ | 4.34 | -4.1 | 2.52 | 6.19 |
| | *M.2412* | 3.53 | 22.4 | 2.13 | 9.22 |

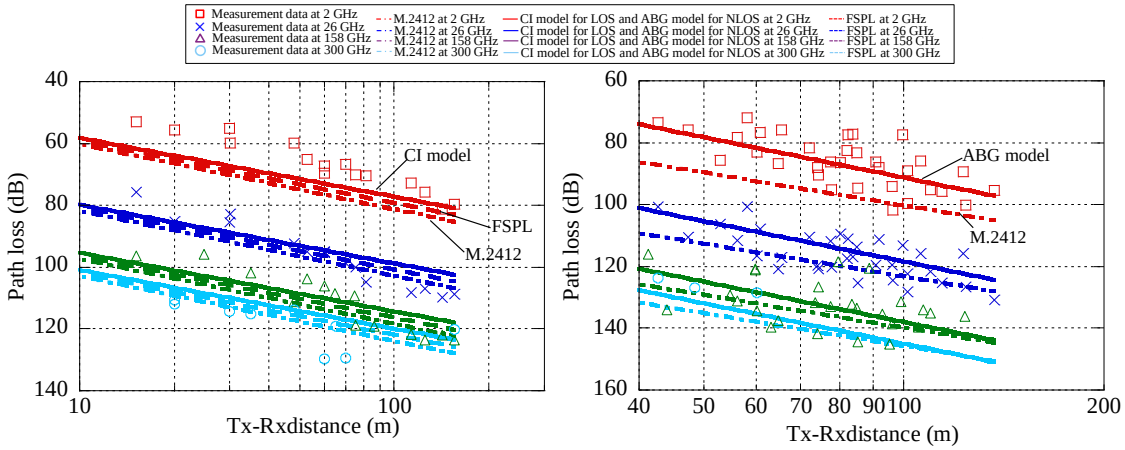


(a) LOS (b) NLOS

Fig. II-3. measurement results [7]

### II-5. Building Penetration Loss

This section introduces the results of measuring building penetration loss at 2, 26, 97, and 158 GHz in an urban environment in Tokyo [8]. Fig. II-4 shows the Tx and Rx antenna setup. The Tx antenna was set on the roof of the building with a height of 2.24 m from the floor, and the Rx antenna was fixed to a trolley in rooms of the building with a height of 1.5 m from the floor. Fig. II-4 shows a comparison between the measurement building penetration loss, prediction results using the M.2412 low-loss model, and proposed model. Table II-2 shows the components of those models. Typical building façades are composed of several materials. The measurement results in M.2412 model can roughly be grouped into two categories: low building-penetration loss results for old buildings with standard glass, and high ones for modern buildings with infrared reflective glass. The proportion of measurement building composed of multi-layer standard glass was about 70%, and that of concrete was about 30%, and the material composite was similar to the low-loss model. Building penetration loss was calculated by sum of the building penetration loss through the external wall $PL_{tw}$ and the indoor loss dependent on the depth into the building $PL_{in}$. $PL_{tw}$ consists of an additional loss due to the non-perpendicular incidence and linear loss as a function of frequency. When the propagation is deeper into the indoor room, indoor loss $PL_{in}$ and variation due to the shadowing of the furniture can occur. It was found that measurement loss due to the non-perpendicular incidence and indoor loss was equivalent to M.2412, but the measurement results were more gradually frequency-dependent than M.2412. Since the material loss tends to increase as the frequency becomes higher or permittivity becomes larger, the power of the transmission paths through concrete is significantly lower in bands above 100 GHz. Thus, it was

assumed that the transmission paths through the glass were dominant and that the M.2412 low-loss model overestimated the building penetration loss due to the higher transmission loss of the concrete. Therefore, we proposed an effective building penetration loss model based on single transmission paths with the lowest transmission loss through standard glass and the RMSE value was 5.7 dB improved.

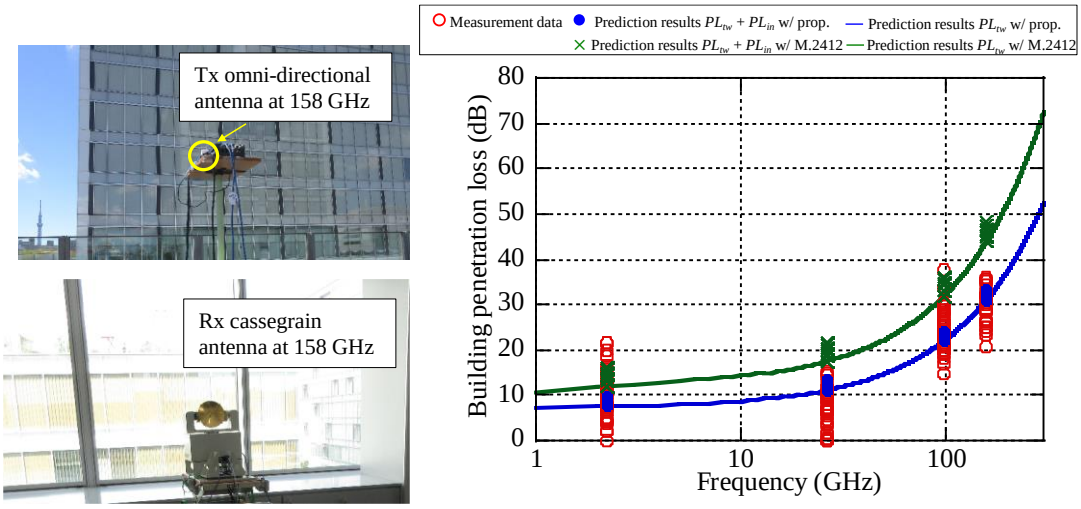


(a) measurement system setup (b) measurement results

Fig. II-4. measurement system setup and results [8]

Table II-2. Comparison results [8]

| | Path loss through external wall: $PL_{tw}$ (dB) | Material loss: $L_{glass}$ (dB) | Indoor loss: $PL_{in}$ (dB) | RMSE (dB) |
|---|---|---|---|---|
| *M.2412* | $5 - 10\log_{10}(0.3 \cdot 10^{-L_{glass}/10} + 0.7 \cdot 10^{-L_{concrete}/10})$ | $2 + 0.2f$ | 0.5 | 11.3 |
| *Prop.* | $4.58 + L_{glass}$ | $2.58 + 0.15f$ | 0.28 | 5.7 |

## II-6. Conclusion

Path loss and building penetration loss characteristics were investigated from microwave to sub-THz bands in urban environment. In the basic outdoor path loss, the results indicate that since the direct wave in the LOS environment was dominant, the PLE for the CI model is equivalent to FSPL and M.2412. From results for NLOS, the PLE and frequency dependency were more significant than M.2412 due to larger diffraction and reflection loss. It was found that the results of building penetration loss above 100 GHz were more gradually frequency dependency than M.2412, and it was assumed that the transmission paths through the glass were dominant. It is essential for accurate path loss prediction to clarify the dominant paths considering the key propagation phenomena such as scattering from a building rough surface and material loss in frequency bands above 100 GHz.

## REFERENCE


[1] NTT DOCOMO, INC. “White Paper, 5G Evolution and 6G,” Feb. 2021.

[2] ITU-R WP5D, “The ITU-R Framework for IMT-2030,” July.2023.

[3] ITU-R WP5D, “Preliminary draft new Report ITU-R M.[IMT.Above 100 GHz] Technical feasibility of IMT in bands above 100 GHz,” July 2023.

[4] D. Uchida, Technologies and Proof-of-Concept Activities for 6G 2022 (TPoC6G 2022) keynote speech, Finland, June 2022.

[5] M.Inomata, et al., “Sub-Terahertz Propagation Characteristics up to 150 GHz for 6G Mobile Communication Systems,” EuMA International Journal of microwave and wireless technologies, March 2022.

[6] M. Inomata et al., "Terahertz Propagation Characteristics for 6G Mobile Communication Systems," EuCAP2021, Germany, March 2021.

[7] M. Inomata et al., " Path-loss Characteristics and Modeling for 2-300-GHz bands in Urban Microcell Environment," EuCAP2023, Italy, March 2023.

[8] M.Inomata et al., “Building Penetration Loss for 2 -150 GHz Bands for Pioneering Terahertz Wave Bands of 6G,” IEICE Technical reports, vol. 122, AP-339, pp. 74-79, January 2023 (Japanese edition).

[9] Rep. ITU-R M.2412-0, “Guidelines for evaluation of radio interface technologies for IMT-2020,” Oct. 2017.

# III. Evaluation Technique for Propagation Characteristics of 300-GHz-band Radio wave near the Human Body

Akihiko Hirata, Chiba Institute of Technology

*Abstract*—**In order to put a terahertz-band Body Area Network (BAN) into practical use, it is necessary to measure a large amount of 300 GHz-band radio propagation data, such as the direction of arrival (DOA) of 300 GHz-band radio signals near the human body, and to construct a propagation model. This chapter describes the evaluation techniques for 300-GHz radio propagation near the human body, including diffraction and reflection characteristics near the human body.**

## III-1. Introduction

In Beyond 5G, the next generation of mobile communications, the use of 300 GHz band wireless links, which can achieve data rates of over 100 Gbit/s, is currently being considered for various use cases such as mobile access, wireless local area networks (LANs), and body area networks (BANs). For practical application of these use cases, it is necessary to evaluate the radio propagation characteristics near the human body in the 300 GHz band and to construct a radio propagation model at this frequency. We have been conducting radio propagation experiments and simulations for building radio propagation models for each of the above-mentioned use cases. In this paper, we report the results of these experiments and simulations of radio propagation at 300 GHz.

## III-2. Shadowing loss due to human body

A 300-GHz-band transmitter (Tx) and a receiver (Rx) were used to measure the shadowing loss due to the human body [1]. The unmodulated continuous wave with a frequency of 293.4 GHz was used for the evaluation of propagation characteristics near human body. The Tx output power was 1.2 mW. A waveguide probe antenna with a gain of 7 dBi was used for both Tx and Rx. The distance between the Tx and Rx was fixed at 2 m, and the received power fluctuation was measured when the human body was moved horizontally from -35 cm to +35 cm in 5 cm increments at the midpoint between the transmitter and receiver. Fig. III-1(a) shows the offset position dependence of the shadowing loss due to the human body. When the human body was facing the Tx, the shadowing loss at an offset position of 0 cm was about 26 dB.

To verify the validity of the measurement results, a radio propagation simulation using the ray trace method was performed. The results are also shown in Fig. III-1(a). When a human model (Model A) with closed armpits shown in Fig. III-1(b) was used, a deviation of 18 dB from the experimental results was observed at an offset position of 0 cm. Fig. III-1(a) also shows the simulation results using a human body model with a 1

cm gap between the armpits and the torso (Model B); for Model B, the simulated shadowing loss is close to the experimental results when the offset position is 0 cm. When the offset position is at the gap between the arm and the torso, the simulated shadowing loss is less than 10 dB, which is 15 dB less than the experimental result. This may be because the position of the gap between the arm and the torso is different between the simulation and the experiment.

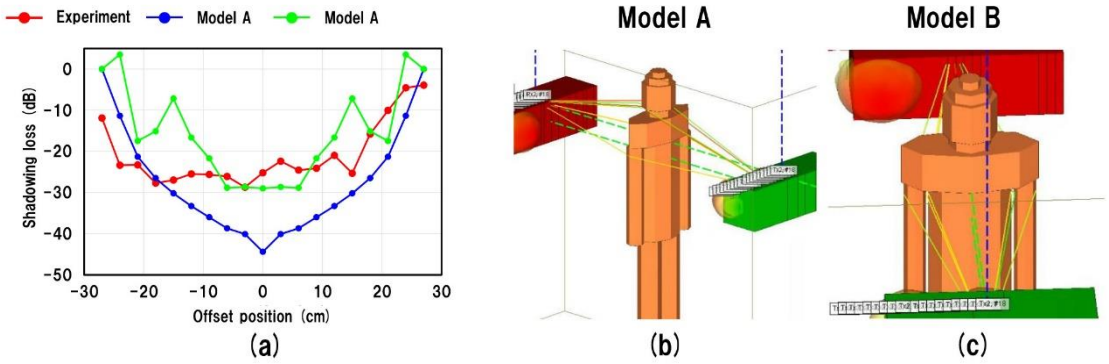


Fig. III-1. (a) Dependence of the shadowing loss by human body on the offset position, (b) human model with armpit closed, (c) human model with a 1 cm gap between the arm and the torso.

### III-3. 300 GHz band human body phantom

To construct a radio propagation model near the human body, it is necessary to measure the shadowing, reflection and scattering characteristics of radio propagation near human body. Since it is difficult for a living human to maintain the same position for a long period of time, it is necessary to use a human body phantom with the same complex permittivity as that of the living human body at the measurement frequency in order to obtain reproducible data. However, there has been no 300-GHz-band human phantom with the same complex permittivity as that of the living human body. Yamazaki et al. reported that the real and imaginary dielectric constants of the human body in the 300 GHz band will be 3.5 to 5.0 and 2.0 to 3.0, respectively, in 2022 [2]. We fabricated a new material based on silicon rubber and evaluated its complex permittivity by ellipsometry using the THz time-domain spectroscopy (TDS) technique. Fig. III-2(a) shows the complex permittivity of the prototype human phantom at 200 to 400 GHz. The real and imaginary dielectric constants are 4.6 and 1.2, respectively, which are close to those of a living human. We prototyped a human phantom with the shape of a human body based on this silicon rubber [3]. Fig. III-2(b) shows a photograph of the prototype human phantom. In the following sections, the diffraction and reflection characteristics at 300 GHz near the human body are evaluated using this human phantom.

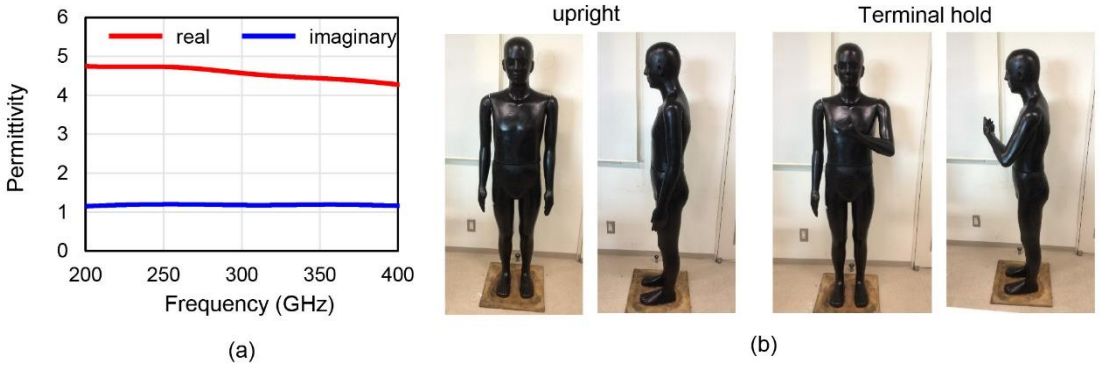


Fig. III-2. (a) Complex permittivity measurement results of the prototype human phantom, (b) Photograph of the prototype human phantom.

### III-4. DOA measurement result

Terahertz-band DOA measurements require large devices that change the azimuth and elevation angles of the Rx. However, these devices take time to measure and are difficult to place near the human body. We have developed a high-speed terahertz hemispheric scanner capable of making DOA measurements of radio propagation at 300 GHz [3]. Fig. III-3(a) shows a schematic diagram of the terahertz band hemispheric scanner. The scanner consists of a 300 GHz-band Rx, a rotating mirror, a fixed mirror, and a rotating stage. 35 dBi lens antenna is connected to the Rx. The rotating mirror and the rotating stage control the elevation and azimuth angles of the terahertz beam to be measured, respectively. The scanning range of the azimuth angle is 360°, and the scanning range of the elevation angle can be selected from 0 to 90° or 45 to 135° by changing the adapter. Fig. III-3(b) shows a photograph of the terahertz hemispheric scanner. The outer surface of the scan direction is surrounded by a radio wave absorber to avoid stray light reception outside the scan direction.

The diffraction characteristics of 300 GHz band radio propagation near the human body were evaluated using a terahertz band hemispherical scanner and a human phantom. The Tx and Rx were placed opposite each other at a transmission distance of 1 m, and a human phantom was placed at the midpoint between the transmitter and receiver. The human phantom was placed directly opposite to the transmitter. A 7 dBi waveguide probe antenna was used for the Tx. Fig. III-4(a) shows the results of DOA measurements. Two diffracted propagation paths were observed on the outside of both arms. In addition, two propagation paths that pass through the gap between the arm and the torso were observed. The DOAs of the two propagation paths through the gap between the arm and torso were wider than the DOAs of the propagation paths through the outer arms.

Next, Fig. III-4(b) shows the results of DOA measurements when the human phantom was wearing a down coat. When the human phantom wears the down coat, these paths

have wider DOA perpendicular to the ground than when the human phantom does not wear the down coat. In addition, periodic variations in DOA were observed, reflecting the periodic surface geometry of the down coat. These wider DOAs may be due to the scattering of radio waves inside the down coat.

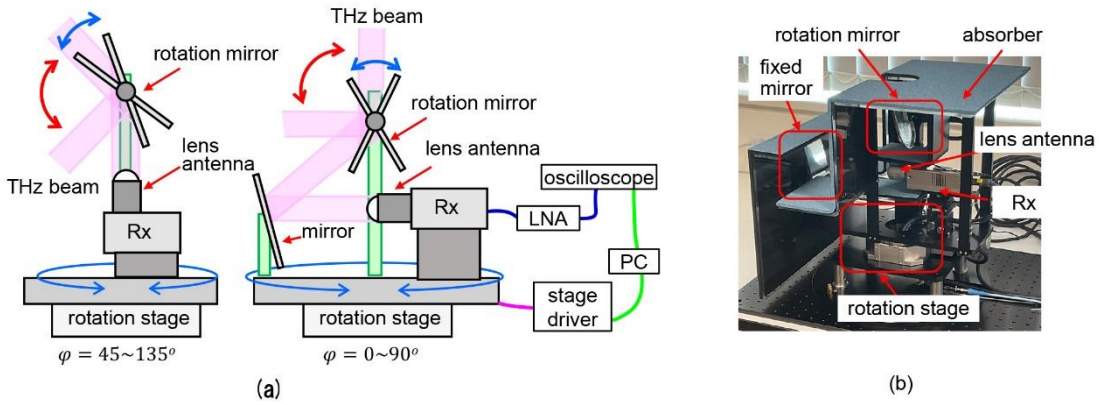


Fig. III-3. (a) Schematic diagram of the hemispheric scanner, (b) Photograph of the hemispheric scanner.

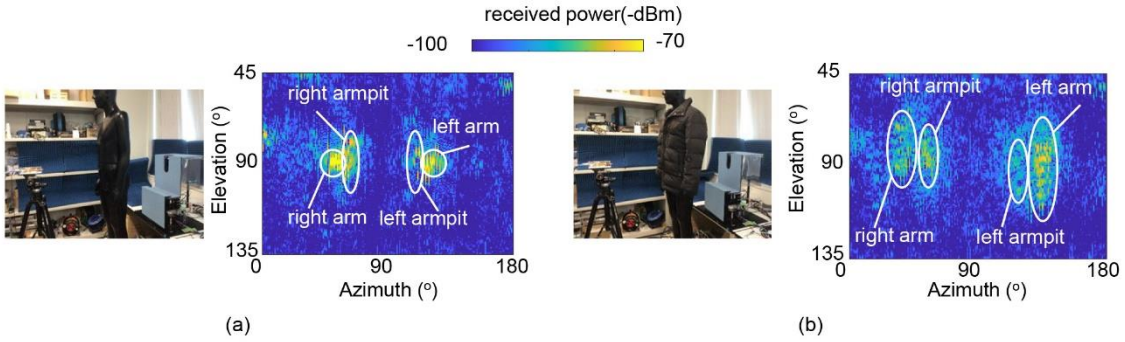


Fig. III-4. (a) Photographs of the experimental setup and measurement results of DOA due to the diffraction on the human phantom, (b) Photographs of the experimental setup and measurement results of DOA due to the diffraction on the human phantom wearing a down coat

Next, the reflection characteristics on the human body were evaluated using the hemispherical scanner and a human body phantom. The Tx and Rx were placed at 0.5 m from the human body phantom so that the angle of incidence and the angle of reflection were 45°. Fig. III-5(a) and Fig. III-5(b) show the measurement results of DOA of the reflected wave from the human body phantom without and with a down coat, respectively. In the case of the phantom without a down coat, the DOA of the propagation path of the reflected wave was observed separately for each body part, such as the chest, chin, and arms. When the down coat was worn, the DOA was observed over a wider area and

reflections were no longer observed separately for each body part. This may be due to the scattering of the down coat.

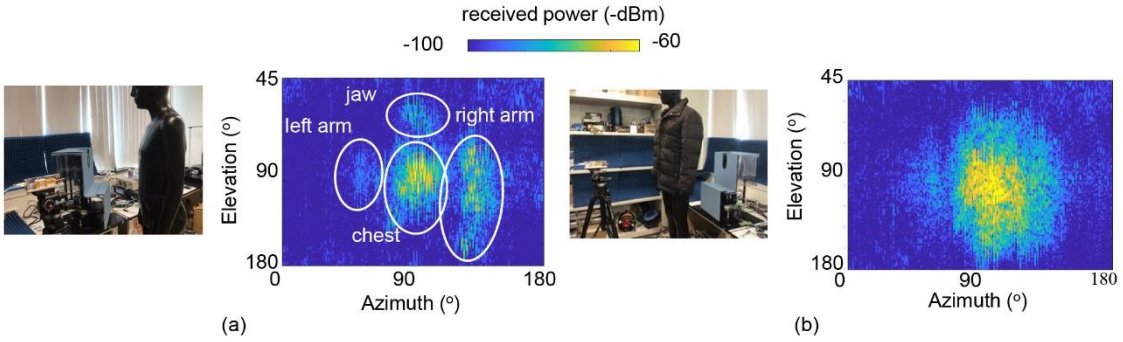


Fig. III-5. (a) Photographs of the experimental setup and DOA measurement results during reflection from the human phantom, (b) Photographs of the experimental system and DOA measurement results during reflection from the human phantom wearing a down coat.

## III-5. Conclusion

Evaluation of radio propagation characteristics near the human body was conducted. To obtain a large amount of reproducible radio propagation data, a human body phantom with a complex permittivity close to that of the human body at 300 GHz was developed. The reflection and diffraction characteristics of radio wave propagation near the human body were evaluated, and it was found that the gap between the arm and torso and the clothing had a significant effect on the radio propagation characteristics near the human body.

## III-6. Acknowledgements

These research results were obtained from commissioned research (No.00401) by the National Institute of Information and Communications Technology (NICT), Japan.

## REFERENCE

[1] S. Takagi et al., “Shadowing and Reflection Loss due to Human Body in 300-GHz-band Wireless Links,” IEICE, B-1-13, 2022.

[2] S. Yamazaki et al., “Investigation of Biological Phantom Reproducing Dielectric Properties of Skin Tissue in Terahertz Frequency Range,” IEICE Technical Report PEM, p1, 2022.

[3] A. Hirata, "Measurement of 300 GHz Band Radio Propagation Characteristics in the Vicinity of Human Body using Terahertz Hemispheric Scanner," 2023 IEEE APS and USNC-URSI, pp. 1221-1222, 2023.

# IV. AI Calibration Technique for RF Impairments with Sub-THz transmission

Keita Kuriyama, Kentaro Tanaka, Hitoshi Hasegawa, Toshifumi Miyagi
NTT Access Network Service Systems Laboratories, NTT Corporation
Satoshi Suyama, Huiling Jiang, Atsuya Nakamura
6G Network Innovation Department, NTT DOCOMO, INC.

***Abstract*— In the sixth-generation mobile communication system (6G) era, high-frequency bands (e.g., sub-terahertz (sub-THz) bands) show promise for achieving extremely high-speed and high-capacity communications. However, it is difficult to ensure radio frequency (RF) circuit quality in high-frequency bands compared to lower frequency bands below mmWave, and utilizing higher performance and higher quality circuits lead to higher costs. Considering the increasing popularity of the high-frequency bands, it is vital to achieve low cost while simultaneously ensuring communication quality. It is also necessary to optimize the communication quality, cost, and power consumption of the whole radio access network (RAN) by considering the diversified topology. This chapter presents a conceptual overview of our proposed artificial intelligence (AI) device calibration and the AI calibration network to optimize communication quality and calibration cost based on AI. Further, as a basic examination of AI device calibration, we demonstrate a compensation technology for RF impairments based on a deep neural network (DNN).**

## IV-1. Introduction

One of the requirements for sixth-generation mobile communication systems (6G) is an extremely high data rate and capacity. Radio access technologies (RAT) to provide data rates over 100 Gbps are being discussed as a potential way of meeting this requirement. To achieve 100 Gbps, exploiting higher frequency bands between 100 GHz and 300 GHz with a wider bandwidth than 5G (e.g., sub-terahertz (sub-THz) bands) is a promising approach. However, to utilize the sub-THz bands in 6G, similar to the case when introducing the millimeter-wave band in 5G, there are many technical issues that need to be resolved by the 2030s. These technical issues are diverse and exist mainly in four areas: radio propagation, radio frequency (RF) devices, modulation and demodulation schemes, and air interfaces, which are summarized in detail for each area in [1].

Focusing on the technical issues in RF devices, the characteristics of the RF devices mainly depend on the frequency band and the signal bandwidth, and it is difficult to ensure the same circuit characteristics in the high-frequency bands as those in the low frequency [2]. Some RF impairments, such as frequency selectivity, IQ imbalance, direct

current (DC) offset, carrier leakage, phase noise, and nonlinear distortion, have become increasingly pressing as implementation challenges because they can cause degradation of the communications quality. While performance enhancement and high integration of the RF devices are required, for the popularization of high-frequency bands, the RF devices must be manufactured with a level of accuracy and a cost that enables usage in 6G commercial services. Cost reduction can be achieved by allowing the use of low-quality devices, but a calibration scheme by digital signal processing (DSP) is necessary for ensuring the communication quality. Although a partial compensation technique for the RF impairments by DSP has been proposed, this technique requires designing an optimal digital calibration for high-frequency bands, where the influence of each RF impairment is both large and mixed. In recent years, technology that compensates for multiple RF impairments by utilizing artificial intelligence (AI) such as deep neural networks (DNN) has attracted attention [3].

The performance of the RF device and the resources (e.g., processor capability and power consumption) available for DSP are different for each wireless device. Therefore, it is desirable that the cost of digital calibration be dynamically optimized in accordance with the constraints of the available hardware and the required quality from the applications. In addition, it is necessary to optimize the communication quality, cost, and power consumption of the whole radio access network (RAN) by considering the diversified topology. In this chapter, we present our concept of AI device calibration and the AI calibration network [4], which utilizes AI to optimize the communication quality and the calibration cost. Also, as a basic technology of AI device calibration, a demodulation technology [5] utilizing DNN is introduced.

## IV-2. Concept of AI calibration

### IV-2.1. AI device calibration

Fig. IV-1 shows the concept of AI device calibration. The required specifications for the equipment differ between base station (BS) and user equipment (UE), which means the characteristics of the RF circuit, the capability of the processor, and the allowable power consumption for DSP are also different from each device. On the other hand, regarding the communication quality, the total communication quality that can be observed end-to-end only needs to meet the requirements. In other words, points such as calibrating within the transmitting station to send a high-quality signal, calibrating only at the receiving station, setting the proportion of each calibration processing load, etc. can be freely designed. In AI device calibration, the existence of digital calibration in each station, the compensation scheme to be used, and the level of compensation accuracy are dynamically controlled in accordance with the constraint of available

hardware and the demands of the communication quality. As a case study of a compensation scheme, we introduce a DNN demodulator in Section IV-3.

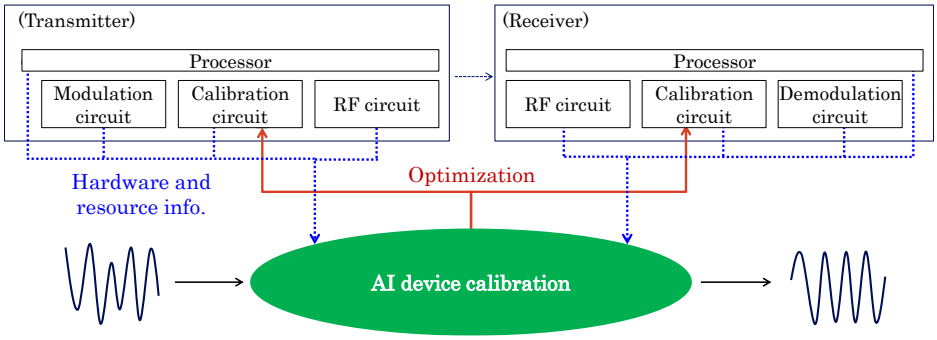


Fig. IV-1. Concept of AI device calibration.

### IV-2.2. AI calibration network

In the 6G era, many devices will be connected to the RAN through various frequency bands, so the topology of the RAN is expected to diversify. Therefore, new radio network topology (NRNT) has been investigated to improve the performance of RAN for 5G Evolution and 6G [6]. In NRNT, the topology changes dynamically in accordance with the environment, situation, and requirements based on various key performance indicators (KPIs). With sub-THz bands, optimization in the whole of RAN including the relay station (RS) is required, since the impact on KPIs such as equipment cost and power consumption seems to be large.

Fig. IV-2 shows the concept of the AI calibration network. The AI device calibration described in Section IV-2.1 is extended to the entire RAN. The AI calibration network collects the resource information such as the performance of the RF devices of each equipment, processor capability, and power consumption available for DSP. The calibration cost of each device is controlled in accordance with the constraint of available hardware and the requirement of communication quality. In addition, appropriate route selection is performed for the optimization of the whole network.

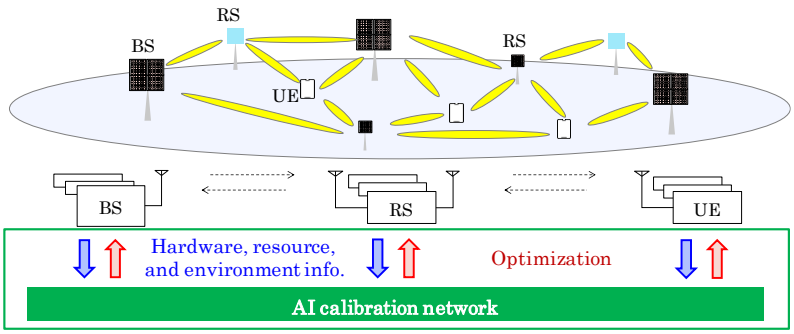


Fig. IV-2. Concept of AI calibration network.

## IV-3. Compensation technique based on AI

### IV-3.1. Deep neural network demodulator

In this section, we introduce a technique to compensate for multiple RF impairments based on DNN. Fig. IV-3 shows the system model of our DNN demodulator. Assuming single carrier-(SC) frequency domain equalization (FDE) transmission with nonlinear distortion of the amplifier and IQ imbalance of the IQ modulator/demodulator, bit detection by DNN is performed for the received symbols after FDE. The FDE output is divided into an IQ real valued sequence after IFFT processing and passed to the input layer of the DNN. The DNN outputs a vector consisting of values from 0 to 1 via the sigmoid function. The DNN is trained to minimize the root mean square error (RMSE) of the training data and the output data. Round processing is performed after the DNN, and the bit string corresponding to the index of the input data is output.

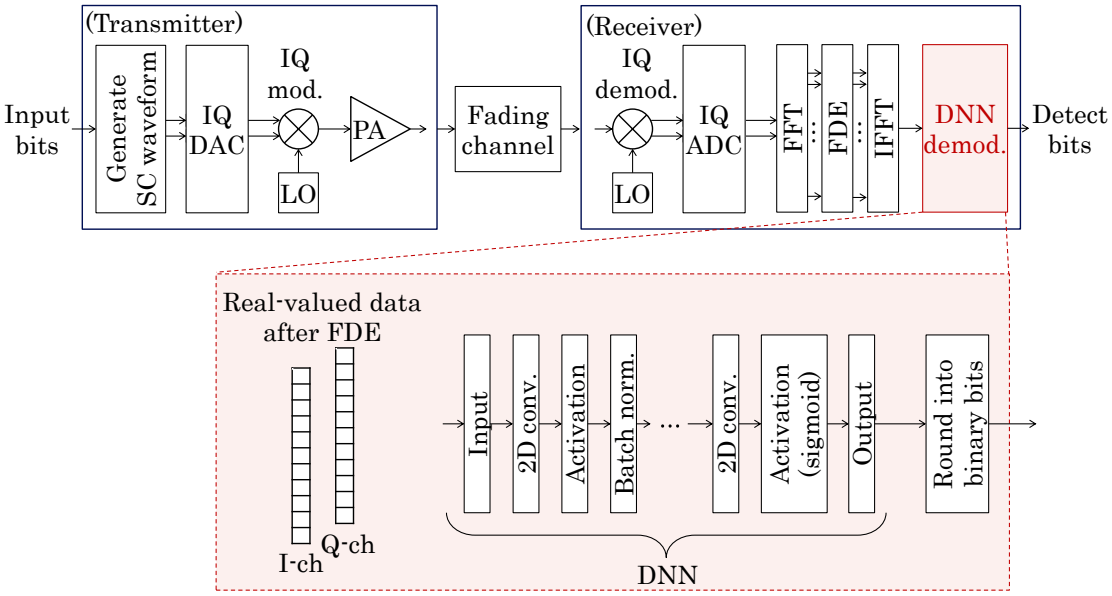


Fig. IV-3. System model of DNN demodulator.

### IV-3.2. Numerical Results

In this section, we evaluate the effectiveness of the DNN demodulator. Table IV-1 lists the parameters utilized during learning and validation. The nonlinearity of the power amplifier utilizes a Rapp model with the input back off (IBO) of 2 dB. The IQ imbalance of the quadrature modulator and demodulator is 1 dB in amplitude and 5° in phase. The average signal to noise power ratio (SNR) is 30 dB while learning the DNN. The fading channel assumes a static environment and utilizes common values in the learning and test data. We use 16-QAM and 64-QAM for the modulation scheme.

Fig. IV-4 shows the bit error rate (BER) performance of the DNN demodulator, w/o compensation, and w/o RF impairments of nonlinear distortion and IQ imbalance. In w/o compensation, hard decision demodulation is performed after IFFT. Compared to w/o compensation, the DNN demodulator improves the BER performance and approaches the characteristics of the case without RF impairments. These results demonstrate that the communication quality can be improved by using the DNN demodulator for RF impairments.

Table IV-1. Simulation parameters for training and validation.

| Parameter | Value |
|---|---|
| Modulation scheme | 16-QAM, 64-QAM |
| PA Nonlinearity | Rapp model[7], $p$=2, IBO=2 dB |
| Tx and Rx IQ imbalance | Amplitude: 1 dB<br>Phase: 5° |
| Channel model | Static, exponential |
| CIR length | 4 |
| Average SNR | Training: 30 dB<br>Validation: 10 dB – 30 dB |
| FFT size | 64 |

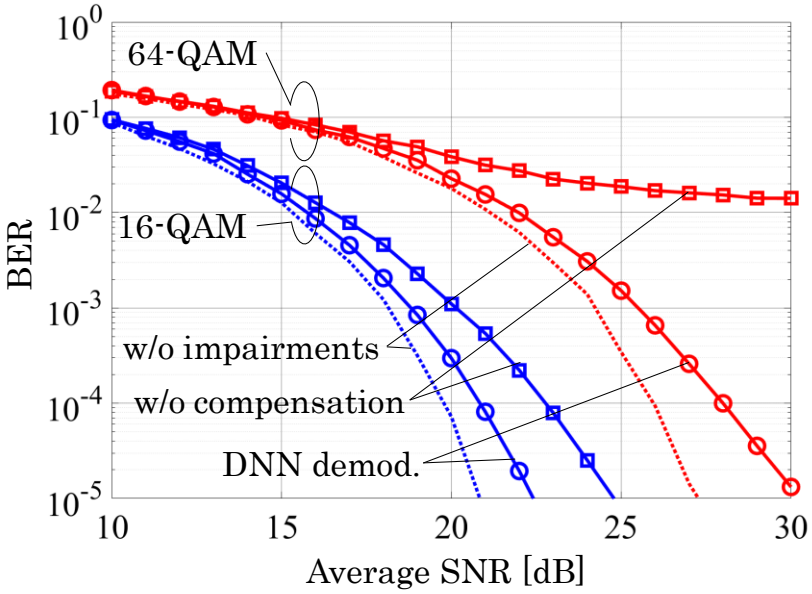


Fig. IV-4. BER performance with PA nonlinearity, IQ imbalance, and fading channel.

## IV-4. Conclusion

To popularize the use of high-frequency bands, it is desirable to optimize the trade-off between communication quality and cost reduction in accordance with the application

requirements. We introduced a conceptual overview of AI device calibration as an optimization technology that dynamically controls the calibration cost in accordance with the constraint of available hardware and the demand of the communication quality. We also proposed an AI calibration network to optimize the device calibration cost across the RAN, which is an important KPI in the sub-THz bands. Our findings demonstrated the effectiveness of the RF impairment compensation technology based on DNN as a basic technology for AI device calibration.

## REFERENCE


[1] H. Fukuzono, S. Suyama, D. Lee, D. Uchida, T. Okuyama, M. Iwabuchi, J. Mashino, and Y. Kishiyama, "Issues of Sub-Terahertz-Band Radio Access Technologies for 6G," *IEICE Tech. Rep.*, vol. 121, no. 302, RCS2021-180, pp. 30–34, Dec. 2021.

[2] U. Gustavsson et al., "Implementation Challenges and Opportunities in Beyond-5G and 6G Communication," *IEEE Journal of Microwaves*, vol. 1, no. 1, pp. 86–100, Jan. 2021. DOI: 10.1109/JMW.2020.3034648

[3] J. Pihlajasalo, D. Korpi, T. Riihonen, J. Talvitie, M. A. Uusitalo, and M. Valkama, "Detection of Impaired OFDM Waveforms Using Deep Learning Receiver," 2022 IEEE 23rd International Workshop on Signal Processing Advances in Wireless Communication (SPAWC), Oulu, Finland, 2022, pp. 1–5. DOI: 10.1109/SPAWC51304.2022.9834021

[4] K. Tanaka, K. Kuriyama, H. Hasegawa, T. Miyagi, S. Suyama, and Takayuki Yamada, "A study of calibration techniques for the use of high frequency bands," in Proc. IEICE Society Conf., B-5-46, Sept. 2023.

[5] K. Kuriyama, K. Tanaka, H. Hasegawa, T. Miyagi, S. Suyama, and Takayuki Yamada, "A Study of Compensation for RF Impairments Based on DNN in SC-FDE Transmission with Higher Frequency Bands," in Proc. IEICE Society Conf., B-5-46, Sept. 2023.

[6] M. Iwabuchi, S. Suyama, T. Arai, M. Nakamura, K. Goto, R. Ohmiya, D. Uchida, T. Yamada, and T. Ogawa, "Concept and Issues of New Radio Network Topology for 5G Evolution & 6G," *IEICE Tech. Rep.*, vol. 122, no. 235, RCS2022-148, pp. 101–106, Oct. 2022.

[7] T. Schenk, RF imperfections in high-rate wireless, Springer

## V. Sub-THz-Band Massive MIMO Technology for Beyond 5G/6G

Satoshi Suyama
NTT DOCOMO, INC.

*Abstract*— **A massive multiple-input multiple-output (M-MIMO) technology has been introduced into 5G in millimeter-wave bands such as 28 GHz. For Beyond 5G/6G, extremely high data rate exceeding 100 Gbps is required, and hence so-called sub-terahertz (sub-THz) band targeting the frequency from 100 GHz to 300 GHz has attracted much attention. This paper introduces link-level simulations of a 100 GHz-band radio access technology exploiting M-MIMO, over-100 Gbps downlink throughput and coverage performances are clarified in the sub-THz band.**

### V-1. Introduction

Higher frequency bands such as 28 GHz millimeter wave (mmW) have been introduced into 5G. It is also well known that beamforming (BF) technologies using massive multiple-input multiple-output (M-MIMO) can compensate for larger pathloss in the higher frequency bands. Towards Beyond 5G/6G, extremely high data rate exceeding 100 Gbps is expected to realize by exploiting much wider bandwidth of so-called sub-terahertz (sub-THz) wave targeting the frequency from 100 GHz to 300 GHz [1]-[3]. For realizing 5G and 6G, a variety of studies on advanced M-MIMO technologies are being carried out all over the world. NTT DOCOMO is also promoting to perform experimental trials and computer simulations for them. This paper briefly introduces studies on the M-MIMO technology for 6G. Concretely, it shows over-100 Gbps downlink (DL) throughput and coverage performances by 100 GHz-band link-level simulations employing the M-MIMO technology.

### V-2. M-MIMO Technology Based on Hybrid BF

This paper employs the M-MIMO technology based on hybrid BF scheme as shown in Fig. V-1. The scheme is joint processing of analog BF and channel state information (CSI)-based digital precoding [3], [4]. Let denote $N_T$ and L the number of antenna elements in M-MIMO and the number of analog beams in the hybrid BF, respectively. L is same as the number of up-converter (down-converter) or digital processing chains. L is set to 16, for example, in the case of $N_T = 4096$, a subarray consisting of 256 ($= N_T/L$) antenna elements generates one beam. First, the hybrid BF selects each direction of L analog beams based on the maximum received power criterion, and then the digital precoding is performed for M-MIMO streams by exploiting the estimated CSI [3].

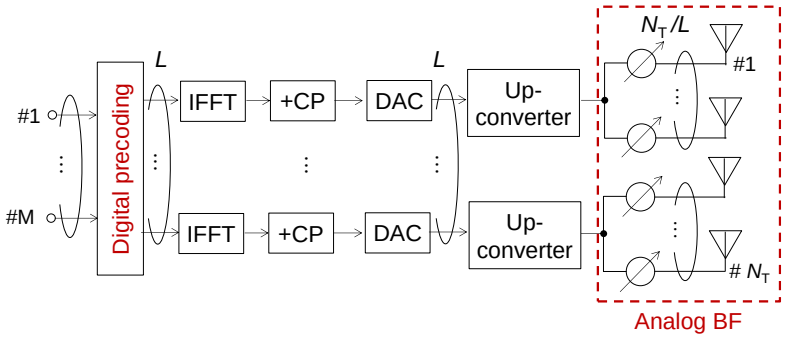


Fig. V-1. Configuration of M-MIMO based on hybrid BF.

### V-3. Performance Evaluation of 100 GHz-Band M-MIMO by Link-Level Simulations

Link-level simulations evaluate performances of sub-terahertz 100 GHz-band M-MIMO for 6G [5]. Table V-1 shows simulation specifications in the 6G link-level simulations. The performances of 5G are also evaluated in addition to 6G. The center frequency fc was set to 28 GHz and 100 GHz for 5G and 6G, respectively. A total bandwidth B = 400 MHz for 5G with 4 component carriers (CCs) and B = 6.4 GHz for 6G with 2 CCs, which is 16 times of 5G. In order to extract the full performance of MIMO transmission by the digital precoding, this paper employed OFDM as 5G and 6G radio access, and time slots in time division duplex (TDD) were all assigned to DL, in other words, the ratio of time slots in DL and uplink (UL) (TDD ratio) was 10 to 0. In 6G, the number of BS antenna elements in M-MIMO, $N_T$ is set to 256, 1024, and 4096, and the number of MS antenna elements, $N_R$ is made to be a planar array equivalent to 256 elements in which 16 uniform planar arrays with 16 elements and half-wavelength interval are arranged at 3.5-wavelength interval so as to have the same aperture size as the 5G MS antenna with 16 elements and one-wavelength interval. Note that the simulations in 6G were carried out by 16-element uniform planar array with 3.5-wavelength interval, and 12 dB was considered as an additional BF gain of MS in evaluating coverage performances. L is set to 16, for example, in the case of $N_T$ = 4096, the subarray consists of 16 elements in the horizontal direction and 16 elements in the vertical one. M is set to 16 for 5G and 4 and 8 for 6G. This simulation employed adaptive modulation and coding (AMC) using the set with the highest throughput according to the average signal-to-noise power ratio (SNR) of each stream. When the transmission efficiency considering pilot insertion loss, etc. is 0.8, the maximum throughput becomes 28.96 Gbps in 5G, 115.85 Gbps and 231.70 Gbps in 6G with M = 4 and M = 8, respectively. Since the UL throughput is expected to become important in 6G, M = 8, which can allocate the TDD ratio to the UL to some extent, is a more realistic setting.

Table V-1. SIMULATION SPECIFICATIONS

| | 5G | 6G |
|---|---|---|
| Center frequency, $f_c$ | 28 GHz | 100 GHz |
| Bandwidth, $B$ | 400 MHz | 6.4 GHz |
| No. of CCs | 4 | 2 |
| Subcarrier spacing | 60 kHz | 1920 kHz |
| No. of subcarriers | 1584 | |
| No. of FFT points | 2048 | |
| No. of BS antenna elements, $N_T$ | 256 | 256, 1024, 4096 |
| No. of MS antenna elements, $N_R$ | 16 | Comparable to 256 |
| No. of beams, $L$ | 16 | |
| No. of MSs, $N_U$ | 1 | |
| No. of streams, $M$ | 16 | 4, 8 |
| Average angle (azimuth, zenith) | Departure: (90 deg., 90 deg.) Arrival: (90 deg., 90 deg.) | |
| Angular spread (azimuth, zenith) | Departure: (5 deg., 5 deg.) Arrival: (20 deg., 20 deg.) | |
| TDD ratio | DL : UL = 10 : 0 | |
| Transmission efficiency | 0.8 | |
| Modulation scheme | QPSK, 16QAM, 64QAM, 256QAM | |
| Channel coding | Turbo code (coding rate: 1/2, 2/3, 3/4) | |
| Transmission power, $P_T$ | 30 dBm | |
| Noise power density, $N_{PD}$ | -174 dBm/Hz | |
| Noise figure, $N_f$ | 5 dB | |
| Multipath fading channel | 16-path Nakagami-Rice fading with Rice factor of 10 dB | |

## V-4. Simulation Results of 100 GHz-Band M-MIMO Technology

### V-4.1. Throughput Performances with Average SNR

Fig. V-2 shows DL throughput performances in 5G and 6G for the average received SNR at the MS antenna. From this figure, the average SNR that can achieve 100 Gbps in 6 G with $N_T$ = 256, 1024, and 4096 is 8.5 dB, 2.5 dB, and -0.5 dB, respectively. As $N_T$ increases, the BF gain improves, however, in the case of $N_T$ = 4096, the BF gain decreases with the expansion of antenna aperture size. The spectrum efficiency in 6G with M = 8 is half of that in 5G, while even in case of $N_T$ = 256, the effect of increasing the bandwidth B by 16 is large, which shows that higher throughput can be achieved compared with 5G. From these evaluation results, it was shown that the extreme wideband 6G can provide extremely higher data rate compared with 5G [5].

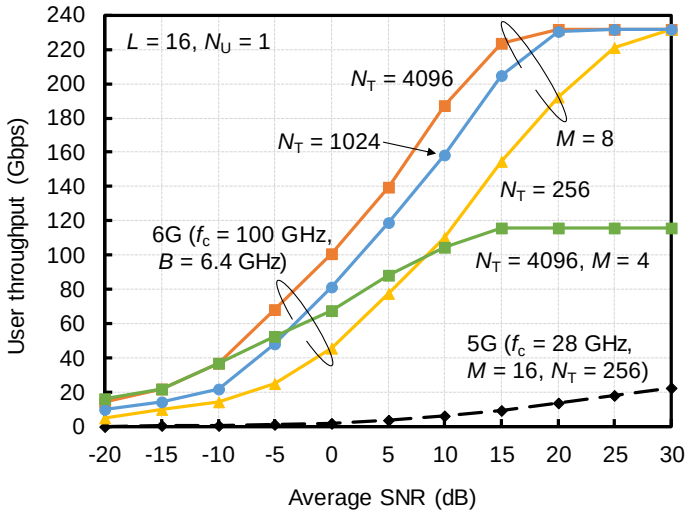


Fig. V-2. Throughput versus average SNR.

### V-4.2. Coverage Performances

By calculating the received SNR based on the link budget, the coverage performances of 6G radio access using the center frequency of 100 GHz are evaluated [5]. When the total transmission power is $P_T$ (dBm), the pathloss is $L_P$ (dB), the noise power density is $N_{PD}$ (dBm/Hz), and the noise figure is $N_f$ (dB), the received SNR $\Gamma$ (dB) is expressed as

$$\Gamma = P_T + G_{BS} + G_{MS} - L_P - (N_{PD} + 10\log_{10} B + N_f) ,$$

where $G_{BS}$ and $G_{MS}$ denote antenna (element) gains of BS and MS, respectively. Here, in consideration of the fact that the rectilinearity of 100 GHz is higher than that of 28 GHz, the pathloss $L_P$ in the LOS environment of a rural area is used [6]. In this evaluation, it was assumed that $G_{BS} = G_{MS} = 3$ dBi, and 6G considered 12 dB as the additional BF gain of MS.

Fig. V-3 shows the throughput for the distance between BS and MS as coverage performances. As a reference, the coverage performance of 28 GHz-band 5G is also shown. From this figure, the throughput of 100 GHz-band 6G decreases as the distance increases, and 6G can achieve the throughput of 100 Gbps up to the distance of 75 m for M = 4 and 120 m for M = 8. The results of M = 4 and M = 8 become closer as the distance increases. This is because the MIMO spatial multiplexing is performed under the condition that the total transmission power is constant, so that the transmission power per stream of M = 4 is twice that of M = 8. In comparison with 5G, 6G can achieve the throughput of approximately 118 Gbps even in the distance of 100 m by exploiting the extreme wideband of 6.4 GHz despite the larger pathloss, and it is proven that almost 13 times higher throughput than 5G can be achieved.

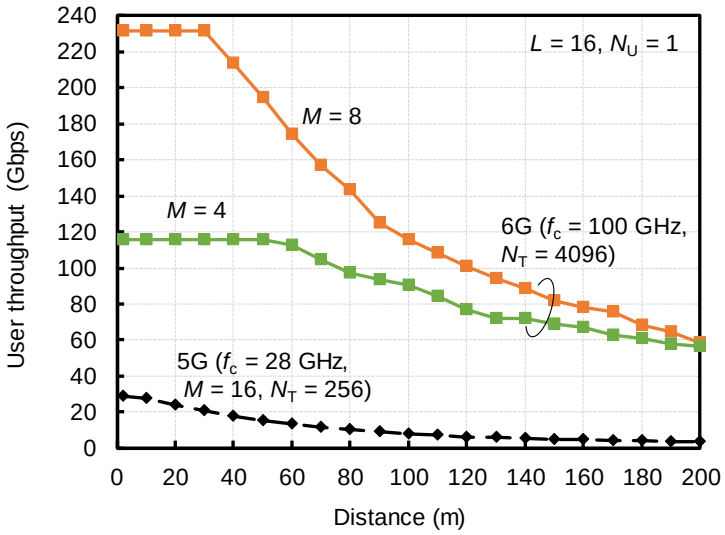


Fig. V-3. Coverage performance.

## V-5. Conclusion

For Beyond 5G/6G, this paper introduced NTT DOCOMO's recent studies on the sub-THz-band M-MIMO technologies. Link-level simulations using 100 GHz-band M-MIMO clarified that 6G can achieve extremely high DL user throughput over 100 Gbps. In addition, 100 GHz-band system-level performances have been shown by NTT DOCOMO's developed 6G simulator employing multiple base station antennas with M-MIMO in a future shopping mall environment [7].

## REFERENCE

[1] Press release from NTT DOCOMO on Jan. 24, 2020. https://www.nttdocomo.co.jp/english/info/media_center/pr/2020/0124_00.html

[2] NTT DOCOMO, INC., "White paper: 5G Evolution and 6G (version 5.0)," Jan. 2023. [Online]. Available: https://www.nttdocomo.co.jp/english/binary/pdf/corporate/technology/whitepaper_6g/DOCOMO_6G_White_PaperEN_v5.0.pdf

[3] S. Suyama, T. Okuyama, Y. Kishiyama, S. Nagata, and T. Asai, "A study on extreme wideband 6G radio access technologies for achieving 100 Gbps data rate in higher frequency bands," IEICE Trans. Commun., vol. E104-B, no. 9, pp. 992-999, Sept. 2021.

[4] T. Obara, S. Suyama, J. Shen, and Y. Okumura, "Joint processing of analog fixed beamforming and CSI-based precoding for super high bit rate massive MIMO transmission using higher frequency bands," IEICE Trans. Commun., vol. E98-B, no. 8, pp. 1474-1481, Aug. 2015.

[5] S. Suyama, T. Okuyama, N. Nonaka, and T. Asai, “Recent studies on massive MIMO technologies,” IEEE RWW2022, Jan. 2022.
[6] 3GPP, TR 38.901 (V16.1.0), “Study on channel model for frequencies from 0.5 to 100 GHz (Release 16),” Dec. 2019.
[7] T. Okuyama, S. Suyama, N. Nonaka, and T. Asai, “6G system-level simulator -Toward 100 GHz band, 100 Gbps extreme-high-data-rate communications-,” NTT DOCOMO Tech. Journal, vol. 23, no. 3, pp. 13–26, Jan. 2022.

# VI. High-Capacity Wireless Transmission Technology using Orbital Angular Momentum Multiplexing in the Sub-THz Frequency Bands

Doohwan Lee, NTT Network Innovation Laboratories, NTT Corporation
Hirofumi Sasaki, NTT Network Innovation Laboratories, NTT Corporation
Yasunori Yagi, NTT Network Innovation Laboratories, NTT Corporation
Riichi Kudo, NTT Network Innovation Laboratories, NTT Corporation

*Abstract*— **Experimental demonstrations of more than 1-Tb/s wireless transmissions based on orbital angular momentum (OAM) multiplexing using Butler matrices and parabolic reflector antennas were conducted in sub-terahertz (sub-THz) frequency bands. We designed and implemented an 8×8 Butler matrix that performs discrete Fourier transform (DFT) processing in an analog way to generate and separate OAM waves with high precision over a 32-GHz bandwidth. Also, a parabolic reflector antenna was designed and implemented to extend the transmission distance. An experiment was conducted in a shielded room, and 1.4 Tb/s wireless transmissions were achieved using eight OAM modes and dual polarization (16 signals) at distances of 1 m and 20 m—without and with parabolic reflector antennas, respectively.**

## VI-1. Introduction

As the data traffic of wireless communications continues to grow exponentially, high-capacity wireless transmissions are in great demand for many scenarios. Several generations of wireless networks have emerged and been passed on, and discussions related to the sixth generation (6G) are currently ongoing. The aggregated wireless transmission data rate in these networks has increased up to 1,000 times as the generations have migrated over the last decade, and over 200 Gb/s is expected in the next generation of wireless networks [1]. The capacity of backhaul and fronthaul connections for these networks has to be enlarged accordingly, and providing such connections wirelessly is useful in terms of the maintenance and deployment flexibility of base stations. To achieve further high-capacity wireless transmissions, we need to utilize sub-terahertz (sub-THz) bands in 6G, where a wide bandwidth is available. New technology such as orbital angular momentum (OAM) multiplexing is emerging to provide high-capacity wireless transmissions utilizing a wide bandwidth in sub-THz frequency bands.

## VI-2. OAM Multiplexing Transmission and Use Cases

OAM is one of the physical properties of electromagnetic waves characterized by a spiral phase front in the direction of propagation. The phase rotation speed of the helical phase front is called the OAM mode. The transmission capacity can be enhanced with

different data signals using different OAM modes. Fig. VI-1 (a) illustrates OAM multiplexing transmissions using three different OAM modes. This technology should enable high-capacity wireless transmissions comparable to those of optical transmission systems envisioning various applications, including wireless backhaul/fronthaul between base stations, as shown in Fig. VI-1 (b). The eventual development of this technology will likely support the creation and spread of various future services, such as virtual reality/augmented reality (VR/AR), high-definition video transmissions, connected cars, and telemedicine, as innovative wireless-communication technology in the 6G era.

(a) (b)

Fig. VI-1. (a) Illustration of OAM multiplexing transmissions, (b) Use case: complement of optical fiber connections.

## VI-3. Enabler of OAM Multiplexing in Sub-THz Frequency Bands

### VI-3.1. Butler Matrix Design for Wideband Transmissions

Electromagnetic waves with different OAM modes can be generated and separated simultaneously using a uniform circular array (UCA) with discrete Fourier transform (DFT) processing. Such processing can be performed using an analog approach [2, 3] or a digital one [4]. We chose the analog approach to reduce the digital signal processing burden and to utilize the wide bandwidth of sub-THz frequency bands fully.

Fig. VI-2 (a) shows a schematic of our designed 8×8 Butler matrix that performs DFT processing in an analog way [2]. It is composed of wideband 3-dB couplers (π/2 hybrid couplers) and phase shifters. To remove intersections of such components that degrade the ability to extend the operation bandwidth, we designed a waveguide-based multi-layer Butler matrix having two types of 3-dB coupler, one for the E-plane and one for the H-plane. Therefore, our designed Butler matrix can be implemented without any intersections. Each E-plane coupler connected by a dashed line covers two layers and is operated by fitting the two layers together. The transmission waveguides labeled Ay (y= 1, 2…8) are connected to the corresponding antenna ports that form the shape of the

UCA on the top layer. Fig. VI-2 (b) shows our implemented 8×8 Butler matrix forming the UCA that can operate over a 32-GHz bandwidth in sub-THz frequency bands.

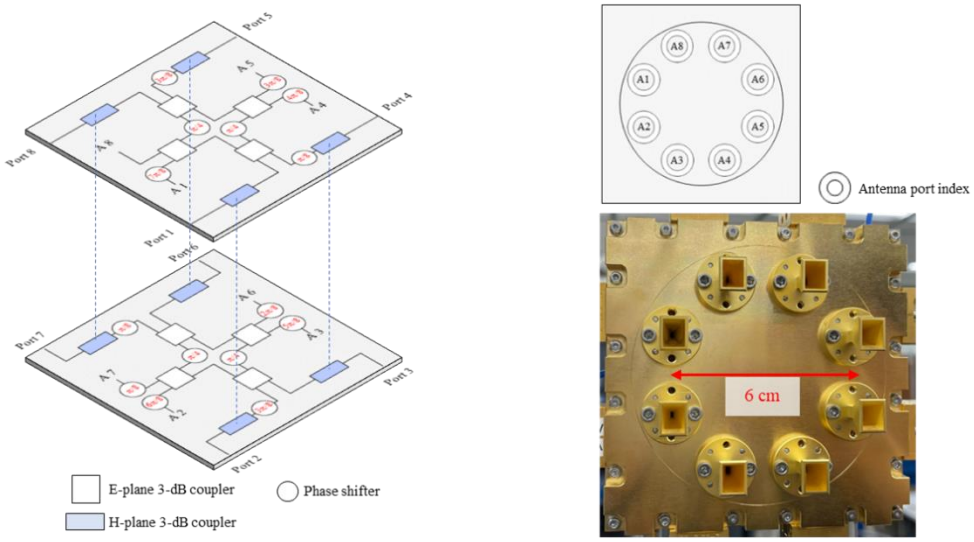


(a) (b)

Fig. VI-2. (a) Schematic design of 8×8 Butler matrix, (b) Implemented 8×8 Butler matrix forming the UCA.

### VI-3.2. Design of the Parabolic Reflector Antenna for Extending the Transmission Distance

To extend the transmission distance of the OAM waves, we developed a parabolic reflector antenna. The antenna was designed for the plane wave source of OAM waves using two paraboloidal surfaces with the same focal point and different focal lengths, as shown in Fig. VI-3 (a) [3].

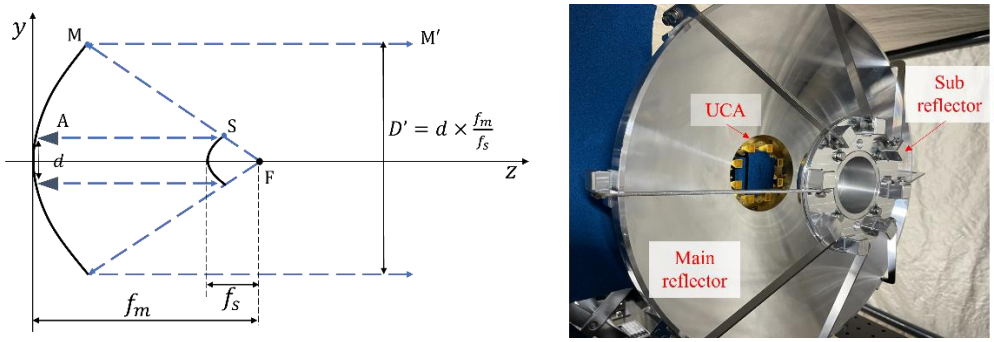


(a) (b)

Fig. VI-3. (a) Parabolic reflector design for OAM multiplexing, (b) Photograph of fabricated parabolic reflector antenna mounted with the UCA.

Because the focal point (F) is the same, a beam parallel to the axis of propagation (AS) from the feed antenna is bounced back by the two reflectors and becomes parallel again

(MM'), thereby expanding the beam diameter D'. This allows the aperture plane to be enlarged by the two reflectors. The focal length of the main reflector is $f_m$, and that of the sub-reflector is $f_s$. The aperture D' was determined to be $d \times \frac{f_m}{f_s}$. That is, the aperture of the UCA can be enlarged by a factor of $f_m/f_s$. Fig. VI-3 (b) shows our implemented parabolic reflector antenna designed for 20-m transmissions using a UCA with 6-cm diameter. The diameter of the main reflector was set to 35 cm to enlarge the aperture of the UCA by a final factor of 5 using two reflectors. A fabrication margin of 5 cm was provided to account for a slight spread.

### VI-4. Experimental Evaluations

We performed experiments transmitting OAM multiplexing signals using our designed Butler matrix and parabolic reflector in sub-THz frequency bands, as shown in Fig. VI-4 (1). Table VI-1 summarizes our experimental parameters. The transmission signals in each OAM mode were independently processed before and after the 8×8 Butler matrix in the transmitter and receiver, respectively. Therefore, equalization between the signal series in the OAM modes was not required. Fig. VI-4 (b) shows the representative constellations of the transmitted signals in the 152–168 GHz band. We found that eight different signals could be successfully transmitted using various modulation levels and channel coding rates. Bit error rates of all the transmitted signals were less than $10^{-7}$.

Table VI-1. Experimental Parameters.

| Parameters | Values | Parameters | Values |
|---|---|---|---|
| OAM modes | −4, −3, −2, −1, 0, 1, 2, 3 | Total baud rate | 16+16=32 GBd |
| Diameter of reflector | 12 cm (Sub) / 35 cm (Main) | Frame length | 32,400 symbols |
| Diameter of UCA | 6 cm | Forward error correction | BCH (Outer) / LDPC (Inner) |
| Num. of antennas | 8 elements | Equalization | SC-FDE |
| Transmission distance | 20 m | Modulation | 16 QAM, 64 QAM |
| Frequency | 136–152, 152–168 GHz | Coding rate | 1/2, 3/5, 2/3, 3/4, 4/5, 5/6 |

Table VI-2 shows the experimental results. As a reference a 1-m distance experiment was conducted using only UCAs without any parabolic reflectors. In both 1-m and-20 m distance experiments, similar transmission rates larger than 700 Gb/s over the 32 GHz bandwidth were achieved. Potential exists to further double the transmission capacity by using polarization multiplexing to achieve over 1 Tb/s. We experimentally found a total 1.4 Tb/s capacity using dual polarization at 1 m without a parabolic reflector antenna and at 20 m with the parabolic reflector antennas, respectively.

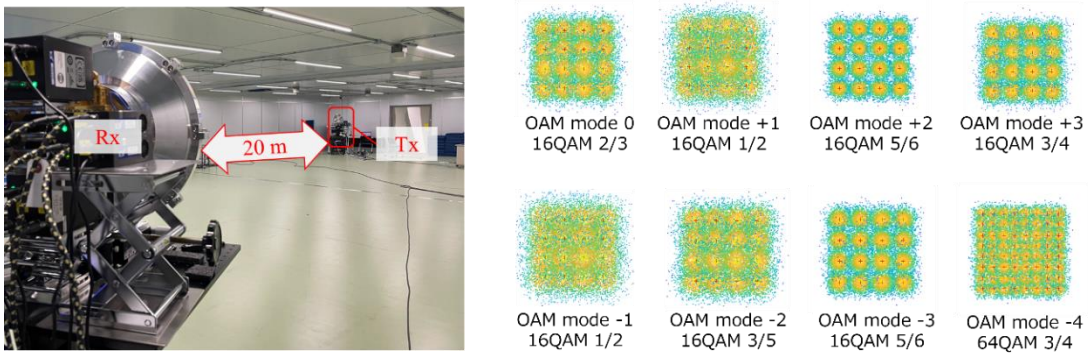


(a) (b)

Fig. VI-4. (a) Experimental environment for wireless OAM multiplexing transmissions at 20 m in a shielded room, (b) Representative constellations of the transmitted signals in the 152–168 GHz band.

Table VI-2. Experimental Results.

| Frequency Band | Transmission rates (1 m) | Transmission rates (20 m) |
|---|---|---|
| Lower (136–152 GHz) | 331 Gb/s | 335 Gb/s |
| Higher (152–168 GHz) | 390 Gb/s | 371.73 Gb/s |
| Total (136–168 GHz) | 721 Gb/s | 707.73 Gb/s |

## VI-5. Conclusion

To provide high-capacity wireless transmissions, we have been conducting research on OAM multiplexing. Thus, we designed and implemented an 8×8 Butler matrix that operates over a 32-GHz bandwidth to fully utilize a wide bandwidth in sub-THz frequency bands. To extend the transmission distance, we also designed a parabolic reflector antenna for OAM multiplexing. We experimentally showed that wireless transmissions over 1.4 Tb/s are feasible using our Butler matrix and parabolic reflector antenna.

## REFERENCE

[1] Recommendation ITU-R M.2160-0, Framework and overall objectives of the future development of IMT for 2030 and beyond. https://www.itu.int/dms_pubrec/itu-r/rec/m/R-REC-M.2160-0-202311-I!!PDF-E.pdf

[2] H. Sasaki, Y. Yagi, R. Kudo, and D. Lee, “Demonstration of 1.44 Tbit/s OAM multiplexing transmission in sub-THz bands,” in Proc. 2023 IEEE ICC Workshops, 2023.

[3] Y. Yagi, H. Sasaki, R. Kudo, and D. Lee, “Parabolic Reflector for UCA-based OAM Multiplexing in sub-THz Band and Transmission Experiment,” in Proc. 2023 IEEE GLOBECOM Workshops, 2023.

[4] N. Kamiya and E. Sasaki, “A Simple Closed-Loop Method for Compensating the Impact of Antenna Misalignment in UCA-based OAM-MIMO Systems,” in Proc. 2023 IEEE ICC Workshops, 2023.

## VII. Performance Analysis of OAM Multiplexing Using Parabolic Antenna

Shuhei SAITO[†], Yasunori YAGI[‡], Doohwan LEE[‡], and Fumiaki MAEHARA[†]
[†]Graduate School of Fundamental Science and Engineering, Waseda University
[‡]NTT Network Innovation Laboratories, NTT Corporation

***Abstract*— Utilizing a parabolic antenna enhances the transmission performance of orbital angular momentum (OAM) multiplexing. This study investigates OAM multiplexing transmission with a parabolic antenna for a link distance. We analyze the received power concerning link distance, carrier frequency, and receiving antenna radius, as well as highlight the advantages of planar reception achieved by the parabolic antenna. Additionally, we also demonstrate how OAM modes affect propagation attenuation at different link distances.**

### VII-1. Introduction

The sixth-generation mobile communication systems (6G), which are projected to materialize by 2030, are expected to have a peak data rate of 1 Tb/s [1]. Improving small-cell backhaul and access link technologies is crucial [2]. Specifically, for small-cell backhauls, line-of-sight wireless communication using fixed transmitter and receiver locations is preferred over fiber-based solutions owing to its flexibility, scalability, and cost effectiveness [2]. Orbital angular momentum (OAM) multiplexing has garnered attention for its ability to simultaneously transmit multiple data streams through a single aperture pair [3].

To enhance the multiplexing transmission performance of OAM, a method involving a parabolic antenna has been proposed and validated [4]–[6]. In [4] and [5], the transmission performance of a particular OAM mode with parabolic antennas was assessed through simulations and experiments. However, these studies did not investigate the effects of planar reception using parabolic antennas. Conversely, in [6], an analysis comparing parabolic and uniform circular array (UCA) antennas demonstrated that propagation attenuation did not depend solely on the OAM mode. However, this analysis focused on relatively short link distances. Thus, a comprehensive evaluation of parabolic antennas across a wider range of link distances is warranted.

Considering the background presented above, we investigate the multiplexing performance of OAM using parabolic antennas for a link distance [7]. In our investigation, parabolic antennas are employed in both the transmitter and receiver to enhance transmission performance. We analyze the effectiveness of planar reception facilitated by a parabolic antenna and compare it with that of UCA reception. This analysis elucidates the effects of different OAM modes on propagation attenuation at different link distances.

## VII-2. Performance Analysis of OAM Multiplexing Using Parabolic Antenna

Fig. VII-1(a) shows the phase and intensity distributions of OAM signals for modes $l$ = 1, 2, and 3. From this figure, a spiral phase with a uniform intensity distribution can be confirmed regardless of $l$. Fig. VII-1(b) illustrates OAM transmission using a parabolic antenna. The OAM signal was transmitted by reflecting it from the feed to the receiver through the parabolic antenna. At the receiver, co-phase combination by a planar antenna enhanced the received power, and the desired OAM mode can be extracted using the discrete Fourier transform. For shorter link distances, where beam divergence was less pronounced, planar reception mitigated propagation attenuation, particularly for higher OAM modes [6]. However, for longer link distances, severe beam divergence reduced the effectiveness of planar reception achieved by the parabolic antenna.

Fig. **VII-2** shows the coordinates of the OAM signal transmission using a parabolic antenna, which included the focal length $f_p$, diameter $D_p$, depth $h_p$, semi-open angle $\theta_p$ of the parabolic antenna, and radius $R_r$ for the receiving UCA or planar antenna. Additionally, a circular microstrip antenna was used as the feed for the parabolic antenna. In our analysis, we employed spherical coordinates $(r', \theta', \varphi')$ and rectangular coordinates $(x', y', z')$ at the transmitter, as well as $(r, \theta, \varphi)$ and $(x, y, z)$ at the receiver.

The electric field of the reflected OAM signal on the transmit parabolic antenna can be expressed as [6]

$$\vec{E}_r = \vec{E}_i - 2\left(\hat{n}\cdot\vec{E}_i\right)\hat{n} = -\left(\hat{r}'E_{\theta'}^{t}\sin\theta' + \hat{\theta}'E_{\theta'}^{t}\cos\theta' E_{\theta'}^{t} + \hat{\varphi}'E_{\varphi'}^{t}\right)\exp\left(-jk_0 r'\right)/r', \quad (1)$$

where $\vec{E}_i$ is the electric field of OAM signal radiated from the feed and incident on the parabolic antenna; $E_{\theta'}^{t}$ and $E_{\varphi'}^{t}$ are the $\theta'$ and $\varphi'$ components of $\vec{E}_i$, respectively; $\hat{n}$ is the normal unit vector of the parabolic antenna; $\hat{r}'$, $\hat{\theta}'$, and $\hat{\varphi}'$ are the unit vectors of

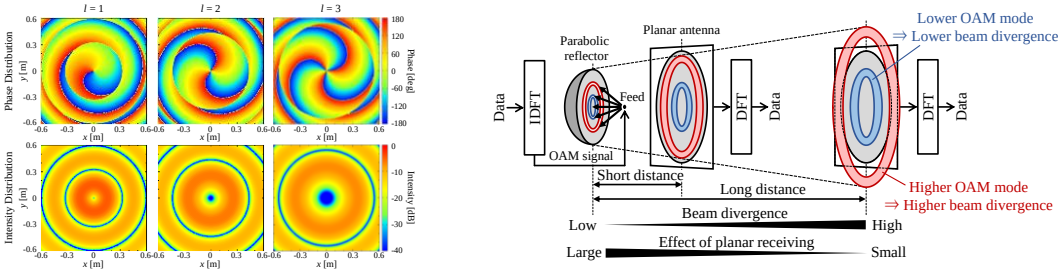


(a) Signal distributions of OAM signals (b) OAM transmission with parabolic antenna

**Fig. VII-1.** Concept of OAM transmission.

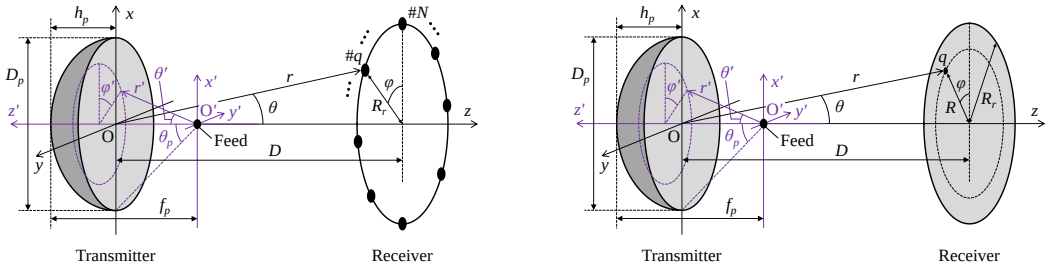


(a) UCA reception (b) Planar antenna reception

Fig. VII-2. Coordinates of OAM signal transmission employing parabolic antenna.

the spherical coordinates $(r', \theta', \varphi')$; and $k_0 = 2\pi / \lambda$ denotes the wavenumber with the wavelength $\lambda$.

At the receiver, the electric field at point $q$ of the receiving antenna can be expressed as [6]

$$\vec{E}_q = \hat{\theta} E_{q,\theta} + \hat{\varphi} E_{q,\varphi}, \tag{2}$$

$$E_{q,\theta} = \frac{-jk_0 f_p e^{-jk_0(r+f_p+h_p)}}{2\pi r}(1+\cos\theta)\int_S \tan\left(\frac{\theta'}{2}\right)\left(E^{\mathrm{t}}_{x'}\cos\varphi + E^{\mathrm{t}}_{y'}\sin\varphi\right)e^{jk_0 f_p \sin\theta\tan\left(\frac{\theta'}{2}\right)\cos(\varphi'+\varphi)}dS, \tag{3}$$

$$E_{q,\varphi} = \frac{-jk_0 f_p e^{-jk_0(r+f_p+h_p)}}{2\pi r}(1+\cos\theta)\int_S \tan\left(\frac{\theta'}{2}\right)\left(-E^{\mathrm{t}}_{x'}\cos\varphi + E^{\mathrm{t}}_{y'}\sin\varphi\right)e^{jk_0 f_p \sin\theta\tan\left(\frac{\theta'}{2}\right)\cos(\varphi'+\varphi)}dS, \tag{4}$$

$$E^{\mathrm{t}}_{x'} = E^{\mathrm{t}}_{\theta'}\cos\varphi' - E^{\mathrm{t}}_{\varphi'}\sin\varphi', \quad E^{\mathrm{t}}_{y'} = E^{\mathrm{t}}_{\theta'}\sin\varphi' + E^{\mathrm{t}}_{\varphi'}\cos\varphi', \tag{5}$$

where $S$ denotes the aperture of the parabolic antenna. Based on Eqs. (2)–(5), the received power of OAM mode $l$ with planar antenna reception, with consideration of co-phase combination, can be calculated as

$$P_{\mathrm{Planar},l} = \left|\int_0^{R_r}\left|\frac{1}{2\pi}\int_0^{2\pi}\vec{E}_q e^{-jl\varphi_q}d\varphi_q\right|dR\right|^2 = \left|\int_0^{R_r}\sqrt{\left|\frac{1}{2\pi}\int_0^{2\pi}E_{q,\theta}e^{-jl\varphi_q}d\varphi_q\right|^2 + \left|\frac{1}{2\pi}\int_0^{2\pi}E_{q,\varphi}e^{-jl\varphi_q}d\varphi_q\right|^2}dR\right|^2. \tag{6}$$

Meanwhile, the received power of OAM mode $l$ with UCA reception can be obtained as shown in [7].

## VII-3. Numerical Results

In this section, we assess the effectiveness of planar reception by comparing it with UCA reception based on various parameters, including the link distance, carrier frequency, and antenna radius. We evaluated the received power of the OAM modes ($l$ = 0, 1, ..., 4) at carrier frequencies of 80 and 300 GHz. We used a parabolic antenna with an aperture diameter $D_p$ of 0.6 m and a focal length $f_p$ of 0.4 m. For UCA reception, we employed a receiving UCA with $N$ = 16 antenna elements and assumed a negligible element size.

Fig. **VII-3** illustrates the received power versus receiving antenna radius $R$ for two different link distances ($D$ = 40 and 400 m) at a carrier frequency of $f_c$ = 80 GHz. As

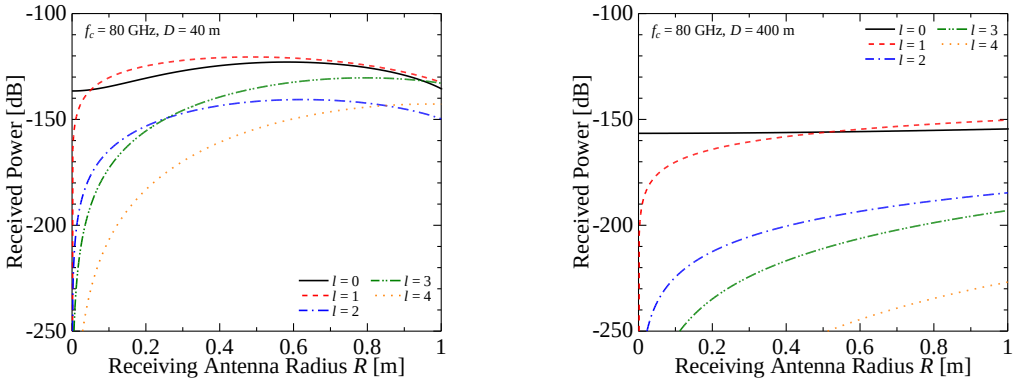


(a) $D$ = 40 m (b) $D$ = 400 m

Fig. VII-3. Received power vs. receiving antenna radius, where the carrier frequency $f_c$ = 80 GHz.

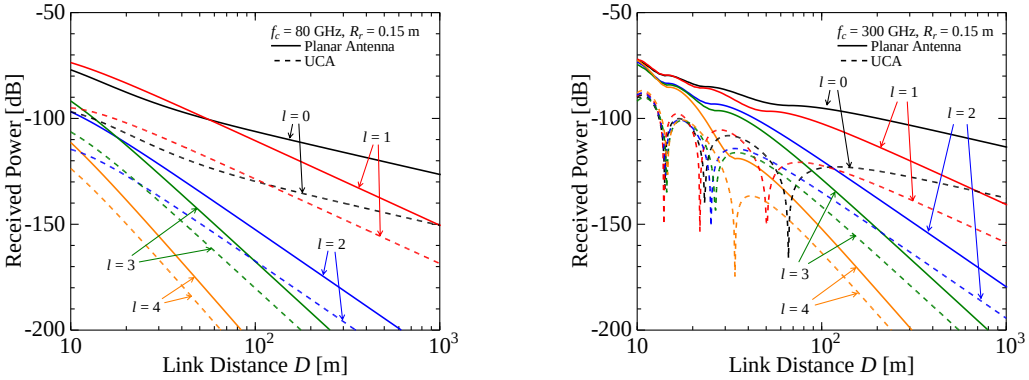


(a) $f_c$ = 80 GHz (b) $f_c$ = 300 GHz

Fig. VII-4. Received power vs. link distance, where the radius of planar antenna or UCA $R_r$ = 0.15 m.

shown in Fig. **VII-3**(a), for OAM modes $l$ = 2, 3, and 4, the received power decreased, particularly for smaller $R$ values. This reduction is due to the increasing severity of beam divergence with higher OAM modes. Conversely, as shown in Fig. **VII-3**(b), as the link distance $D$ increased to 400 m, the effect of beam divergence was more significant than that of the case involving $D$ = 40 m presented in Fig. **VII-3**(a), which resulted in a lower received power for higher OAM modes regardless of $R$. Therefore, using a parabolic antenna can mitigate the propagation attenuation, particularly for short link distances.

Fig. **VII-4** depicts the received power versus the link distance $D$ for each OAM mode $l$ under a fixed antenna radius ($R_r$ = 0.15 m) for both the planar and UCA antennas. As presented in Fig. **VII-4**, the planar antenna consistently yielded a higher received power than the UCA, irrespective of the $f_c$ and $D$, owing to planar reception. Furthermore, adopting planar reception uniformly reduced the propagation attenuation over short link distances owing to the reduced beam divergence, particularly at high carrier frequencies such as $f_c$ = 300 GHz. Conversely, at lower carrier frequencies or longer link distances, the propagation attenuation became mode-dependent regardless of the antenna type, owing to severe beam divergence.

## VII-4. Conclusion

In this study, we examined the effect of link distance on OAM multiplexing performance using a parabolic antenna. Our key finding was that planar reception outperformed UCA reception for a link distance. The numerical results indicated that adopting a planar antenna consistently improved the received power for all OAM modes regardless of the link distance or carrier frequency, owing to its planar reception properties. Shorter link distances exhibited reduced propagation attenuation owing to the lower beam divergence, where OAM signals appeared primarily near the propagation axis. Conversely, longer link distances experienced greater propagation attenuation even when parabolic antennas were used, particularly at higher OAM modes, owing to severe beam divergence.

## REFERENCE


[1] Z. Zhang et al., "6G wireless networks: Vision, requirements, architecture, and key technologies," IEEE Vehicular Technology Magazine, vol. 14, no. 3, pp. 28–41, Sept. 2019.

[2] Z. Pi, J. Choi, and R. Heath, "Millimeter-wave gigabit broadband evolution toward 5G: Fixed access and backhaul," IEEE Communications Magazine, vol. 54, no. 4, pp. 138–144, Apr. 2016.

[3] D. Lee, H. Sasaki, H. Fukumoto, K. Hiraga, and T. Nakagawa, "Orbital angular momentum multiplexing: An enabler of a new era of wireless communications," IEICE Transactions on Communications, vol. E100-B, no. 7, pp. 1044–1063, July 2017.

[4] T. Nguyen, R. Zenkyu, M. Hirabe, T. Maru, and E. Sasaki, "A study of orbital angular momentum generated by parabolic reflector with circular array feed," Proc. 2016 International Symposium on Antennas and Propagation (ISAP 2016), pp. 708–709, Oct. 2016.

[5] Y. Yao, X. Liang, W. Zhu, J. Geng, and R. Jin, "Experiments of orbital angular momentum phase properties for long-distance transmission," IEEE Access, vol. 7, pp. 62689–62694, May 2019.

[6] Q. Wu, X. Jiang, and C. Zhang, "Attenuation of orbital angular momentum beam transmission with a parabolic antenna," IEEE Antennas and Wireless Propagation Letters, vol. 20, no. 10, pp. 1849–1853, Oct. 2021.

[7] S. Saito, Y. Yagi, D. Lee, and F. Maehara, "Link distance and carrier frequency dependence of propagation attenuation in OAM multiplexing using parabolic antenna," Proc. 2023 IEEE Annual International Symposium on Personal, Indoor and Mobile Radio Communications (PIMRC 2023), pp. 1–5, Sept. 2023.

## VIII. Antenna Array Module for Sub-THz Communications

Shiro Ozaki, Fujitsu Limited
Takuichi Hirano, Tokyo City University

***Abstract*—For sub-THz communication applications, we developed an antenna array module with element pitch less than 1 wavelength (1λ) at 300 GHz. The 1 × 4 waveguide-based antenna array module showed an antenna gain of 10 dBi and a beam steering angle of ±10° with reduced grating lobes.**

### VIII-1. Introduction

Sub-THz bands, particularly the 300-GHz band, are considered as one of candidates for next-generation wireless communications [1]. For the sub-THz indoor use case shown in Fig. VIII-1 [2], it is essential for the access point to perform beamforming with antenna arrays. The large grating lobes have been a critical issue to realize practical antenna arrays. This is because the size of active devices such as power amplifiers (PAs) tend to be large for the sub-THz wavelengths (λs), i.e. 1 mm at 300 GHz [3]. In this study, we demonstrated an antenna array module with element pitch less than 1λ for reducing grating lobes.

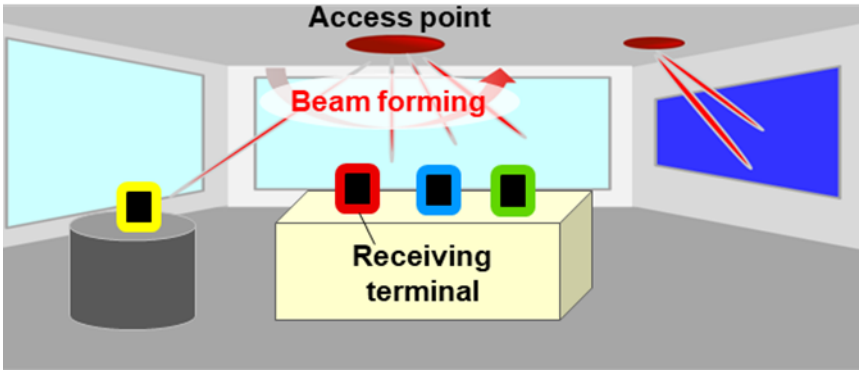


Fig. VIII-1. Indoor use case of 300-GHz band wireless communications (Reprinted with permission from [2], copyright 2023 IEEE)

### VIII-2. Demonstration of 1 × 4 Antenna Array

Fig. VIII-2 [2] illustrates the proposed 1 × 4 antenna array module. 4-element waveguide antennas and PAs are integrated heterogeneously in the module. Sub-THz signals propagate on microstrip lines (MSLs) formed on a printed substrate. The PAs are mounted on the printed substrate by flip chip assembly. In addition to these technologies for heterogeneous integration, we are developing PA monolithic microwave integrated circuit using InP-based metal-oxide-semiconductor high-electron-mobility transistors (MOS-HEMTs) [4, 5] to achieve high equivalent isotropic radiation power.

Herein, a waveguide-based antenna array (without PAs) was fabricated with an element pitch of only 0.7 mm. In Fig. VIII-3(a) [2], the aperture area of each waveguide antenna was 0.6 mm × 0.432 mm. The thickness of metal walls between the aperture area was designed to be 0.1 mm to achieve the element pitch of 0.7 mm. Polyimide was used as a printed substrate by considering low transmission loss (low dielectric constant and low loss tangent) and a design rule for heterogeneous integration with PAs: high-density through-hole vias for ground pads used in flip chip mounting. To suppress radiation from the substrate at 300 GHz, the pitch of ground vias are required less than 0.1 mm (0.1λ) [6]. At the MSL-Waveguide transition, the width of the polyimide substrate was designed to be 0.2 mm in the floating state (Fig. VIII-3(b) [2]). In this case, the thickness of the polyimide substrate and the width of the signal line formed on the substrate were 25 and 50 μm, respectively to be the characteristic impedance of 50 Ω.

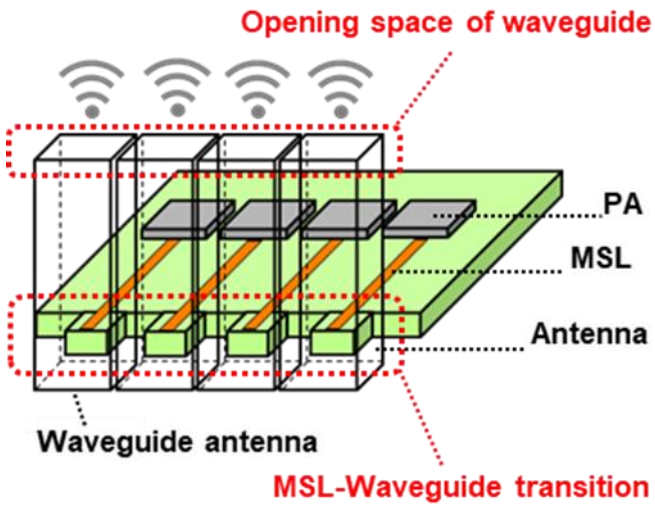


Fig. VIII-2. Proposed 1 × 4 antenna array module with PAs (Reprinted with permission from [2], copyright 2023 IEEE)

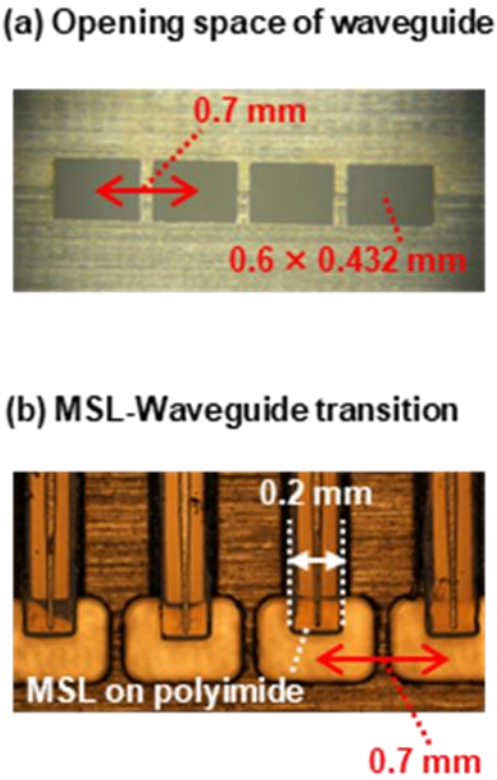


Fig. VIII-3. Photograph of the developed 1 × 4 antenna array module (Reprinted with permission from [2], copyright 2023 IEEE)

The performance of the developed 1 × 4 antenna array module is shown in Fig. VIII-4 [2]. The developed antenna array achieved a gain of 10 dBi and a beam steering angle of 10° by varying the phase difference between each port from 0° to 45° (Φ1 = 0°, Φ2 = 45°, Φ3 = 90°, Φ4 = 135°), which is in good agreement with electro-magnetic simulation. Moreover, simulations revealed that the beam can be steered by ±24° by varying the phase difference between each port from 0° to 120° (Φ1 = 0°, Φ2 = ±120°, Φ3 = ±240°, Φ4 = ±360°), as shown in Fig. VIII-5 [2]. This phase shift reduced the antenna gain from 10.6 to 9.35 dBi and increased the grating lobe level to 1.95 dB at ±54°. By reducing the element pitch to be less than 1 mm, the grating lobes of the antenna array module were successfully reduced compared to previous report [7] that used horn antennas with an element pitch of 1.25 mm.

(a) Normalized gain pattern obtained from simulation

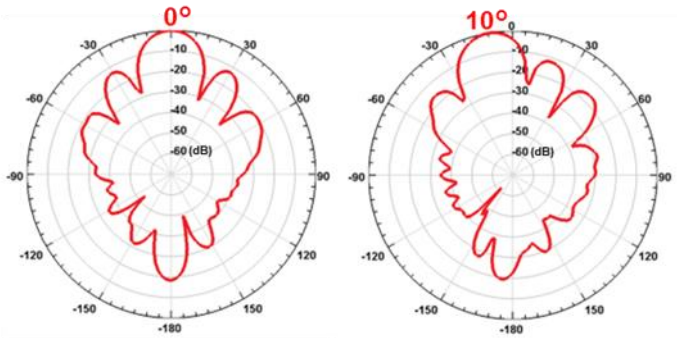


(b) Comparison of simulation and experiment

| Beam steering angle (°) | Antenna gain (dBi) | |
|---|---|---|
| | Simulation | Experiment |
| 0° | 10.6 | 10.1 |
| 10° | 10.6 | 10.3 |

Fig. VIII-4. Performance of the developed 1 × 4 antenna array module (Reprinted with permission from [2], copyright 2023 IEEE)

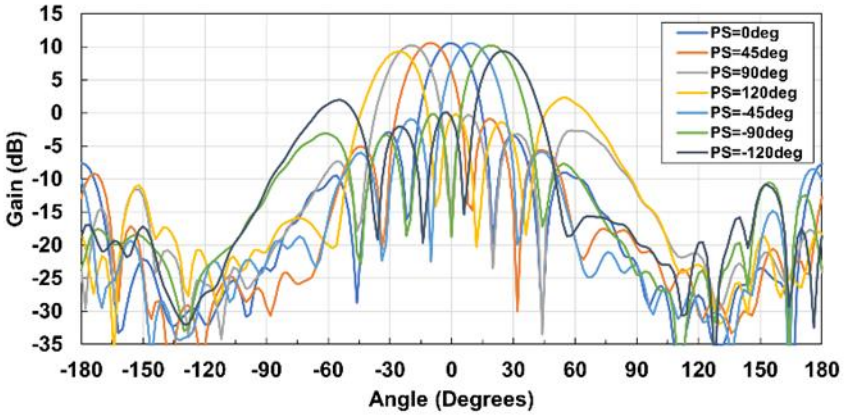


Fig. VIII-5. Performance of the developed 1 × 4 antenna array module (Reprinted with permission from [2], copyright 2023 IEEE)

### VIII-3. Conclusion

Herein, an antenna array module with element pitch less than 1λ at 300 GHz was developed for sub-THz communication applications. The 1 × 4 waveguide-based antenna array module exhibited a gain of 10 dBi and a beam steering angle of ±10°. By electromagnetic simulation, it was confirmed that the beam can be steered by ±24° by varying the phase difference between each port from 0° to ±120°.

### VIII-4. Acknowledgements

This work was partially supported by "R&D on THz band ultra high-capacity wireless communications for beyond 5G (No.00301)" from the commissioned research by National Institute of Information and Communications Technology (NICT), and "The research and development project for the expansion of radio spectrum resources (JPJ000254)" of the Ministry of Internal Affairs and Communication, Japan.

### REFERENCE

[1] V. Petrov et al., "First Standardization Efforts for Sub-Terahertz Band Communications toward 6G," IEEE Communications Magazine, vol. 58, no. 11, pp. 28-33, Nov. 2020.

[2] S. Ozaki et al., "A Waveguide Antenna Array Module with Controlled Element Pitch < 1λ for Sub-THz Communications," CAMA, pp.281-284, Nov. 2023.

[3] T. Hirano, "Series-Fed Printed-Dipoles With a Director for Substrate Lateral Radiation," ISAP, pp.537-538, Oct. 2022.

[4] Y. Kumazaki et al., "High-Efficiency 250-320 GHz Power Amplifiers Using InP-Based Metal-Oxide-Semiconductor High-Electron-Mobility Transistors," IEICE Transactions on Electronics, 2023MMP0005, Aug. 2023.

[5] S. Ozaki et al., "Improved $f_T/f_{max}$ in wide bias range by steam-annealed ultrathin-Al2O3 gate dielectrics for InP-based high-electron-mobility transistors," Appl. Phys. Express 15, 041001, Mar. 2022.

[6] Y. Kawano et al., "Flip chip assembly for sub-millimeter wave amplifier MMIC on polyimide substrate," MTT-S, pp.1-4, Jun. 2014.

[7] S. Rey et al., "A Phased Array Antenna with Horn Elements for 300 GHz Communications," ISAP, pp.122-123, Oct. 2016.

# IX. Virtualized terminal technologies for high-capacity communications in Beyond 5G era

Satoshi Ito, KDDI Research, Inc.
Yoshio Kunisawa, KDDI Research, Inc.
Takahiro Hayashi, KDDI Research, Inc.
Yoshiki Sugimoto, Nagoya Institute of Technology
Kunio Sakakibara, Nagoya Institute of Technology
Nobuyoshi Kikuma, Nagoya Institute of Technology

***Abstract*— In anticipation of the Cyber Physical Systems (CPSs) integration in 2023, this paper presents a "virtualized terminal" concept for enhanced uplink capacity in beyond 5G networks to overcome the space and power constraints of conventional MIMO systems. Operating in the subterahertz band, the proposed architecture includes offloading antenna functions to relay devices (RDs), thus enabling high-capacity data transmission. The experimental results show a 19.2 Gbps transmission rate. Future work will seek to achieve the Beyond 5G target of 100 Gbps through advanced component miniaturization and leveraging a network of five RDs.**

## IX-1. Introduction

As 2030 approaches, the integration of physical and cyber spaces, which is known as Cyber Physical System (CPS), is expected [1]. Upon realizing the broad integration a CPS, there will be an increased demand for uploading large amounts of data to networks. Consequently, there will be a greater need for high-capacity uplink transmission capabilities than ever before. MIMO is considered to be a method for enhancing uplink capacity, but challenges such as the space required for antenna installation and the power consumption of amplifiers limit the increase in the number of antennas that can be achieved within devices. Therefore, the present study explores the concept of a "virtualized terminal" that relocates the antenna functionality within a device to surrounding wireless devices to communicate with base stations, thereby enabling high-capacity uplink communication [2]. This paper presents the conceptual and architectural overview such a virtualized terminal, including utilization of the subterahertz band, and reports the current status of proof-of-concept experiments for virtualized terminals.

## IX-2. Virtualized terminal technologies

The proposed virtualized terminal is shown in Fig. IX-1. This virtualized terminal consists of user equipment (UE) with which the user directly interacts with, as well as multiple relay devices (RDs), which are installed in wearable devices. This configuration enables spatial multiplexing transmission with many antennas without constraint from

the installation space or power consumption within the UE. The communication between the virtualized terminal and the base stations is assumed to utilize the 40 GHz band (37.0 GHz to 43.5 GHz), which is being considered for allocation to 5G in the Frequency Reorganization Action Plan of Japan [3].

The virtualized terminal is intended to achieve a data rate of 100 Gbps, which is anticipated for use in Beyond 5G [1] applications, by transmitting 10 streams using a QPSK modulated signal with a 4.8 GHz bandwidth to five RDs that support orthogonal dual polarization multiplexing. However, due to interference concerns, it is difficult to use the millimeter-wave band simultaneously for communication between the UE and the RDs, which is also used for communication with the base stations. Therefore, the virtualized terminal uses different frequency bands for wireless transmission from the UE to each RD in the subterahertz band allocated to land mobile services by the ITU-R, ranging from 252 GHz to 296 GHz [4]. While a total bandwidth of 24 GHz is required for the five RDs, the abovementioned subterahertz band can potentially provide a 44 GHz bandwidth, which is a sufficient capacity even when accounting for guard bands.

Moreover, large path loss is a critical issue in subterahertz band communication. However, the expected propagation distance in the virtualized terminal configuration is approximately 1 m in the subterahertz band, and it is anticipated that frequency conversion to the millimeter-wave band will enable communications over distances of more than 100 m to the base station [5]. An example of the link budget design is shown in Fig. IX-2. The transmission power for the subterahertz band is based on values from previous research, while the millimeter-wave band uses values equivalent to 5G, with a simple model using free space path loss applied. In this example, transmission from the UE to the RD over a distance of 0.9 m in the subterahertz band and subsequent transmission over a distance of 100 m to the base station in the millimeter-wave band using QPSK are both feasible.

Fig. IX-3 shows an example of the configuration of the virtualized terminal. In the UE, baseband signals for each RD are converted to different frequencies in the subterahertz band by the subterahertz band front-end component. Signals in each subterahertz band are radiated toward each RD by a multibeam antenna. The RDs convert the received subterahertz band signals from the UE into frequencies used in the millimeter-wave band for communication with the base station and then radiate these signals from the millimeter-wave band antennas. By using all RDs to emit radio waves at the same frequency in the millimeter-wave band toward the base station, the virtualized terminal is configured with multiple antennas realized by the RDs.

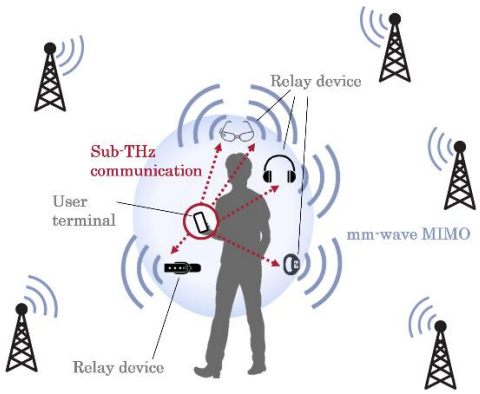


Fig. IX-1. Concept of a virtualized terminal.

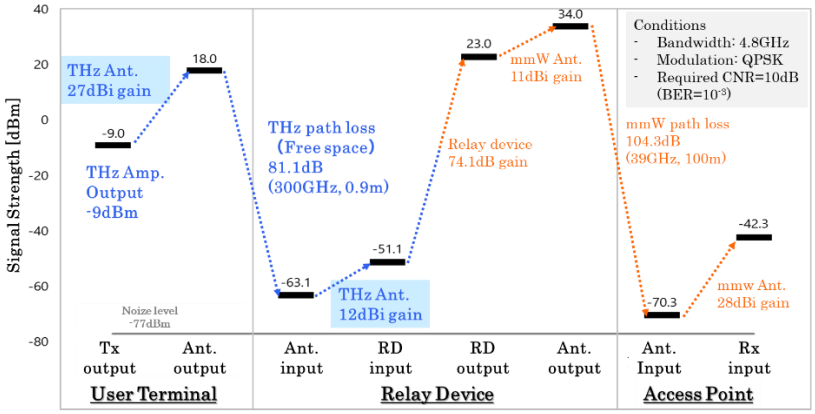


Fig. IX-2. Link budget for the virtualized terminal.

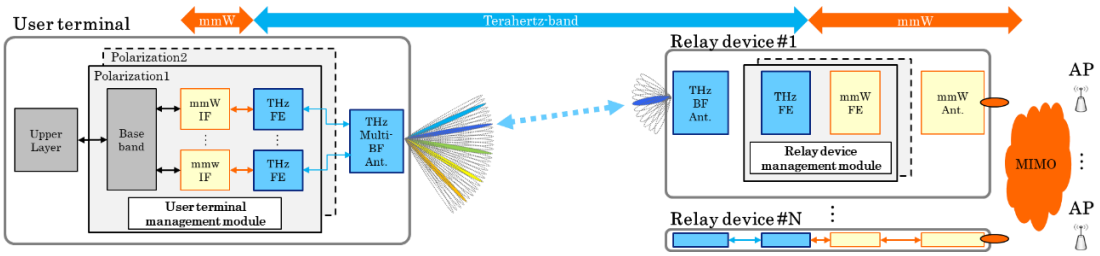


Fig. IX-3. Structure of the virtualized terminal.

### IX-3. Demonstration experiment

To evaluate a wireless communication system using a virtualized terminal, a proof-of-concept experiment was conducted with a measurement system comprising two transmitters and two receivers in the subterahertz band and a multibeam lens antenna [6].

Fig. IX-4 shows the measurement system used for the proof-of-concept experiment. An arbitrary waveform generator (AWG) was used to generate a 4.8 GHz bandwidth OFDM signal with a center frequency of 37.5 GHz, modulated with two different data sequences, which was subsequently input into two subterahertz band transmitters. The distance between the subterahertz band transmitting and receiving antennas was set to 20 cm for channel 1 and 33 cm for channel 2. The modulated signals from the transmitters were received by two receivers via a subterahertz band multibeam antenna, frequency-converted to the millimeter-wave band, level-adjusted, and subsequently fed to the vertical and horizontal polarization ports of an orthogonal dual-polarization antenna for radiation in the millimeter-wave band. On the base station side, the signals received by the dual-polarization antenna were amplified by a low-noise amplifier (LNA) and subsequently input into two channels of an oscilloscope for vertical and horizontal polarization. After demodulating the OFDM signal, the bit error rate (BER) was calculated from the demodulated QPSK signals. The results were subsequently used to calculate and evaluate the physical transmission rate for the 4.8 GHz bandwidth.

Fig. IX-4 also shows the constellation and power spectrum of the received signal when the millimeter-wave band propagation distance is 10 m. As shown in the figure, the physical transmission rate for both channel 1 and channel 2 was approximately 9.6 Gbps, for a combined total of 19.2 Gbps. This finding indicated that with five RDs supporting dual polarization, it is feasible to realize the 100 Gbps equivalent required for Beyond 5G. However, the received signal exhibited a difference of more than 10 dB within the signal transmission band, and the constellation was dispersed. In this demonstration, discrete RF components were used, but it is expected that the use of MMIC (Monolithic Microwave IC) will lead to an improvement to the in-band frequency characteristics.

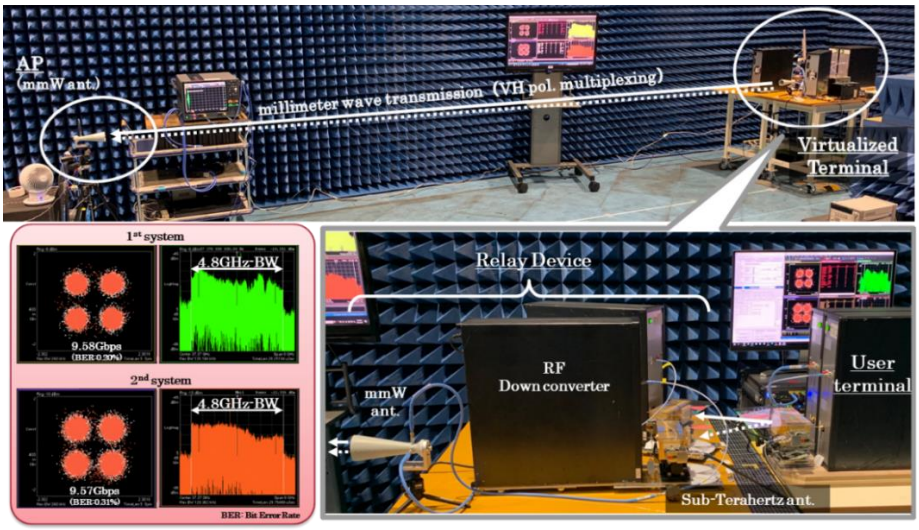


Fig. IX-4. Experimental setup.

## IX-4. Conclusion

This paper reports the conceptual and architectural overview of a virtualized terminal utilizing the subterahertz band to achieve high-capacity uplink communication. The data confirmed that by frequency-converting subterahertz band QPSK signals to the millimeter-wave band using RDs and wirelessly relaying these signals through two systems, a physical transmission rate of 19.2 Gbps was achieved, as calculated from the bit error rate (BER) at a millimeter-wave transmission distance of 10 m. Future advancements to this work will continue the miniaturization and enhancement of subterahertz band RF components by introducing MMIC technology. This improvement is to facilitate a physical transmission rate of 100 Gbps by implementing wireless transmission through ten channels using a configuration of five RDs. Therefore, the proposed system is intended to achieve a physical transmission rate equivalent to the 100 Gbps by conducting wireless transmission across ten systems using five RDs.

## IX-5. Acknowledgements

These research results were obtained from the commissioned research (JPJ012368C00401) by National Institute of Information and Communications Technology (NICT), Japan.

## REFERENCE

[1] Beyond 5G Promotion Consortium White Paper Subcommittee, "Beyond 5G White Paper," Mar. 2023, https://b5g.jp/en/output/

[2] KDDI, KDDI Research, Inc., "Beyond 5G/6G White Paper ver.2.0.1," Oct. 2021, https://www.kddi-research.jp/english/tech/whitepaper_b5g_6g/

[3] Ministry of Internal Affairs and Communications Japan, "Solicitation of Opinions on Draft Frequency Reorganization Action Plan (Fiscal 2022 Version)," https://www.soumu.go.jp/main_sosiki/joho_tsusin/eng/pressrelease/2022/9/01_03.html

[4] ITU-R, "World Radiocommunication Conference 2019 Final Acts," https://www.itu.int/dms_pub/itu-r/opb/act/R-ACT-WRC.14-2019-PDF-E.pdf

[5] Y. Kunisawa and Y. Amano, "Virtualized terminal utilizing terahertz band radio waves for Beyond 5G : Link budget analysis," IEEE VTC2022-Spring, June. 19-22, 2022. DOI: 10.1109/VTC2022-Spring54318.2022.9860515

[6] T. Sugiyama, Y. Sugimoto, K. Sakakibara and N. Kikuma, "Low-profile Multi-beam Lens Antenna with Corrugation to Suppress Surface Reflection of High-permittivity Material in 300 GHz Band," 2023 IEEE International Symposium on Antennas and Propagation, Oct. 2023, Kuala Lumpur, Malaysia.

# X. Sub-THz multi-beam antennas for virtualized terminal technologies

Kunio Sakakibara, Nagoya Institute of Technology
Yoshiki Sugimoto, Nagoya Institute of Technology
Satoshi Ito, KDDI Research, Inc.
Yoshio Kunisawa, KDDI Research, Inc.
Takahiro Hayashi, KDDI Research, Inc.
Nobuyoshi Kikuma, Nagoya Institute of Technology

***Abstract*—Various multi-beam antennas are in the development at Sub-THz band. Plano-convex lenses are potentially capable to design in lower profile. Spherical lenses essentially never generate scan loss. Rotman lens arrays are low-profile planar antennas. These multi-beam antennas are proposed to apply to the virtualized terminal technologies of user-centric architecture for future beyond 5G/6G systems.**

## X-1. Introduction

The sub-terahertz band is attracting attention for next-generation mobile communication beyond 5G/6G. Developments are strongly driven in wide range of technical fields including antennas and propagation. However, due to its high propagation loss of sub-terahertz waves, it is not easy to apply MIMO technologies which utilizes in multipath environments. One possible way to utilize sub-terahertz communication can be a virtualized terminal technology [1]. This report demonstrates the antenna performances required for the virtualized terminal technologies and presents the status of multi-beam antennas currently under development.

## X-2. Required function of Sub-THz antennas for virtualized terminal technologies

A user-centric architecture has been proposed to improve the communication quality and to extend the service area for future cellular systems [2]. MIMO communication technologies are widely used in various wireless communication systems such as cellular systems and WiFi. MIMO antennas in a user terminal are extended out to the surrounding area around the user terminal in the virtualized terminals of a user-centric architecture as shown in Fig. X-1. The user terminal and the relay devices are connected by high-speed sub-terahertz communications with narrow-beam antennas.

There are multiple relay devices for one user terminal. Therefore, as shown in Fig. X-2, a multi-beam antenna with independent beam-scanning is required for the user terminal. On the other hand, relay devices require a beam scanning function in a single beam.

Various beam scanning antennas have been proposed in general. Low-profile planar antennas are advantageous for installation in user terminals and relay devices. However, the feeding loss of the transmission line is serious in the sub-terahertz band. Lens

antennas perform very well. However, the focal length and the lens thickness cannot be avoided essentially. Lens antennas can still be candidates because high gain is obtained even with a small size.

Mechanical scanning using a lens antenna and phased array using a planar antenna are possible. However, we decided to develop a dielectric lens multi-beam antenna for user terminals and a planar multi-beam antenna with a Rotman lens for relay devices.


Fig. X-1. Virtualized terminal technologies for user-centric architecture

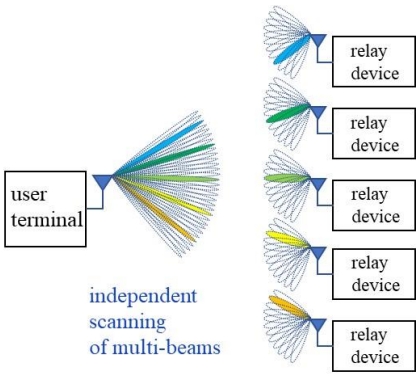


Fig. X-2. Simultaneous communication between a user terminal and relay devices

### X-3. Plano-convex dielectric lens multi-beam antennas

A lens antenna can scan the beam by shifting the position of the primary radiator from the focal point of the lens. A multi-beam antenna was developed by arranging eight horn antennas in an arc around the focal point of a plano-convex polypropylene lens ($\varepsilon_r = 2.4$) with a diameter of 10mm as shown in Fig. X-3(a). The radiation patterns are presented in Fig. X-3(b). Eight beams with a pitch of approximately 7.5 degrees cover ±30 degrees with a gain higher than 22.8dBi [3].

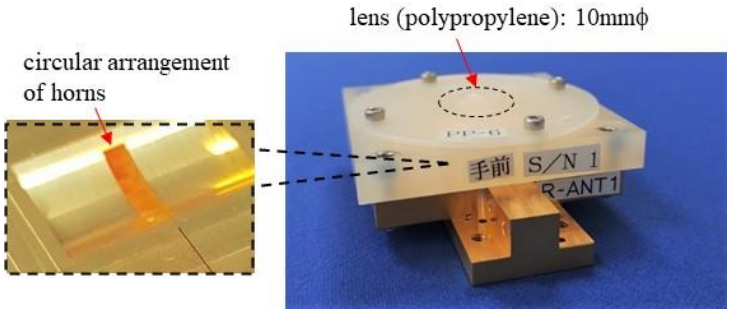


Fig. X-3 (a) Developed plano-convex multi-beam lens antenna.

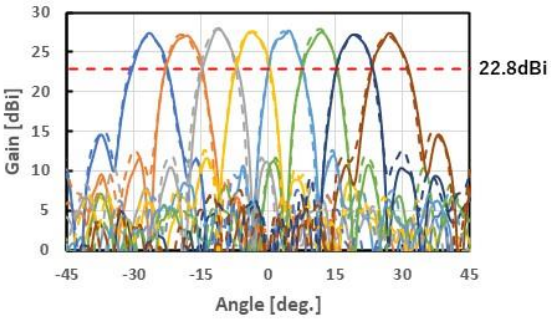


Fig. X-3 (b) Multi-beam radiation patterns and gains of the plano-convex lens antenna.

## X-4. Spherical dielectric lens multi-beam antennas

Plano-convex lenses have the problem of scan loss due to the reduction of projected aperture size and the spill over. Since the Luneberg lens has a point-symmetric structure, scan loss is not generated in principle [4]. However, it requires a layered structure in the radial direction, which is not practical in the sub-terahertz band due to manufacturing constraints. Therefore, we developed a spherical lens multi-beam antenna. Although the focusing performance is degraded, the manufacturing is practical. A multi-beam antenna is formed by arranging 16 horn antennas around the focus of the polypropylene spherical lens with a diameter of 20mm as shown in Fig. X-4(a). The multi-beam radiation patterns with the gains are presented in Fig. X-4(b). Peak gain higher than 30dBi was obtained. Sixteen beams with a pitch of approximately 4 degrees cover ±30 degrees with a gain higher than 26.7dBi [5].

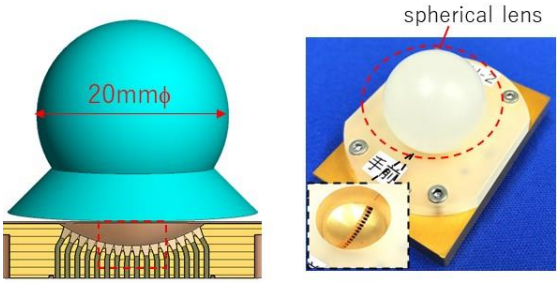


Fig. X-4. (a) Spherical lens multi-beam antenna.

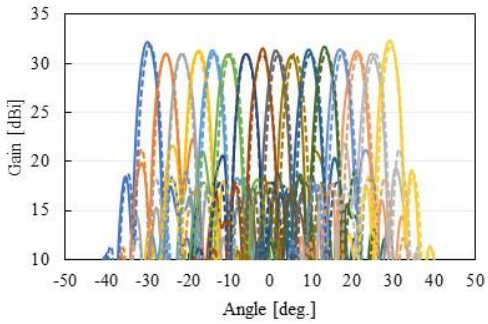


Fig. X-4 (b) Multi-beam radiation patterns and gains of the spherical lens antenna.

## X-5. Rotman lens multi-beam antennas

Planar antennas have the advantage of low-profile. A compact multi-beam antenna was designed to compose Rotman-lens beam-forming circuit on the back of the microstrip array antennas as shown in Fig. X-5(a). The antenna can be fabricated in multi-layer substrate. Two transmission line transitions were designed to connect the components. The transition between substrate-integrated waveguide (SIW) and microstrip line is used to connect the microstrip array and the Rotman lens. The transition between the waveguide and SIW is used at the feeding from the back. As a result of electromagnetic simulation, five-beam characteristics with a 12-degree pitch was confirmed as shown in Fig. X-5(b) [6].

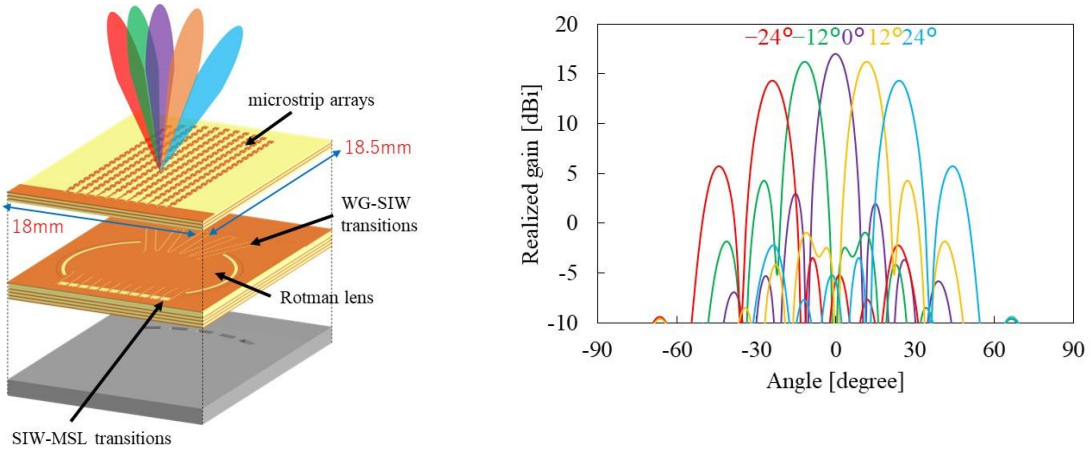


(a) Configuration (b) Multi-beam radiation patterns

Fig. X-5. Rotman-lens multi-beam planar antenna.

## X-6. Conclusion

We are in the development of multi-beam antennas for virtualized terminal technologies of user-centric architecture expected for future beyond 5G/6G. We continue

our development efforts to lower the profile of lens antennas and to improve efficiency of planar antennas.

### X-7. Acknowledgements

These research results were obtained from the commissioned research (JPJ012368C00401) by National Institute of Information and Communications Technology (NICT), Japan.

### REFERENCE

[1] KDDI Corporation, KDDI Research, Inc., "Beyond 5G/6G whitepaper," Mar. 2021.

[2] K. Yamazaki, T. Ohseki, Y. Amano, H. Shinbo, T. Murakami and Y. Kishi, "Proposal for a User-Centric Ran Architecture Towards Beyond 5G," 2021 ITU Kaleidoscope: Connecting Physical and Virtual Worlds (ITU K), Geneva, Switzerland, 2021, pp. 1-7.

[3] T. Sugiyama, Y. Sugimoto, K. Sakakibara and N. Kikuma, "Low-profile Multi-beam Lens Antenna with Corrugation to Suppress Surface Reflection of High-permittivity Material in 300 GHz Band," 2023 IEEE International Symposium on Antennas and Propagation, Oct. 2023, Kuala Lumpur, Malaysia.

[4] G. Peeler and H. Coleman, "Microwave stepped-index luneberg lenses," in IRE Transactions on Antennas and Propagation, vol. 6, no. 2, pp. 202-207, April 1958, doi: 10.1109/TAP.1958.1144575.

[5] T. Tsuchida, Y. Sugimoto, K. Sakakibara and N. Kikuma, "High Crossover Level Design of a 300 GHz Band Multi-beam Spherical Homogeneous Dielectric Lens Antenna," IEICE Tech. Rep., vol. 123, no. 223, AP2023-93, pp. 27-31, Oct. 2023.

[6] S. Kishi, K. Sakakibara, Y. Sugimoto, T. Morioka, J. Kim and N. Kikuma, "274-GHz Substrate-Integrated-Waveguide Fed Rotman-Lens Multibeam Antenna Integrated in Multi-Layer Substrate," ISAP2023, RS28.4, Nov. 2, 2023.

# XI. Sub-THz band device technologies

Yasunori Suzuki, NTT DOCOMO, INC.
Hiroyuki Takahashi, NTT Device Technology Labs., NTT Corporation
Toshihiro Ohki, Shiro Ozaki, Yusuke Kumazaki, Fujitsu Limited

***Abstract*—This chapter presents sub-THz band device technologies from high power transistors to RF components. The research target of sub-THz band device technologies is identified for sub-THz band mobile communication system in the future. The validity of the presented sub-THz band device technologies confirms the experiment and simulation results.**

## XI-1. Introduction

Mobile communication systems have continuously evolved for offering various services. The fifth generation (5G) mobile communication system has been launched from 2020, while 5G mobile communication system supports millimeter-wave band operation for higher data transmission.

For providing extremely higher data transmission in the future, many research groups focuses on sub-THz band which has enough bandwidth for this purpose. The research target of sub-THz band operation shows the throughout of more than 100 Gbit/s [1]. The transmission distance from base station to terminal needs more than 100 m with corresponding to current service areas. However, the current status is basic research stage. There are many technical issues for exploring sub-THz band operation on mobile communications.

First, RF circuit technologies should be revealed for achieving the research target of sub-THz band operation. RF core technologies are presented for improving quality of data transmission. One is a frequency domain equalizer for providing widely flat frequency response of transmitter. The other is a linearizer for compensating non-linear components generated by power amplifier. This chapter presents the research results of these technologies in detail.

Next, power amplifier technologies are presented. There is the trade-off between frequency and output power / efficiency from the operational principle of transistor. Therefore, it is not sufficient the output power and efficiency of sub-THz band power amplifier in the current status. According to proving various use-case scenarios by sub-THz band mobile communications, it requires higher output power of sub-THz band power amplifier for covering service area. Furthermore, the efficiency of sub-THz band power amplifier such as more than 100 GHz becomes low level, while the power consumption of one seems to become extremely larger level. This chapter shows the high output power and high efficiency techniques for 100 GHz and 300 GHz power amplifiers.

Finally, RF device technologies are presented for high quality of transmission at 300 GHz band. One is the mixer for operating wider bandwidth, which can realize for 100 Gbit/s transmission at 300 GHz band. The other is the front-end IC which can attain the beamforming function at 300 GHz band. This chapter shows the experimental results.

## XI-2. Frequency Domain Equalization Technology

It is well-known that the frequency response of transmitter for providing wider bandwidth transmission is very important role for offering higher quality of transmission. The bandwidth of sub-THz band transmitter will seem to be wider bandwidth than that of cellular-band transmitter. However, the frequency response of actual sub-THz band device is difficult to become widely flat. We proposed the frequency domain equalizer for providing widely flat frequency response [2].

Fig. XI-1(a) and (b) show the measurement configuration and experimental results of the proposed equalizer, respectively. The transmitter shown in Fig. XI-1(a) consists of the arbitrary waveform generator (AWG), up-converter, filter, amplifier, coupler, local oscillator, down-converter, and oscilloscope. The receiver shown in Fig. XI-1(b) is the analyzer. The inverse of frequency response parameter is calculated in the oscillator using the down-converted signal from the output signal of power amplifier, while the proposed equalizer using the parameter is set in the inside of AWG.

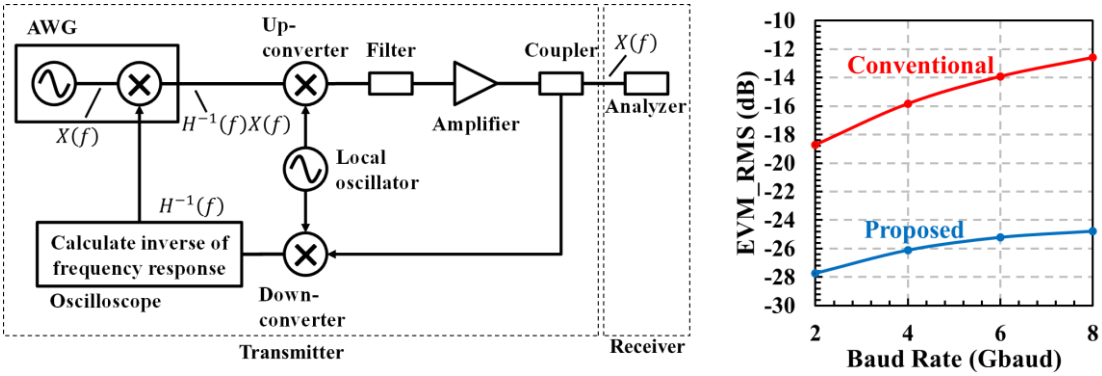


(a) (b)

Fig. XI-1. (a) Measurement configuration and (b) experimental results.
(Roll-off factor: 0.22, Modulation: 64QAM, IF: 8.5 GHz, RF: 155 GHz)

According to Fig. XI-1(b), the proposed equalizer can sufficiently improve the error vector magnitude (EVM) results. The EVM improve about 13 dB at the baud rate of 8 Gbaud. In this case, the data transmission becomes about 48 Gbit/s. From these results, the proposed equalizer is useful for providing sufficient EVM performance.

## XI-3. Non-Linear Components Compensation Technology

In general, non-linear distortion components compensation is very important for improving transmission quality such as bit error rate performance and EVM performance. The millimeter-wave-band base station usually uses digital distortion linearizer for compensating the non-linear distortion components. The sub-THz band base station will seem to employ linearization technology for the same purpose of the millimeter-wave-band base station. In addition, the linearization technology should provide low power consumption for compact-size sub-THz band base stations. From these reasons, we proposed an analogue predistorter operating sub-THz band [3]. Fig. XI-2(a) shows the basic configuration of sub-THz band transmitter, while the proposed predistorter is set in front of power amplifier operating sub-THz band.

Fig. XI-2(b) shows the computer simulation results employing the InP HBT model [4] at 100 GHz. The test signals are two CWs with the same amplitude and difference frequencies at 100.0 GHz and 100.1 GHz. The IM3 means the power of third-order intermodulation distortion components. From Fig. XI-2(b), the proposed predistorter can reduce IM3 component about 10 dB at the same input power per tone. In general, analogue predistorter does not consume power because of using a diode in IC. Therefore, the sub-THz band transmitter does not pay attention to increase power consumption by using the proposed predistorter. There are still technical issues for realizing the proposed predistorter.

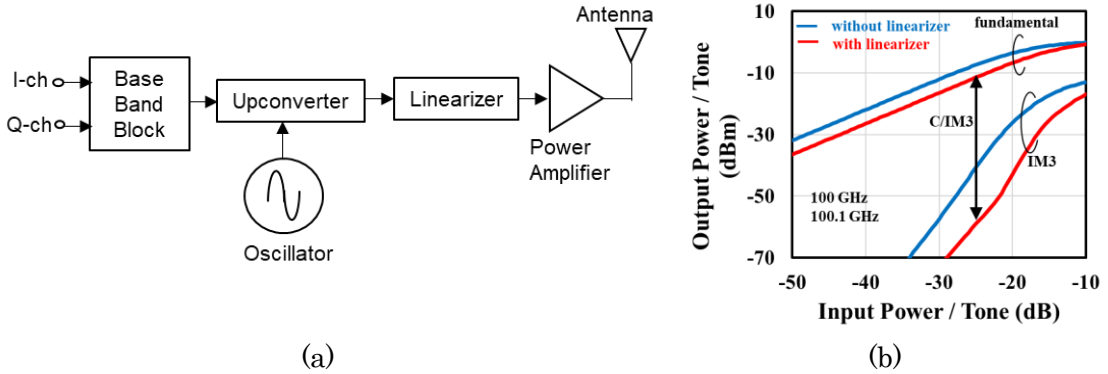


(a) (b)

Fig. XI-2. (a) Basic configuration and (b) simulation results.

## XI-4. Device technology for 100 GHz band power amplifier

GaN-based high-electron-mobility transistors (HEMTs) have advantages in high-power operation because of their high critical electric fields. In addition, a high maximum oscillation frequency enables the amplification of 100 GHz signals. In order to realize further high frequency operation, insertion of AlN spacer layer between barrier and channel layers is effective in improving electron mobility, but can degrade contact resistance, in general.

In this section, we mentioned a low-resistance and low-thermal-budget ohmic contact by introducing periodic microstructures for AlGaN/AlN/GaN HEMTs [5]. An ohmic contact with periodic microstructures was developed through low-damage patterned recess etching and metallization via low-temperature annealing (600˚C) as shown in Fig. XI-3(a). The optimization of structural parameters of periodic microstructures allowed a low contact resistance of 0.29 Ωmm, which is less than half of that of the conventional planar-recessed ohmic contact prepared in same study. A simplified equivalent circuit model reproduced the experimental results and predicted that enhanced metal/channel direct contact areas contributed to the reduction of contact resistance.

Pulsed current–voltage measurements revealed that an AlGaN/AlN/GaN HEMT with periodic microstructures showed considerably suppressed current collapse compared with that of a selective-area growth (SAG) ohmic contact, indicating that the introduction of trap states was suppressed in periodic-structured devices owing to low-thermal-budget processes. Under high off-stress conditions, periodic-structured devices showed the highest drain current at knee voltage compared to the devices with a conventional planar-recessed ohmic contact and an SAG ohmic contact as shown in Fig. XI-3(b). Therefore, ohmic contact with periodic microstructures is one of the best techniques to achieve low contact resistance with low-thermal-budget processes.

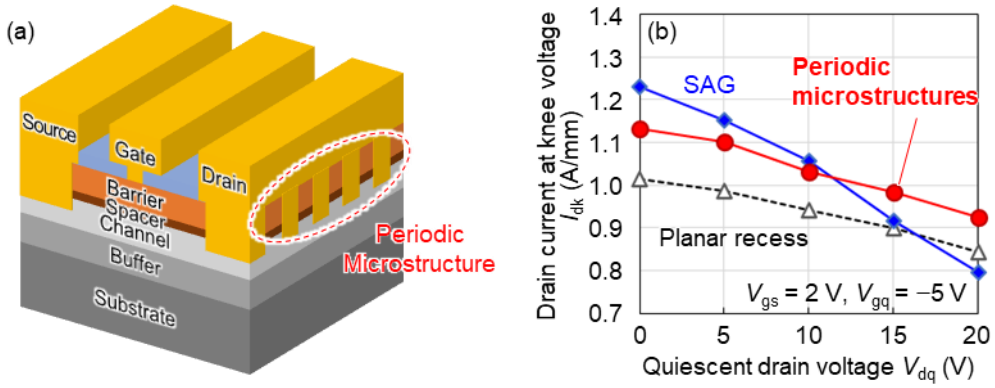


Fig. XI-3. (a) Schematic cross-section of the GaN HEMT with periodic microstructures and (b) correlation between drain current at knee voltage and quiescent drain voltage obtained by pulsed $I_d$-$V_{ds}$ measurement [5]

### XI-5. Device technology for 300 GHz band power amplifier

InP-based HEMTs with InGaAs channel and InAlAs electron supply layers show higher output power characteristics in the 300 GHz band compared with other materials. However, a large gate leakage current and a low breakdown voltage of them limit their operations. To address these issues, metal-oxide-semiconductor (MOS) gate structures with a low gate leakage current are desirable for radiofrequency (RF) operation across a wide bias range. Among the various types of dielectrics used to improve the performance

of oxide-gate HEMTs, $Al_2O_3$ has been one of the most attractive because of its wide band gap (~7.0 eV), high dielectric constant (~9.0), and high breakdown voltage (~10 MV $cm^{-1}$). Furthermore, considering the tradeoff between effective reduction in gate leakage current and degradation of transconductance ($g_m$), it is necessary to optimize the thickness of oxide film. Thus, atomic layer deposited (ALD)- $Al_2O_3$ is suitable for high-frequency insulated-gate HEMTs.

Fig. XI-4(a) shows the schematic illustration of the InP-based MOS HEMTs with ultrathin- $Al_2O_3$ gate dielectrics [6]. After the gate recess process, 2 nm thick $Al_2O_3$ films were deposited on the recess structure using the remote plasma ALD method at 300 °C. Trimethylaluminum (TMA) and $O_2$ plasma were used as precursors, where $O_2$ plasma was used for increasing the density and decreasing the leakage current of ALD- $Al_2O_3$. To minimize the defects in $Al_2O_3$ films, we applied steam annealing at 300°C for 1 h post-deposition. According to previous studies, annealing in an oxygen-containing environment enhances the passivation of dangling bonds, including oxygen vacancies in oxide films. Moreover, it is expected that $H_2O$ vapor (steam) accelerates the hydrolysis of carbon impurities in $Al_2O_3$ films caused by TMA.

Fig. XI-4(b) and (c) show the three-terminal drain and gate current versus gate voltage ($I_d$, $I_g$-$V_{gs}$) and small signal characteristics of InP-based MOS and Schottky-gate HEMTs, respectively. High $f_{max}$ of > 600 GHz and extremely flat $f_{max}$ were successfully achieved across a wide bias range on InP-based HEMTs with a steam-annealed ultrathin- $Al_2O_3$ gate dielectric, due to a reduction in gate leakage current and an increase in forward breakdown voltage.

Furthermore, a broadband high-efficiency six-stage common-source PA MMIC was developed using InP-based MOS HEMTs [7]. A small-signal gain greater than 15 dB was achieved in 242-322 GHz, corresponding to 80 GHz bandwidth as shown in Fig. XI-5(a). The input-output power ($P_{in}$-$P_{out}$) characteristics of the fabricated PA MMIC at 260 GHz are illustrated in Fig. XI-5(b). Although the saturated output power ($P_{sat}$) and peak PAE could not be evaluated due to the output shortage of a signal source, the fabricated PA MMIC demonstrated a high PAE greater than 7.0%, high drain efficiency greater than 7.2%, and high output power greater than 10.6 dBm, corresponding to an output power density of greater than 290 mW/mm at the final stage. To our knowledge, the PA MMIC developed in this work achieved the highest PAE among all the J-band solid-state PAs.

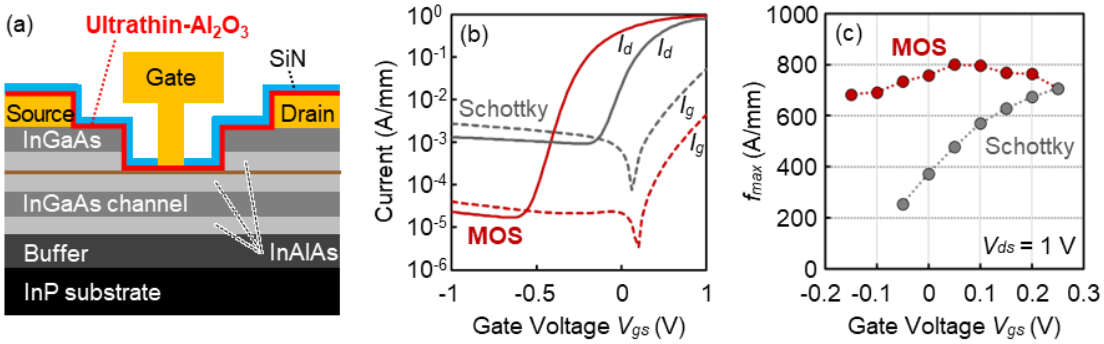


Fig. XI-4. (a) Schematic cross-section, (b) $I_d$-$V_{gs}$ characteristics and (c) $f_{max}$ calculated from S-parameters of the InP-based MOS-HEMT compared with Schottky gate HEMT (Reproduced from ref. 6, copyright 2017 by the Japan Society of Applied Physics).

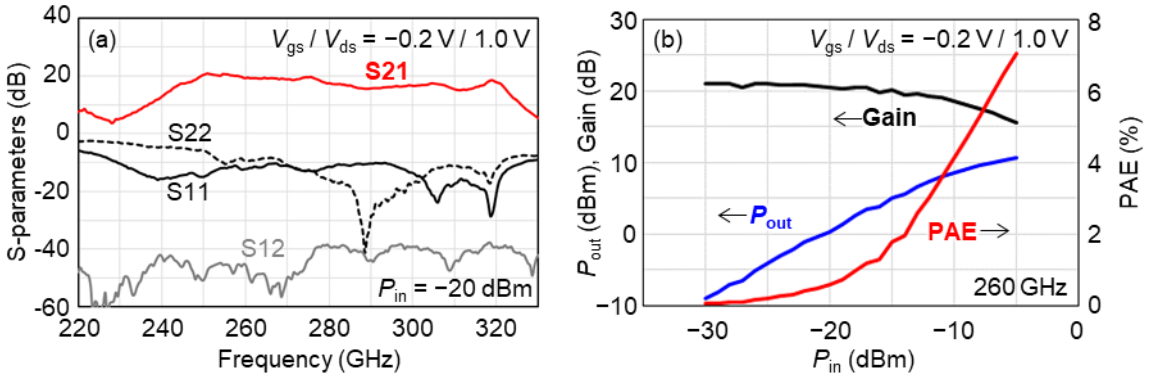


Fig. XI-5. (a) S-parameters and (b) power characteristics of PA MMIC with InP-based MOS HEMTs [7]

### XI-6. Challenge of utilizing over 100 Gbit/s per channel

Standardization of the 300-GHz band with a channel bandwidth of over 25 GHz has been discussed in IEEE 802.15.3d [8]. The use of such a broad channel bandwidth is promising for high-speed wireless systems with data capacities of over 100 Gbit/s per channel. Given these requirements, an extremely wide operating frequency band is needed for radio-frequency devices in the 300-GHz band. Subsequently, over 100-Gbit/s transmission using multiple channels has been reported [9]. The 300-GHz-band fundamental mixer IC shown in Fig. XI-6(a) has an operating band of 100 GHz ranging from 220 to 320 GHz. In addition, back-to-back data transmission using the WR3.4 waveguide mixer module shown in Fig. XI-6(b) was performed in three different frequency bands. The maximum data rates of the 1st band (center frequency (fc) of 227 GHz), 2nd band (fc of 257 GHz), and 3rd band (fc of 307 GHz) are 120 Gbit/s (20 GBaud 64QAM), 168 Gbit/s (42 GBaud 16QAM), and 152 Gbit/s (38 GBaud 16QAM),

respectively. In addition, dual-channel back-to-back data transmission shown in Fig. XI-6(c) was also demonstrated using two mixer modules for a transmitter and a receiver. The maximum data rate of the high band (fc of 316.5 GHz) and the low band (fc of 261 GHz) are 112 Gbit/s (28 GBaud 16QAM) and 128 Gbit/s (32 GBaud 16QAM), respectively. The total data rate of a simultaneous signal transmission was 240 Gbit/s.

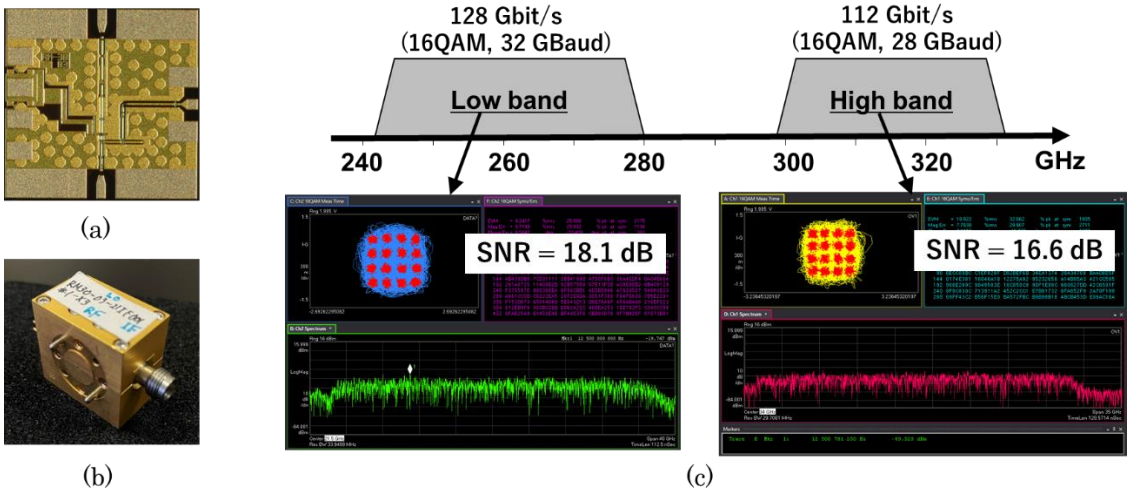


Fig. XI-6. (a) Photograph of mixer IC and (b) mixer module. (c) Measured constellation and spectra of dual-channel back-to-back data transmission experiment [9].

### XI-7. Beamforming in 300-GHz Band

The advantage of the 300-GHz band is that it enables the use of a wide frequency range. However, large free-space path loss occurs during signal propagation through space. Beamforming technology using a phased-array configuration is an effective solution to extend signal coverage. High-density packaging technology is required for the 300-GHz band because the chip dimensions (1–1.5 mm) are larger than the half-wavelength required for beamforming. An example of a successful implementation is a 4-element 300-GHz-band phased-array utilizing a unique flip-chip-on-chip technique that combines both Si-based and InP-based ICs [10]. The proposed 4-element phased-array transmitter consists of four CMOS chips, four InP HBT chips, and a PCB substrate (Fig. XI-7(a)). The CMOS chips were fabricated in a 65-nm CMOS process and include the IF amplification, LO chain, and mixer. The power amplifier chips were fabricated in an InP HBT process. The RF frontend on the fabricated module is small. The phased-array transmitter achieves a maximum EIRP of 8.4 dBm and has a –6 dB beam coverage of 36°, as well as a maximum data rate of 30 Gbit/s over a 50-cm link distance as shown in Fig. XI-7(b).

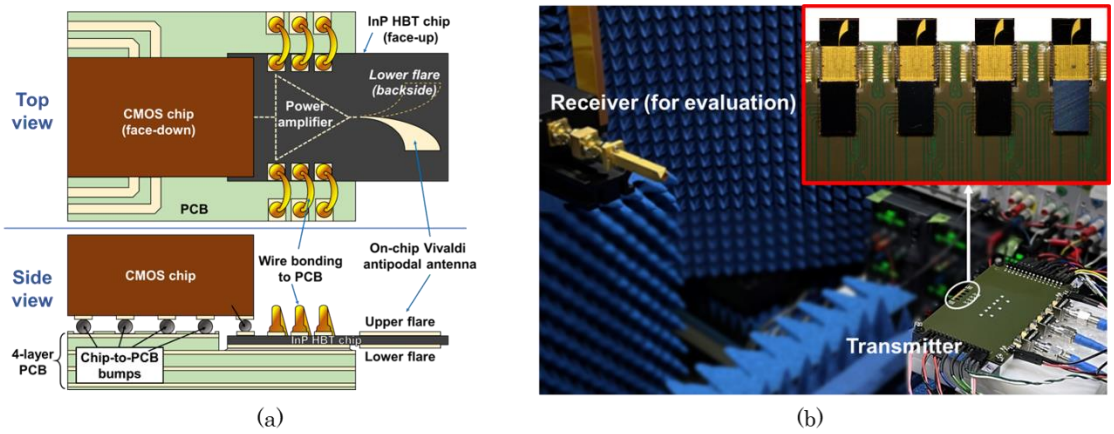


Fig. XI-7. (a) Proposed implementation technique and (b) photograph of measurement system for EIRP, beam pattern and data transmission [10].

## XI-8. Conclusion

This chapter presented the research activities for sub-THz band device technologies from high power transistors to RF components. These research activities focus on the research target for sub-THz band mobile communications, which identifies to achieve the throughput of 100 Gbit/s and the distance from base station to terminal of 100 m.

The research results show excellent performance of each research activity at sub-THz band. However, the research activities are basic stage for evaluating various performance. There are some technical issues for realizing the devices for operating at sub-THz band. In the future, sub-THz band mobile communications will be provided by the research and development results from the research activities.

## XI-9. Acknowledgements

This chapter includes a part of results of "R&D for Expansion of Radio Wave Resources (JPJ000254)," commissioned by The Ministry of Internal Affairs and Communications, Japan.

## REFERENCE

[1] NTT DOCOMO, "White Paper 5G Evolution and 6G", https://www.docomo.ne.jp/english/corporate/technology/whitepaper_6g/

[2] Hiroto Yamamoto, Atsushi Fukuda, Sumire Aoki, Hiroshi Hamada, Hiroshi Okazaki, and Yasunori Suzuki, "A Wideband Single Carrier Transmitter Configuration Equalizing Non-flat Frequency Response," in The 27th Asia-Pacific Conference on Communications (APCC 2022), Oct. 2022.

[3] Sumire Aoki, Hiroshi Hamada, Hiroto Yamamoto, Atsushi Fukuda, Teruo Jyo, Hiroyuki Takahashi, Hiroshi Okazaki, and Yasunori Suzuki, "A Design of InP-HBT

100-GHz Diode Linearizer Toward 6G," in The 27th Asia-Pacific Conference on Communications (APCC 2022), Oct. 2022.

[4] N. Kashio et al., "Over 450-GHz ft and fmax InP/InGaAs DHBTs With a Passivation Ledge Fabricated by Utilizing SiN/SiO2 Sidewall Spacers," IEEE Transactions on Electron Devices, vol. 61, no. 10, pp. 3423–3428, Oct 2014.

[5] Yusuke Kumazaki, Shiro Ozaki, Naoya Okamoto, Naoki Hara, and Toshihiro Ohki, "Low-Resistance and Low-Thermal-Budget Ohmic Contact by Introducing Periodic Microstructures for AlGaN/AlN/GaN HEMTs," IEEE Transactions on Electron Devices, vol. 69, no. 6, pp. 3073 – 3078, Jun. 2022, doi: 10.1109/TED.2022.3169728

[6] Shiro Ozaki, Yusuke Kumazaki, Naoya Okamoto, Naoki Hara, and Toshihiro Ohki, "Improved $f_T/f_{max}$ in wide bias range by steam-annealed ultrathin-$Al_2O_3$ gate dielectrics for InP-based high-electron-mobility transistors," Applied Physics Express, vol. 15, p. 041001, doi: 10.35848/1882-0786/ac5a17

[7] Yusuke Kumazaki, Shiro Ozaki, Naoya Okamoto, Naoki Hara, Yasuhiro Nakasha, Masaru Sato, and Toshihiro Ohki, "High-Efficiency 250-320 GHz Power Amplifiers Using InP-Based Metal-Oxide-Semiconductor High-Electron-Mobility Transistors," IEICE Transactions on Electronics, vol. E106-C, no. 11, pp. 661 – 668, Nov. 2023, doi: 10.1587/transele.2023MMP0005

[8] V. Petrov, T. Kürner, and I. Hosako, "IEEE802.15.3d: First Standardization Efforts for Sub-Terahertz Band Communications toward 6G," IEEE Communications Magazine Nov. 2020, pp. 28-33.

[9] T. Jyo, H. Hamada, T. Tsutsumi, I. Abdo, S. Kawahara, D. Kitayama, M. Nagatani, and H. Takahashi, "220-to-320-GHz Fundamental Mixer in 60-nm InP HEMT Technology Achieving 240-Gbps Dual-Band Data Transmission," IEEE Transactions on Microwave Theory and Techniques, early access, Nov. 3, 2023, doi: 10.1109/TMTT.2023.3327478.

[10] I. Abdo, T. Jyo, A. Pander, H. Wakita, Y. Shiratori, M. Muto, H. Hamada, M. Nagatani, C. da Gomez, C. Wang, K. Hatano, C. Liu, A. A. Fadila, J. Pang, A. Shirane, K. Okada, and H. Takahashi, "300-GHz-Band Four-Element CMOS-InP Hybrid Phased-Array Transmitter With 36circ Steering Range," IEEE Microwave and Wireless Technology Letters, Vol. 33, Issue 6, Jun. 2023, pp. 887 - 890

# XII. 6G Simulator using Real Environment Model based on Point Cloud Data

Koshiro Kitao, Satoshi Suyama, Takahiro Tomie, Nobuaki Kuno,
Kiichi Tateishi, Huiling Jiang
NTT DOCOMO, INC.

*Abstract*— When studying the deployment of a 5G or 6G system in a specific environment such as an indoor environment or factory, it is important to evaluate system performance beforehand such as throughput in the target environment. In addition, the ability to visualize system performance can provide very useful information in deciding on a method for deploying the communications system. We have developed a 6G system level simulator (6G simulator) to clarify the feasibility of 100 Gbps ultrafast communications by utilizing the sub-terahertz band as a system, however, existing 6G simulators can evaluate throughput when using the 100 GHz band in prepared scenarios such as shopping malls, but not in specific real environments such as indoors or factories . With the aim of evaluating system performance in real environments, we have developed an enhanced simulator that can evaluate and visualize 5G and 6G throughput based on propagation characteristics obtained by ray tracing calculations that employ a real-environment model based on point cloud data. In this white paper, we describe an overview of the functions of this simulator and an example of performance evaluation.

## XII-1. Introduction

When studying the deployment of a 5G or 6G system in a specific environment such as an indoor environment or factory, it is important to evaluate system performance beforehand such as throughput in the target environment. In addition, the ability to visualize system performance can provide very useful information in deciding on a method for deploying the communications system. We have developed a 6G system level simulator (6G simulator) to clarify the feasibility of 100 Gbps ultrafast communications by utilizing the sub-terahertz band as a system, however, existing 6G simulators can evaluate throughput when using the 100 GHz band in prepared scenarios such as shopping malls, but not in specific real environments such as indoors or factories [1].

Estimating throughput with high accuracy requires accurate estimation of the radio propagation characteristics in the environment where the communications system is to be deployed. A technique for estimating propagation characteristics with high accuracy that has been attracting attention in recent years is to use point cloud data obtained from the evaluation environment to create a polygon model of structures and to use that model for ray tracing calculations [2]-[5]. With the aim of evaluating system performance in real environments, we have developed an enhanced simulator that can evaluate and

visualize 5G and 6G throughput based on propagation characteristics obtained by ray tracing calculations that employ a real-environment model based on point cloud data [6]. In this white paper, we describe an overview of the functions of this simulator and an example of performance evaluation.

## XII-2. Overview of 6G Simulator Based on a Real Environment Model Using Point Cloud

We have developed a "6G simulator based on a real environment model" with the aim of evaluating throughput in a real environment. This simulator can evaluate and visualize throughput in 5G and 6G based on propagation characteristics obtained by ray tracing calculations using point cloud data. Though based on the 6G simulator reported in [1], this simulator uses information on the propagation characteristics obtained by ray tracing calculations as a channel model between BSs and MSs used in system-level simulations. Specifically, the information used by this simulator consists of the propagation loss, angle of arrival of arriving waves, and propagation delay calculated by ray tracing.

The evaluation environment used in this simulation is shown in Fig. XII-1. This simulator can display an image of any environment targeted for evaluation using the point cloud data obtained for that environment. The figure shows the image generated using the point cloud data obtained in a conference room. This image also reproduces the actual conference room in color by using camera-based image data obtained at the same time as point cloud data. The simulator can place BSs and MSs at any positions, and here, the figure shows an evaluation environment for two BSs and six MSs. When multiple BSs are deployed in the simulation, the throughput of an MS at any position can be evaluated by inputting into a tool the ray-tracing calculation results when MSs are deployed within the evaluation area for each BS. However, MS movement is not supported here.

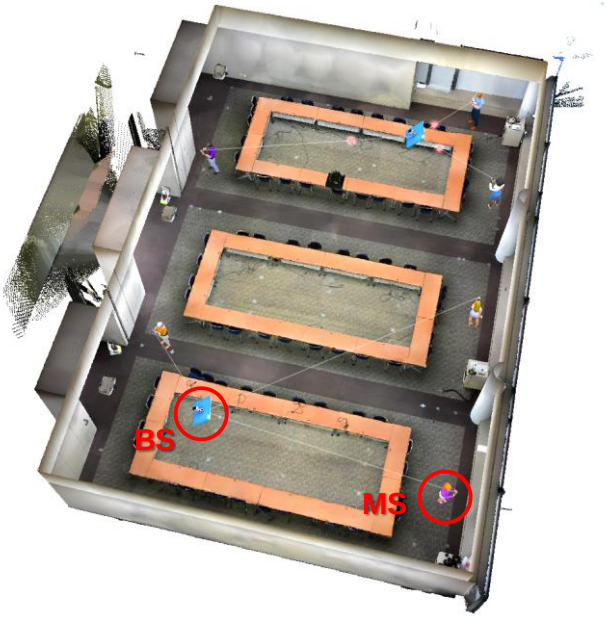


Fig. XII-1. 6G simulator evaluation environment using point cloud data

This simulator can also display color maps for several propagation parameters so that the relationship between propagation characteristics and throughput characteristics can be visually grasped. Ray tracing calculation specifications are listed in Table XII-1. In these calculations, the polygon data generated by point cloud data for the conference room shown in Fig. XII-1 is input into Wireless Insight, a commercially available ray tracing tool. The center frequencies used here are 4.7, 28, and 100 GHz assuming 5G and 6G. The type of antenna used by both BSs and MSs is an onmi-directional antenna, BS and MS antenna heights are 2.0 m and 1.5 m, respectively, and the condition for ray searching is 7 reflections. The calculations are performed assuming that the material of wall surfaces is concrete.

Table XII-1. Ray tracing specifications

| 項目 | 諸元 |
|---|---|
| Ray tracing tool | Wireless Insight |
| Center frequency | 4.7 GHz, 28 GHz, 100 GHz |
| BS and MS antenna height | 1.5 m |
| BS and MS antennas | Omni-directional antenna (0 dBi) |
| Ray launching interval | 0.25 ° |
| Number of reflections | 7 |
| Material | Concrete |

### XII-3. Simulation Results

Examples of propagation characteristics calculated by ray tracing are shown in Fig. XII-2. This figure consists of color maps showing the received level at 100 GHz and the angle spread on the MS side in the horizontal plane. From these maps, it can be seen that the received level is high near each BS and that the angle spread becomes larger near the walls of the conference room due to the effects of reflection.

Next, we describe throughput characteristics calculated by this simulator based on the propagation parameters calculated by ray tracing as described above. The specifications for system-level simulation of this simulator are listed in Table XII-2. The simulator generates a fading channel based on each ray's propagation loss, propagation delay, and arriving angle calculated by ray tracing and calculates throughput when performing BF by massive MIMO and MIMO spatial multiplexing. Here, user throughput on the DL at 100 GHz is shown in Fig. XII-3. The figure shows user throughput for MS #0–5 circled in red. It can be seen that MS #3 and MS #4 located in the areas of Fig. XII-2 having a high received level and large angle spread can achieve high throughput.

In a similar manner, this simulator could also display user throughput on the DL at 4.7 and 28 GHz. The throughput average of six MSs at 4.7, 28, and 100 GHz was found to be 0.62, 1.9, and 37 Gbps, respectively. These results confirm that throughput can be improved by using high frequency bands to provide a wider bandwidth.

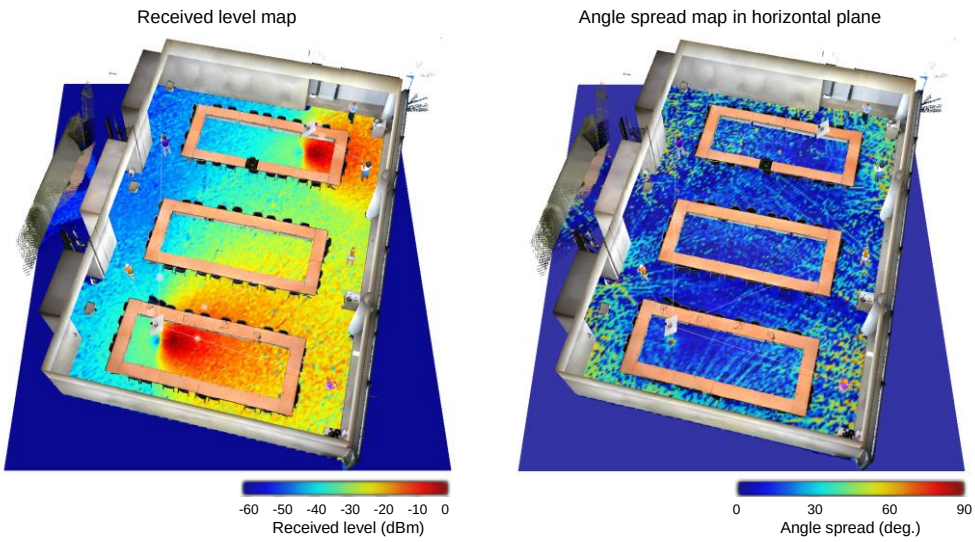


Fig. XII-2. Received level map at 100 GHz and angle spread map on MS side in horizontal plane

Table XII-2. Transmission simulation specifications

| Center frequency | 4.7 GHz | 28 GHz | 100 GHz |
|---|---|---|---|
| Bandwidth | 100 MHz | 400 MHz | 8.0 GHz |
| Total transmission power in TRP | 30 dBm | | |
| MS transmission power | 23 dBm | | |
| Number of antenna elements in TRP (vertical × horizontal × sub-arrays) | 144 (4 x 4 x 9) | 2304 (16 x 16 x 9) | 9216 (32 x 32 x 9) |
| Number of antenna elements in MS (vertical × horizontal × sub-arrays) | 144 (4 x 4 x 9) | | |
| Number of TRPs | 2 | | |
| Number of MS | 6 | | |
| Number of MIMO layers | 1, 2, 3, 4, 8 | | |

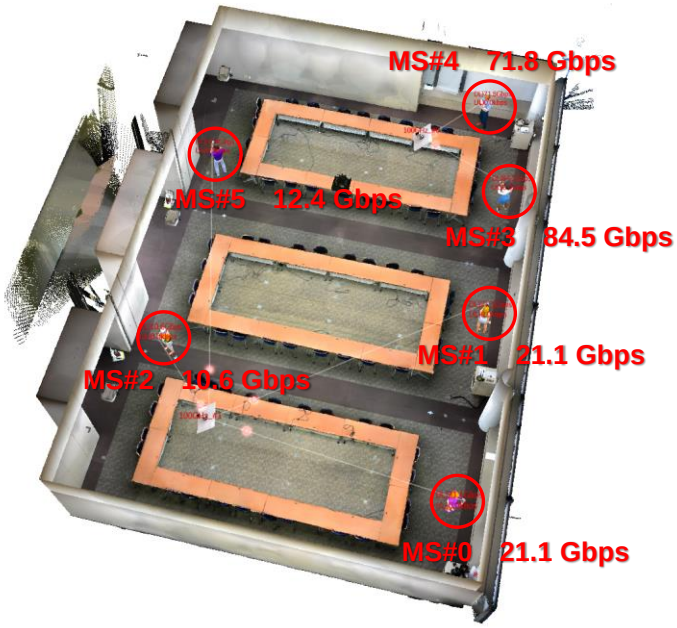


Fig. XII-3. User throughput on DL at 100 GHz

## XII-4. Conclusion

We describe an overview of the functions of 6G simulator based on point cloud data and an example of performance evaluation. Going forward, we plan to compare throughput measured using experimental equipment in a real environment with the calculation results of this simulator to evaluate simulator performance and improve it accuracy. Additionally, with an eye to developing tools that can dynamically control and optimize 6G through CPS, we plan to conduct technical studies on raising the accuracy

and speed of propagation simulations using real environment models and transmission simulations at the link and system levels.

## REFERENCE


[1] T. Okuyama et al.: "6G System-level Simulator—Toward 100 GHz Band, 100 Gbps Extreme-high-data-rate Communications—," NTT DOCOMO Technical Journal, Vol. 23, No. 3, pp. 13–26, Jan. 2022.

[2] J. Jarvelainen, K. Haneda, and A. Karttunen: "Indoor Propagation Channel Simulations at 60 GHz Using Point Cloud Data," IEEE Transactions on Antennas and Propagation, Vol. 64, No. 10, pp. 4457–4467, Oct. 2016.

[3] P. Koivumaki, G. Steinbock, and K. Haneda: "Impacts of Point Cloud Modeling on the Accuracy of Ray-Based Multipath Propagation Simulations," IEEE Transactions on Antennas and Propagation, Vol. 69, No. 8, pp. 4737–4747, Aug. 2021.

[4] W. Okamura, R. Lukita, G. Ching, Y. Matsuyama, Y. Kishiki, Z. Chen, K. Saito, and J. Takada: "Simplification method of 3D point cloud data for ray trace simulation in indoor environment," IEICE Communications Express, Vol. 9, No. 6, pp. 182–187, Jun. 2020.

[5] K. Kitao, M. Nakamura, T. Tomie, and S. Suyama: "Study of Raytracing using Point Cloud Data for Indoor Area Evaluation," ICETC 2022, S1-6, Nov. 2022.

[6] K. Tateishi et al.: "Enhancement of 6G System-level Simulators," NTT DOCOMO Technical Journal, Vol. 25, No. 2, Oct. 2023.

# XIII. THz Sensing and Communication Towards Future Intelligence Connected Networks

Liu Qiao, Huawei Technologies
Koshimizu Takashi, Huawei Technologies Japan

## XIII-1. Introduction

It is envisioned that B5G and 6G would have intelligent connection of everything [1]. Specifically, the demanding ISAC feature would be a novel key service besides the exploration of the THz band. We have key technology research and prototype verification, which shows 210 Gbit/s data transmission rate at 330 m distance, and up to 3 mm invisible imaging, which is the highest performance in ISAC field.

## XIII-2. THz Spectrum and Application Scenarios

A number of bands have been recently approved for ultra-high data rate transmission, which motivates research on THz spectrum and application scenarios.

## XIII-3. THz Channel Propagation and Modeling

A hybrid channel modeling methodology is proposed. A few suggested methods are list in Table XIII-1

.

Table XIII-1. Terahertz channel modeling methodology

| Application | Channel Modeling Method |
|---|---|
| Communication | **Stochastic** |
| Positioning | **Stochastic (GBSCM)** |
| Localization and mapping | **Ray-based** |
| Imaging and recognition | **EM-based** |

### XIII-3.1. Channel Measurement System and Measurement Campaign

The measurements are achieved at 140, 220, and 280 GHz. Parameters are listed in Table XIII-2.

Table XIII-2. Parameters of the measurement system

| Parameter | Value | |
|---|---|---|
| Frequency band [GHz] | 140 | 220 |
| Local oscillator [GHz] | 10.667 | 18 |
| Start frequency [GHz] | 130 | 201 |
| End frequency [GHz] | 143 | 209 |
| Bandwidth [GHz] | 13 | 8 |
| Sweeping points | 1301 | 801 |
| Transmitter antenna gain [dBi] | 15 | 10 |
| Receiver antenna gain [dBi] | 25 | 25 |

| | | |
|---|---|---|
| Azimuth rotation range [degree] | [0:10:360] | [0:10:360] |
| Elevation rotation range [degree] | [–20:10:20] | [–20:10:20] |
| Delay resolution [ps] | 76.9 | 125 |
| Maximum excess delay [ns] | 100 | 100 |

### XIII-3.2. THz Channel Characterization and Analysis

The multi-frequency alpha-beta-gamma (ABG) path loss results on 140, 220, and 280 GHz bands are depicted in Fig. XIII-1. The proposed ABG path loss model is as follows:

$$PL^{ABG}[dB] = 20.7log_{10}\left(\frac{d}{d_0}\right) + 26.72 + 22.2log_{10}\left(\frac{f}{f_0}\right) + 2.53 \quad (2)$$

More measurement campaign and modeling results can be referred to that in the literature [2–3].

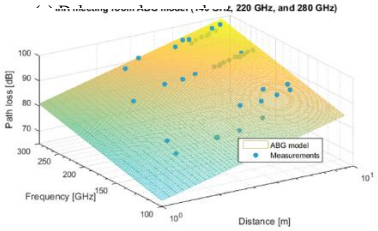


Fig. XIII-1. ABG path loss model results at the meeting room

On the small-scale aspect, the THz channel also exhibits different propagation. For further study, we choose one receiver position, as shown in Fig. XIII-2 to analyze the spatial angle of arrival (AoA).

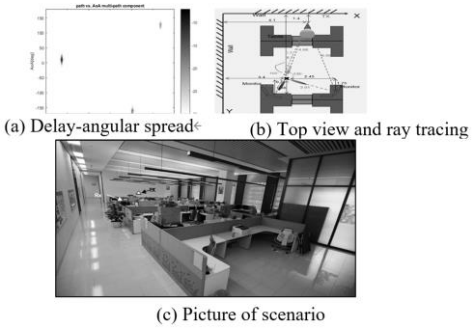


Fig. XIII-2. Indoor hotspot cell (InH) meeting room 140 GHz measurement scenario

## XIII-4. THz Hardware and Components

### XIII-4.1. THz Components

Fig. XIII-3 demonstrates a GaN HEMT power amplifier and its package operation at 220 GHz. The saturation output power reaches 18 dBm. The best amplification application for CMOS is at 140 GHz, and the gain can be achieved at 200 to 300 GHz

using positive feedback technology [6]. BiCMOS currently operates at a maximum amplification frequency of 310 GHz, achieving 4 dBm of output power [5].

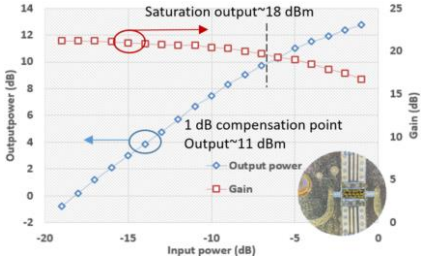


Fig. XIII-3. Output performance of 220 GHz GaN HEMT power amplifier

THz receivers can be classified as heterodyne and direct detector receivers. The different technologies available to build THz and sub-THz receivers are shown in Fig. XIII-4.

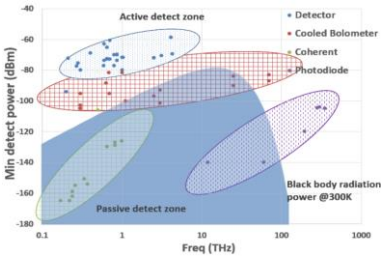


Fig. XIII-4. THz receivers with respect to source technology, with 1 Hz resolution bandwidth (RBW)

### XIII-4.2. THz Antenna

In a THz "tile-able" array, large number of antennas are integrated on chip. High-level integration and scalability are two important considerations in tile design. Programmability is another desired feature of THz "tile-able" array. Limited configurability has been demonstrated mainly through electrically, mechanically or thermally controlled reconfigurable materials [8–9]. In addition, CMOS integration is an important consideration to allow for low-cost fabrication.

### XIII-4.3. Intelligent Surface

In [10], intelligent surface is classified into passive surface and active surface. Fig. XIII-5 shows a wireless communication environment enabled by intelligent surfaces.

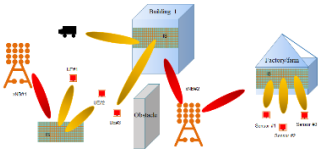

(a) Outdoor environment

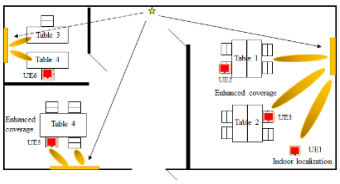


(b) Indoor environment

Fig. XIII-5. Typical RIS use cases for THz

### XIII-4.4. Integration Technologies

Multichip module (MCM), system-in-package (SiP), and heterogeneous integration are promising candidates. Antenna and silicon lenses are integrated in the package to reduce connection loss and enhance EIRP [11]. The through-silicon via (TSV) process has better integration and process precision and can be used at higher frequencies [12]. The embedded wafer level ball grid array (eWLB) technology usually used at low frequency can also be used in lower end of THz [13] as SiP technology. Wafer-level integration using Benzo cyclobutene (BCB) provides a 2D integration method [14]. The alternative approach bonds the wafer or die of III-V materials onto a patterned silicon wafer [15].

## XIII-5. THz System and Testing

### XIII-5.1. THz Communication System

Our THz communication platform at 220 GHz frequency, in which multiple advanced technologies are realized. Field trial experiment was conducted as shown in Fig. XIII-6 [16].

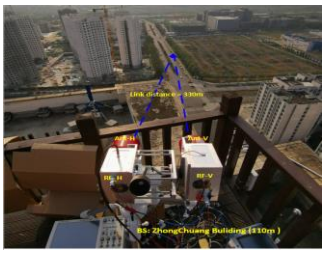

Fig. XIII-6. THz field trial, 2 x 2 polarization-MIMO system

Maximum throughput is 210 Gbit/s, and net data rate is 168 Gbit/s. The demodulated constellation is shown in Fig. XIII-7.

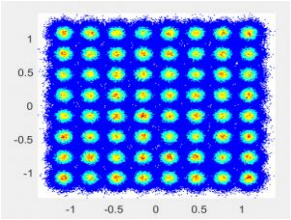


Fig. XIII-7. 64QAM demodulated constellation

Long distance field trial for single-input single-output (SISO) is also considered in our verification. As shown in Fig. XIII-8, the link distance is 3.6 km with high-humidity weather.

Fig. XIII-8. 3.6 km long distance test

Maximum throughput is 35 Gbit/s, and net data rate is 28 Gbit/s after removal of the FEC overhead.

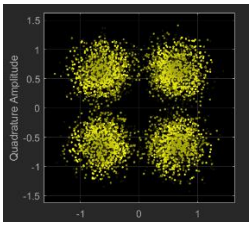


Fig. XIII-9. 3.6 km, demodulation constellation

To explore THz-ISAC, we use a similar system architecture and device. By using the concept of virtual MIMO and compression sensing algorithms, the EM imaging of metal objects hidden in a paper box is rebuilt successfully, and mm-level imaging resolution is achieved, as presented in Fig. XIII-10.

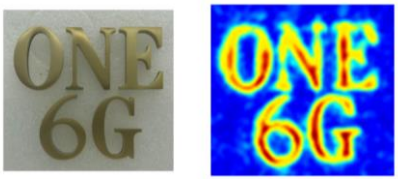


Fig. XIII-10. Imaging results of non-sparse full aperture scanning

### XIII-5.2. THz Sensing System

We developed both simulation model and measurement setup for THz-TDS material characterization application. As shown in Fig. XIII-11, both permittivity and loss tangent agree well with the theoretical values. [17] showed a quasi-optical system that performs complex material property measurement. The complex permittivity of various Rogers RT/duroid series PCB substrates agreed well with the literature.

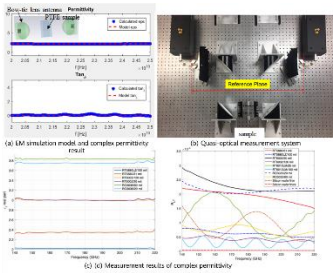

Fig. XIII-11. Simulated and measurement results of material characterization application; Measurement from [60].

In addition, a qualitative microwave holography (QMH) imaging method was demonstrated to perform the imaging and material mapping application [18–19]. The image test-bed was then set up as shown in Fig. XIII-12. It is shown that QMH can achieve spatial resolution close to λ/4, even under a far field measurement set up. A comparison can be found in [19–20].

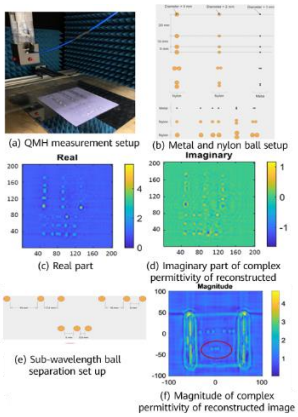


Fig. XIII-12. QMH reconstruction of metal and nylon balls of various sizes. Results from [20]

## XIII-6. Conclusion

In this paper, we discussed the advantages and typical scenarios of THz communication and sensing applications. We also proposed a hybrid channel modeling framework to improve the modeling accuracy and efficiency. In particular, the THz subsystem with silicon and III-V compound semiconductor materials heterogeneous integration is analyzed and proposed to improve the performance by using the advantage of different processes and materials. Finally, the prototype and measurement campaigns were conducted to illustrate the advantages for high throughput communication and high-resolution sensing scenarios. A variety of measurement campaign examples show 210 Gbit/s data transmission rate at 330 m distance, and up to 3 mm invisible imaging, which is the highest performance in this field.

## References


[1] W. Tong and P. Zhu, "6G: the next horizon, from connected people and things to connected intelligence," Cambridge University Press, 2021.

[2] He J, Chen Y, Wang Y, et al., "Channel measurement and path-loss characterization for low-terahertz indoor scenarios," arXiv preprint arXiv:2104.00347, 2021.

[3] Y. Chen, C. Han, Z. Yu, and G. Wang, "140 GHz channel measurement and characterization in an office room," ICC 2021 - IEEE International Conference on Communications, 2021, pp. 1-6, doi: 10.1109/ICC42927.2021.9500596.

[4] Y. Chen, Y. Li, C. Han, Z. Yu, and G. Wang, "Channel measurement and ray-tracing-statistical hybrid modeling for low-terahertz indoor communications," arXiv:2101.12436

[5] U. R. Pfeiffer, R. Jain, J. Grzyb, S. Malz, P. Hillger, and P. Rodríguez-Vízquez, "Current status of terahertz integrated circuits - from components to systems," 2018 IEEE BiCMOS and Compound Semiconductor Integrated Circuits and Technology Symposium (BCICTS), 2018, pp. 1-7, doi: 10.1109/BCICTS.2018.8551068.

[6] X. Li et al., "A 250-310 GHz power amplifier with 15-dB peak gain in 130-nm SiGe BiCMOS process for terahertz wireless system," in IEEE Transactions on Terahertz Science and Technology, doi: 10.1109/TTHZ.2021.3099057.

[7] D. Parveg, D. Karaca, M. Varonen, A. Vahdati, and K. A. I. Halonen, "Demonstration of a 0.325-THz CMOS amplifier," 2016 Global Symposium on Millimeter Waves (GSMM) & ESA Workshop on Millimetre-Wave Technology and Applications, 2016, pp. 1-3.

[8] Liu, C., Ye, J., and Zhang, Y., "Thermally tunable THz filter made of semiconductors," Opt. Comm. 283, 865–868 (2010).

[9] Sanphuang, V., Ghalichechian, N., Nahar, N. K., and Volakis, J. L., "Reconfigurable THz filters using phase-change material and integrated heater," IEEE Trans. THz. Sci. Technol. 6, 583–591 (2016).

[10] C. Huang et al., "Holographic MIMO surfaces for 6G wireless networks: opportunities, challenges, and trends," in IEEE Wireless Communications, vol. 27, no. 5, pp. 118-125, October 2020, doi: 10.1109/MWC.001.1900534.

[11] T. Tajima, H. Song, and M. Yaita, "Compact THz LTCC receiver module for 300 GHz wireless communications," in IEEE Microwave and Wireless Components Letters, vol. 26, no. 4, pp. 291-293, April 2016, doi: 10.1109/LMWC.2016.2537044.

[12] S. Hu et al., "TSV technology for millimeter-wave and terahertz design and applications," in IEEE Transactions on Components, Packaging and Manufacturing Technology, vol. 1, no. 2, pp. 260-267, Feb. 2011, doi: 10.1109/TCPMT.2010.2099731.

[13] A. Hassona et al., "Demonstration of +100-GHz interconnects in eWLB packaging technology," IEEE Trans. Compon., Packag., Manuf. Technol.,vol. 9, no. 7, pp. 1406–1414, Jul. 2019.

[14] X. Yang et al., "Low-loss heterogeneous integrations with high output power radar applications at W-band," in IEEE Journal of Solid-State Circuits, doi: 10.1109/JSSC.2021.3106444.

[15] M. Urteaga et al., "THz bandwidth InP HBT technologies and heterogeneous integration with Si CMOS," 2016 IEEE Bipolar/BiCMOS Circuits and Technology Meeting (BCTM), 2016, pp. 35-41, doi: 10.1109/BCTM.2016.7738973.

[16] Peiying Zhu, "6GWFF 2021 - 6G: connected intelligence (keynote 1)," https://www.youtube.com/watch?v=PU0wKfwssk0.

[17] H. -T. Zhu and K. Wu, "Complex permittivity measurement of dielectric substrate in sub-THz range," in IEEE Transactions on Terahertz Science and Technology, vol. 11, no. 1, pp. 2-15, Jan. 2021, doi: 10.1109/TTHZ.2020.3036181.

[18] Daniel Tajik, Aaron D. Pitcher, and Natalia K. Nikolova, "Comparative study of the Rytov and Born approximations in quantitative microwave holography," Progress In Electromagnetics Research B, Vol. 79, 1-19, 2017.

[19] D. Tajik and N.K. Nikolova, "Real-time imaging with simultaneous use of Born and Rytov approximations in quantitative microwave holography," IEEE Trans. Microwave Theory Tech. (submitted Aug. 9, 2021)

[20] D. Tajik, R. Kazemivala, and N.K. Nikolova, "Combining the Born and Rytov approximations in quantitative microwave holography," The IEEE 19th Int. Symp. on Antenna Technology and Applied Electromagnetics (ANTEM 2021), Winnipeg, Canada, Aug. 8-11, 2021.

## XIV. 300GHz point-to-point fixed wireless transmission systems

Tetsuya Kawanishi, Waseda University
Riku Yoshino, Waseda University
Arata Ogaki, Waseda University
Kunihisa Jitsuno, Waseda University

*Abstract*—**In future mobile networks, many small cells will be needed to provide broadband service everywhere. In order to efficiently connect many base stations, mobile backhaul and fronthaul should be constructed by various types of transmission media, including short-range fixed radio transmission in the THz band. This paper describes a 300 GHz fixed radio transmission system based on V-band IF signal processing. IEEE802.15.3e compliant 60 GHz transceivers are used as baseband and IF units. To expand the flexibility of the network configuration, THz fixed radio can use non-line-of-sight propagation due to reflection as in conventional microwave systems. However, the effect of reflector roughness must be considered. This paper also discusses recent research results on reflection loss and scattering due to roughness.**

### XIV-1. Introduction

Many small cells would be required to provide broadband services anywhere in future mobile networks. To connect many base stations effectively, mobile backhaul and fronthaul should be constructed by various types of transmission media including THz short distance fixed wireless transmission. Optical fiber links are commonly used for mobile backhaul and fronthaul in north-east Asia, while fixed wireless links are often used in developing countries [1]. To mitigate huge traffic demand in mobile networks, conventional fixed wireless links using microwave bands would be replaced by optical fibers. However, it would be rather difficult to make all the base stations connected only by optical fibers, because the number of the base stations would be huge. A part of mobile backhaul or fronthaul links would be by fixed wireless connections, where fiber installation cost is high [2]. The fixed wireless and optical transmission offer heterogeneous networks where high-speed optical fiber links are bridged by high-speed fixed wireless links. The required transmission capacity is much higher than that of conventional fixed wireless transmission using microwave. On the other hand, the required transmission distance is much shorter than a few hundred meters. Such fixed wireless links should be based on millimeter-wave or THz radio, where large bandwidths are available for fixed wireless transmission and attenuation in the air is relatively large.

Normally, fixed wireless links are based on line-of-sight (LoS) propagation, however, non-line-of-sight (NLoS) propagation with reflectors also can be used to enable

installation of fixed wireless links in various locations. Fixed reflectors or passive repeaters have been used in conventional microwave fixed wireless links to increase transmission range [3]. Reflectors can be also used in millimeter-wave or THz bands. However, the reflection loss would be larger than in microwave bands, because of roughness. Typical roughness of smooth wooden surfaces is about 100 micrometers.

In this paper, we will describe an overview of millimeter-wave and THz fixed transmission technologies where performance degradation due to weather conditions should be taken into account [5-8]. For long term evaluation, we are developing a 300GHz transmission system which can record data of wireless transmission and that of weather conditions. This paper also reviews recent research activities on THz-wave scattering from slightly rough surfaces to investigate reflection loss due to roughness [9, 10].

### XIV-2. 300GHz Fixed wireless transmission using V-band modems

Fig. XIV-1 shows a schematic of a networks connecting baseband units and remote antenna units through mobile backhaul and fronthaul links consisting of wired and wireless transmission. Optical fibers are commonly used for high-speed wired transmission. To avoid the wireless link becoming a bottleneck, the transmission capacity of the wireless link connecting to the optical fiber must be comparable to that of the optical fiber transmission. On the other hand, the required transmission range for the wireless link would be less than one kilometer, because separation between the remote antennas would be less than a few hundred meters. Many antennas are for small cells in future mobile networks. Fixed wireless systems using millimeter or THz bands can offer high-speed and short-distance radio links.

Over 100Gb/s wireless transmission has been recently demonstrated by using quadrature amplitude modulation with polarization multiplexing [11, 12]. However, most of research results are based on offline signal processing or unidirectional transmission demonstration. Duplex wireless systems are required to provide data links and functions over TCP/IP. MIMO also needs duplex links. Recently, 300 GHz duplex high-speed transmission was demonstrated by using millimeter-wave modems as baseband and IF modules [13]. V-band or E-band millimeter-wave signals are converted to 300GHz signals by using broadband mixers.

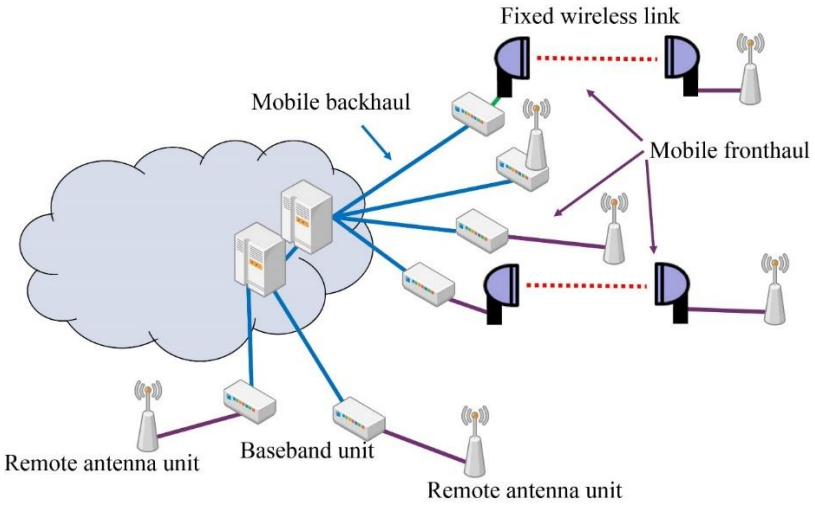


Fig. XIV-1. Mobile backhaul and fronthaul with fixed wireless links [2]

Fig. XIV-2 shows a configuration of the 300GHz transmission system using E-band FDD modems. E-band signals from four modems are combined together by a millimeter-wave circuit and upconverted into a 300GHz signal. A TDD system was also demonstrated by using V-band modems which comply with IEEE 802.15.3e. Two 802.15.3e signals can be aggregated and upconverted into a 300GHz TDD signal, as shown in Fig. XIV-3. Based on this research result, outdoor radio units with weather condition logger are being developed for long-term evaluation. 300GHz power amplifiers and mixers are connected to two V-band modems for parallel TDD duplex transmission. All the components are assembled in a water-proof box as shown in Fig. XIV-4. An antenna is shared with transmission and reception through a coupler with band-bass filter. IF signals in two 802.15.3e channels whose center frequencies are 60.48GHz and 62.64GHz are upconverted into 286.20GHz and 288.36GHz which are corresponding to channels 16 and 17 of IEEE 802.15.3d. 300GHz output power from an output port of the outdoor unit is about 0dBm and the antenna gain is 40dBi. As shown in Fig. XIV-5, a pair of outdoor radio units are installed in motor-controlled platforms for automatic alignment. The platform can control angle in 360 degrees in azimuth and from -45 degrees to +20 degrees in elevation with 0.01-degree resolution. The automatic alignment function would facilitate installation process and offer adaptable network configuration. We have confirmed that the outdoor units can offer stable wireless data transmission whose bitrate is 4Gb/s with QPSK. The THz signal complies with IEEE 802.15.3d.

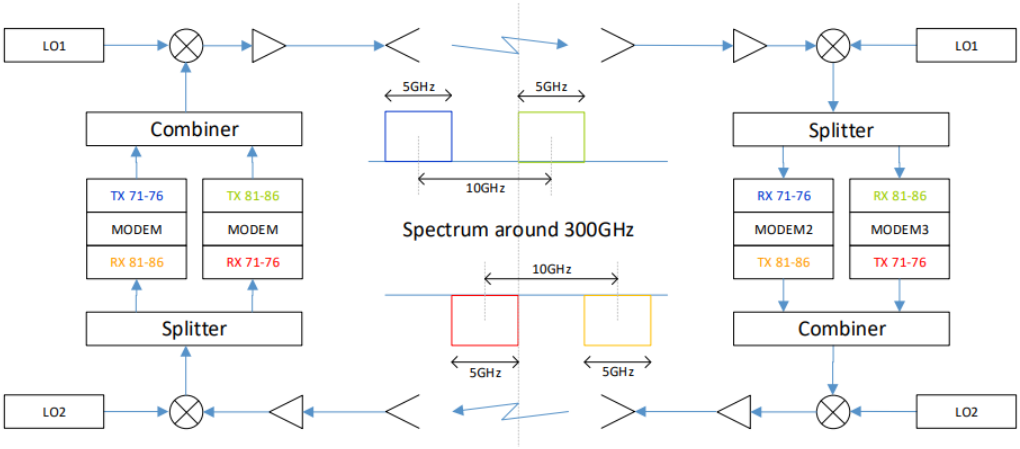


Fig. XIV-2. Configuration of 300GHz transmission system using E-band modems [14]

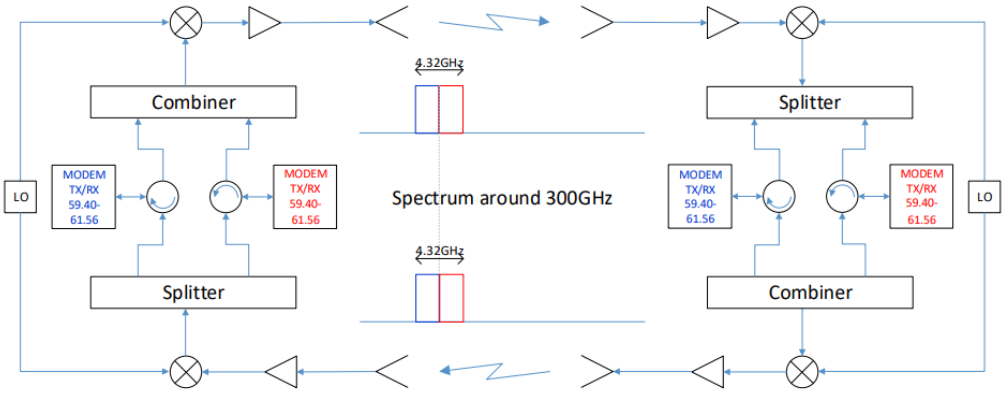


Fig. XIV-3. Configuration of 300GHz transmission system using V-band modems [14]

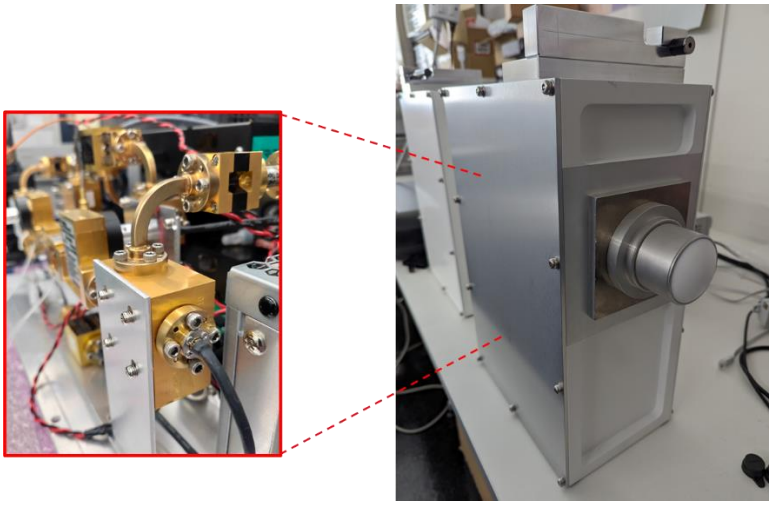

Fig. XIV-4. 300GHz outdoor radio unit

Fig. XIV-5. Outdoor radio unit mounted on a motor-controlled platform.

### XIV-3. THz-wave scattering

THz-wave scattering from slightly rough surfaces can be simulated by using the stochastic functional approach, where the scattered wave can be expressed as a functional of rough surfaces [9, 10]. The rough surface is expressed by two parameters: surface roughness, $\sigma$, and correlation length, $l$. To focus on the scalability of the scattering problem, normalized surface roughness, $k\sigma$, and correlation length, $kl$, are commonly used to describe the surfaces. Typical roughness of smooth wooden surfaces would be 40-100um, which corresponds to $k\sigma$ of 0.2-0.7. Fig. XIV-6 shows examples of calculated scattering wave distribution which is normalized by the incident wave power [15]. The left graph shows horizontal (TE) polarization. The right shows vertical (TM) polarization. The surface parameters for 300GHz, $k\sigma$, $kl$, and $n$ are respectively 0.3074, 0.419 and 1.3, which are actual values of a wooden sample. The roughness and correlation length are measured by a digital microscope.

The loss in reflection due to scattering can be calculated from integration of scattering distributions over a celestial sphere. The total scattering wave power is subtracted from the reflected and refracted wave power on a flat surface. Fig. XIV-7 shows the loss for various roughness. The loss is an increasing function of roughness $k\sigma$. When the roughness is larger than 0.5, the loss would not be negligible.

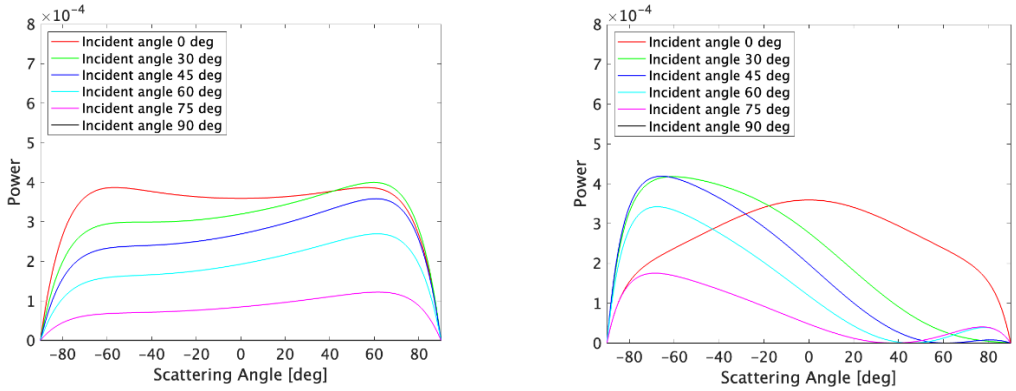


Fig. XIV-6. Scattering wave distribution calculated by stochastic functional approach, (left) horizontal polarization incidence, (right) vertical polarization incidence.

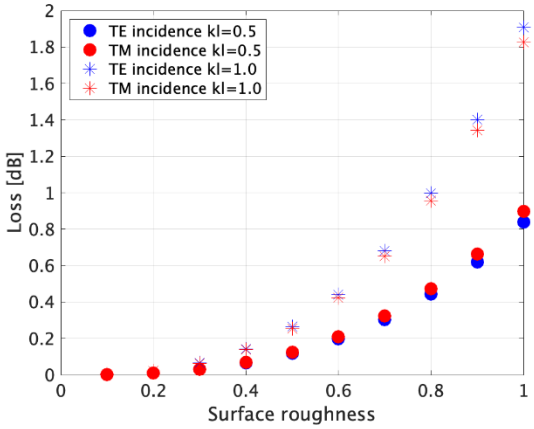


Fig. XIV-7. Reflection loss due to roughness.

## XIV-4. Conclusion

In this paper, we presented millimeter-wave and THz fixed transmission technologies which can be used in mobile backhaul and fronthaul in future mobile networks. We are developing 300GHz outdoor radio units which can record weather conditions and transmission performance for long term evaluation. NLoS propagation with reflectors also can be used to enable installation of fixed wireless links in various locations. However, the reflectivity would be degraded by scattering on rough surfaces. This paper reviewed recent research activities on THz-wave scattering from slightly rough surfaces to investigate reflection loss due to roughness.

## XIV-5. Acknowledgements

This presentation includes research results were supported by / obtained from ThoR (TeraHertz end-to-end wireless systems supporting ultra-high data Rate applications) funded in part by the Horizon 2020, the European Union's Framework Programme for Research and Innovation, under Agreement 814523, and in part by the Commissioned

Research (No. 196), JPJ012368C00302, JPJ012368C00401, JPJ012368C43103, JPJ012368C04901, JPJ012368C06001. THz transmission study was partly conducted under the contract “R&D of high-speed THz communication based on radio and optical direct conversion” by the Ministry of Internal Affairs and Communications of Japan under Grant JPJ000254.

## REFERENCE

[1] Mobile backhaul options, Spectrum analysis and recommendations, GSMA, 2018 https://www.gsma.com/spectrum/wp-content/uploads/2019/04/Mobile-Backhaul-Options.pdf

[2] T. Kawanishi, Wired and Wireless Seamless Access Systems for Public Infrastructure, Artech House 2020.

[3] APT Report on Technologies of Fixed Wireless System to Provide Remote Connectivity, APT/AWG/REP-85 (09/2018)

[4] E. Csanady, et al.: Quality of Machined Wood Surface (Springer, 183, 2015) (DOI: 10.1007/978-3-319-22419-0_4).

[5] Z. -K. Weng et al., Millimeter-Wave and Terahertz Fixed Wireless Link Budget Evaluation for Extreme Weather Conditions, IEEE Access, 9, 163476-163491 (2021)

[6] U. Mankong et al., Millimeter Wave Attenuation Due to Wind and Heavy Rain in a Tropical Region. Sensors, 23, 2532 (2023)

[7] APT Recommendation on Models for FWS Link Performance Degradation due to Wind, APT/AWG/REC-12 (12/2022)

[8] APT Report on FWS link performance under severe weather conditions, APT/AWG/REP-81 (04/2018)

[9] R. Yoshino et al., Modeling and evaluation of millimeter wave scattering from minimally rough surfaces on stones, IEICE Electronics Express, 19, 20220257 (2022)

[10] R. Yoshino et al., 300GHz Terahertz Wave Scattering Experiment and Simulation from Slightly Rough Surfaces on Dielectrics (*to be published in IEICE Communications Express*)

[11] W. Tong et al., Experimental Comparison of Single-Carrier and Digital Subcarrier Multiplexing Transmissions in a W-Band 200 Gb/s Fiber-Wireless System Considering Transmitter IQ Imbalance and Skew Mitigation, IEEE Photonics Journal, 15, 1-8 (2023)

[12] T. Kawanishi, THz and Photonic Seamless Communications," in Journal of Lightwave Technology, 37, 1671-1679 (2019)

[13] ThoR: TeraHertz end-to-end wireless systems supporting ultra high data Rate applications, https://thorproject.eu/

[14] ThoR Deliverables D2.2 Overall System Designhttps://thorproject.eu/wp-content/uploads/2019/07/ThoR_SIKLU_190417_F_WP2-D2.2-Overall-System-Design.pdf

[15] R. Yoshino et al., Scattering experiment and the effect of polarization from wooden surface for terahertz wave, IEICE Tech. Rep., vol. 123, no. 351, MWPTHz2023-86, pp. 60-63, Jan. 2024.

## Abbreviation List

| Abbreviation | Explanation |
|---|---|
| ABG | Alpha-Beta-Gamma |
| AI | Artificial Intelligence |
| ALD | Atomic Layer Deposited |
| AMC | Adaptive Modulation and Coding |
| AoA | Angle of Arrival |
| AR | Augmented Reality |
| ASIC | Application Specific Integrated Circuit |
| AWG | Arbitrary Waveform Generator |
| BAN | Body Area Network |
| BCB | Benzo cyclobutene |
| BER | Bit Error Rate |
| BF | Beam Forming |
| BS | Base Station |
| CC | Component Carrier |
| CI | Close-in |
| CMOS | Complementary Metal Oxide Semiconductor |
| CPS | Cyber Physical System |
| CSI | Channel State Information |
| DC | Direct Current |
| DFT | Discrete Fourier Transform |
| DL | Down Link |
| DNN | Deep Neural Network |
| DOA | Direction of Arrival |
| DSP | Digital Signal Processing |
| EVM | Error Vector Magnitude |
| eWLB | embedded Wafer Level Ball grid array |
| FDD | Frequency Division Duplex |
| FDE | Frequency Domain Equalize |
| FSPL | Free Space Path Loss |
| HARQ | Hybrid Automatic Repeat Request |

| Abbreviation | Explanation |
|---|---|
| **HPBW** | Half Power Beam Width |
| **IBO** | Input Back Off |
| **IFFT** | Inverse Fast Fourier Transform |
| **InH** | Indoor hotspot cell |
| **ISAC** | Integrated Sensing and Communication |
| **ITU-R** | International Telecommunication Union Radiocommunication Sector |
| **KPI** | Key Performance Indicator |
| **LAN** | Local Area Network |
| **LNA** | Low-Noise Amplifier |
| **LOS** | Light of Sight |
| **LTE** | Long Tern Evolution |
| **MCM** | Multichip Module |
| **MIMO** | Multiple-Input and Multiple-Output |
| **MMIC** | Monolithic Microwave IC |
| **MS** | Mobile Station |
| **MOS** | Metal Oxide Semiconductor |
| **MOS-HEMT** | Metal-Oxide-Semiconductor Eigh-Electron-Mobility Transistor |
| **MSL** | Microstrip Line |
| **NLOS** | Non-Line of Sight |
| **NR** | New Radio |
| **NRNT** | New Radio Network Topology |
| **OAM** | Orbital Angular Momentum |
| **OFDM** | Orthogonal Frequency Division Multiplexing |
| **PA** | Power Amplifier |
| **PCB** | Printed Circuit Board |
| **PLE** | Path Loss Exponent |
| **QMH** | Qualitative Microwave Holography |
| **RAN** | Radio Access Network |
| **RAT** | Radio Access Technology |
| **RD** | Relay Device |
| **RF** | Radio Frequency |

| Abbreviation | Explanation |
|---|---|
| **RIS** | Reconfigurable Intelligent Surface |
| **RMSE** | Root Mean Square Error |
| **RS** | Relay Station |
| **Rx** | Receiver |
| **SAG** | Selective-Area Growth |
| **SC** | Single Carrier |
| **SiP** | System-in-Package |
| **SISO** | Single-Input Single-Output |
| **SIW** | Substrate-Integrated Waveguide |
| **SNR** | Signal to Noise power Ratio |
| **Sub-THz** | Sub Tera Hertz |
| **TDD** | Time Division Duplex |
| **TDS** | Time Domain Spectroscopy |
| **THz** | Tera Hertz |
| **TMA** | Trimethylaluminum |
| **TSV** | Through-silicon Via |
| **Tx** | Transmitter |
| **UCA** | Uniform Circular Array |
| **UE** | User Equipment |
| **UL** | Up Link |
| **VR** | Virtual Reality |